

Simulation of Ladle Degassing in Steel Making Process

Thesis submitted for the degree of

Doctor of Philosophy

At the University of Leicester

by

Mansour N. Al-Harbi

Department of Engineering

University of Leicester

June 2007

UMI Number: U230186

All rights reserved

INFORMATION TO ALL USERS

The quality of this reproduction is dependent upon the quality of the copy submitted.

In the unlikely event that the author did not send a complete manuscript and there are missing pages, these will be noted. Also, if material had to be removed, a note will indicate the deletion.



UMI U230186

Published by ProQuest LLC 2013. Copyright in the Dissertation held by the Author.
Microform Edition © ProQuest LLC.

All rights reserved. This work is protected against
unauthorized copying under Title 17, United States Code.



ProQuest LLC
789 East Eisenhower Parkway
P.O. Box 1346
Ann Arbor, MI 48106-1346

Abstract

A multi-phase-species (steel/gas/slag and dissolved elements such as, Al, O, and S) mathematical model based on the fundamental transport equations has been developed. This model was used to study the refining of steel in a ladle, in particular desulphurisation. In this approach, a Computational Fluid Dynamics (CFD) analysis was used to predict the flow pattern of the gas-stirred ladle system. The thermodynamic analysis package MTDATA from the National Physical Laboratory (NPL) was linked to the CFD model to predict the mass transaction at the steel/slag interface during the refining process. A successful linkage between the Fluent (CFD) package and the MTDATA thermodynamics package has been achieved using a Visual Basic 6.0 environment. The predictions have been compared to data from the literature and a good agreement has been found.

In this present work, the capability of the model to predict the desulphurisation rate under various operational conditions has been demonstrated. The slag viscosity has been predicted using the NPL slag viscosity model and this has been successfully implemented. Therefore, it is possible to study the influence of the slag system composition variation during the refining process. Also, it will be possible to extend the present model to study other types of steelmaking processes involving slag-metal reactions.

In this present work, the influence on the desulphurization rate of allowing the Ca^{++} mobility and the CaS precipitation in the molten slag (slag system $\text{CaO-Al}_2\text{O}_3\text{-SiO}_2\text{-MgO}$) was examined.

Acknowledgements

My great thanks to my supervisors, Prof. H Atkinson and Dr. S Gao for the effective guidance, valuable advice, useful comments and continuous encouragement and support throughout the process of conducting this research.

I would like to express my sincere gratitude to my sponsor the Saudi Basic Industries Corporation (SABIC), for providing the scholarship and the assistance that enable me to carry on working this study.

I am thankful to Dr. P. Brown and A. Norman from the Engineering Department for their continuous support.

I acknowledge my gratitude to J. Gisby and J. Robinson from the National Physical Laboratory (NPL) for their generous assistance during this time.

I acknowledge my gratitude to Prof. S Seetharaman and Dr. Ling Zhang for their advice and discussion.

I also thank my colleague G. Shanley from SABIC technology centre for his assistance and excellent advice.

My great appreciation goes to my father and mother for their moral support and prayers for my success. For the most, I am specifically grateful to my wife for her patience for her support and tolerance.

All praise is due to Allah, most Gracious, most Merciful, for his help, blessing and guidance which gave me the patience and endurance to accomplish this work.

Content

List of symbols	i
1. Introduction	1
2. Literature survey	7
2.1 Fluid dynamic phenomena in the gas stirred ladle system	7
2.1.1 Plume characteristics and bubble behaviour in liquid	8
2.1.2 Bubble size prediction correlations	13
2.1.3 Mixing, heat and mass transfer phenomena in the gas stirred ladle	16
2.1.4 The role of convection in the molten steel circulation	22
2.2 The role of the slag in the steelmaking process	23
2.2.1 Thermodynamic fundamentals	24
i) Slag basicity	25
ii) Slag sulphur capacity	26
2.2.2 Slag thermo-physical properties	28
2.2.3 Models of ionic melt properties	31
i) Slag sulphur capacity	31
ii) Slag viscosity	34
a) KTH slag viscosity model	35
b) NPL slag viscosity model	39
c) Zhang and Jahanshahi slag viscosity model	39
iii) Note on the use of the NPL model in the present work	41
2.2.4 Cation diffusivity in molten slag	41
2.3 Gas refining in a ladle degassing system	42
2.4 Gas stirred system simulation	43
3. Simulation of the ladle gas stirred system	47
3.1 Mathematical formulation	47
3.1.1 Assumptions	47
3.1.2 Transport equations	49
3.2 Boundary conditions	53
3.2.1 Gas inlet nozzle	53
3.2.2 Ladle side and bottom walls	54
3.2.3 Pressure outlet	55

3.3 Interactions between two fluids	55
3.3.1 Drag coefficient models	55
3.3.2 Identification of the most appropriate drag coefficient and bubble size models	59
3.4 Steel/slag physical and thermal properties	60
3.5 Basis for the use of the thermodynamic prediction package	62
3.6 Solution method strategy	63
3.7 Mathematical model development stages	67
3.7.1 Grid development	67
3.7.2 Gas escape mechanism	69
3.7.3 Thermal interaction between phases and gas bubble size influence	71
3.8 Model validation	74
3.8.1 Thermal validation of the present mathematical formulation	74
3.8.2 Fluid dynamic validation of the present mathematical formulation	75
4. Results	76
4.1 Gas stirred system, CFD results	78
4.1.1 Model validation	78
i) Thermal validation	78
ii) Fluid flow validation	80
4.1.2 Fluid flow inside gas stirred ladle vessel	81
4.1.3 Bubble size and energy dissipation rate	86
4.1.4 Temperature distribution	87
4.2 CFD and thermodynamic coupling results	91
4.2.1 Model validation	92
4.2.2 Slag viscosity model and gas flow rate	94
4.2.3 The influence of allowing Ca^{++} mobility and CaS precipitation	94
4.2.4 Real plant data	95
5. Discussion	96
5.1 Gas stirred system, CFD results discussion	96
5.1.1 Fluid flow inside the gas stirred ladle vessel	97
5.1.2 Bubbles size	102
5.1.3 Gas stirred ladle thermal analysis	102
i) Heat losses	102
ii) Choice of the turbulent Prandtl number	103

5.2 CFD and thermodynamic coupling results	106
5.2.1 The effect of the change in the rate of interfacing between Fluent and MTDATA	106
5.2.2 The influence of the use of the NPL slag viscosity model	112
5.2.3 The influence of allowing CaS precipitation	114
5.2.4 The influence of nozzle configuration on the desulphurisation rate	115
6. Conclusion	117
7. Future works	119
8. References	120
Appendix A	132
Appendix B	141

List of symbols

A^W	pre-exponential term
a, b	fitting coefficients
B_{LF}	ladle furnace slag basicity
C_d	drag coefficient
C_D	drag coefficient
$C_{p,i}$	i th component heat capacity
D_i	diffusivity coefficient of species i
$D_{i,n}$	nozzle inner diameter;
D	ladle vessel diameter
$d_{b,max}$	maximum stable bubble size.
$d_{b,mean}$	mean bubble diameter in (cm)
d_b	bubble size
d_c	critical bubble size
d_o	nozzle diameter
E_o	Eotvos number
E_η^W	activation energy parameter
ΔG°	standard Gibbs energy change of reaction
ΔG^*	change in Gibbs energy of activation per mole
ΔG_i^*	change in Gibbs energy of activation of component i
ΔG_{mix}^*	change in Gibbs energy of activation of a mixture
H	bath height
h	Planck's constant
I	turbulent intensity
k	thermal conductivity
L	ladle vessel height
M	molecular weight
M_i	molecular weight of component i
Mo	Morton number
n_i	number of oxygen atoms in component i
N	Avogadro's number

Nu	Nusselt number
N_o	oxygen fraction
Pr	Prandtl number
Pr_t	turbulent Prandtl number
Pr_{t_w}	turbulent Prandtl number value far from the wall
Pe_t	turbulent Peclet number
Q_g	gas flow rate ($\text{cm}^3 \text{sec}^{-1}$)
q_g	gas flow rate
R	gas constant
Re	Reynolds number
T	temperature
U_g	gas flow rate per unit area
u_b	bubble rising velocity
We	Weber number
We_c	critical Weber number
X_i, x_i	mole fraction of component i
V	molar volume
y_i	cation fraction of cation i
Z	vertical position

Greek symbols

ρ_i	i_{th} material density
$\rho_{g,n}$	gas density at normal temperature
$\rho_{g,b}$	gas density at bath temperature
σ	surface tension
ε	dissipation rate of turbulent kinetic energy
ε_M	eddy diffusivity of momentum
ν	kinematic viscosity
τ_m	melt mixing time
Λ_i	i_{th} oxide optical basicity

$\Lambda_{th,i}$	i_{th} oxide theoretical optical basicity
Λ^{corr}	corrected optical basicity
γ_i	i_{th} element activity coefficient
ξ	Slag sulphur capacity model parameter (equ. 23)
ξ_i	i_{th} component parameter (table 3)
ξ_{mix}	Component interaction parameter (table 3)
δ and Δ	parameters describing the variation between the calculated and the measure values of the slag viscosity
η	slag viscosity
η_{cal}	calculated slag viscosity
η_{mea}	measured slag viscosity
μ	dynamic viscosity

1. Introduction

Steel is the most extensively used metallic material, mainly due to its relatively cheap cost and its mechanical properties. The steelmaking process can be divided into two main parts namely, *primary* and *secondary* steelmaking. In the primary phase, there are two main different routes, electric arc furnace (EAF) and blast furnace as illustrated in figure 1. In the steelmaking process using EAF, first the iron ore is reduced and the oxygen is removed to produce a metallic iron called Direct Reduction Iron (DRI). Then, different fractions of scrap and/or reduced iron ore are melted in the EAF furnace to produce molten steel. However, in the steelmaking process using the blast furnace the route is different. The iron ore is reduced in the blast furnace to produce molten pig iron. Then this molten iron and a scrap material are mixed in the Basic Oxygen Furnace to produce molten steel. In secondary steelmaking, the molten steel coming from the primary phase is transferred into the ladle furnace for chemical adjustment and refining prior to continuous casting, as illustrated in figure 1.

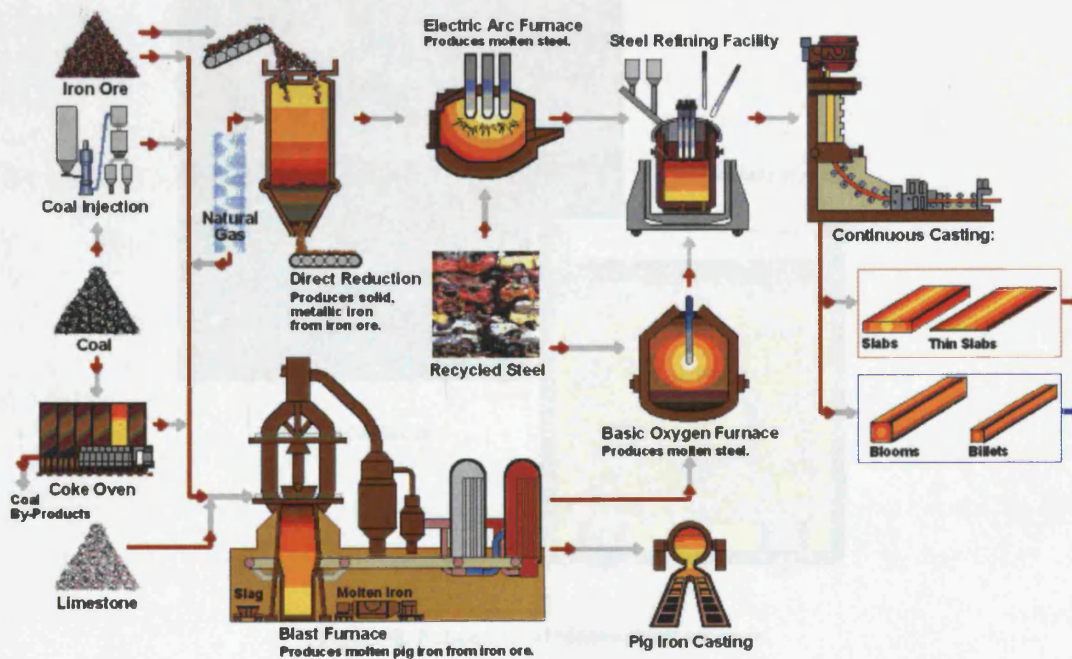


Figure-1. Schematic of steelmaking process.

The first bottom blown steelmaking process was invented by Sir Henry Bessemer over hundred and fifty years ago [1]. Over the years, steelmaking technology has improved. Higher quality steel products are produced within less production time to cover the huge market demand for high quality clean steel. The secondary steelmaking process becomes a key stage for clean steel production and the continuous casting process.

In the secondary steelmaking gas stirred ladle system an inert gas is injected from the ladle vessel bottom through a porous plug/nozzle to circulate the molten steel inside the vessel to achieve a proper chemical and thermal homogenisation, and enhance the reaction rates. During the molten steel circulation with gas bubbles, the unwanted elements, dissolved gases, and inclusions are absorbed by the top slag layer and removed from the melt as illustrated figure 2. This refining process is enhanced under vacuum operation conditions. Therefore, the ladle-degassing system shown in figure 3 is usually applied for high quality clean steel production but this increases the final product cost as a result of the high technology used. Lime, bauxite, and dolomite are usually added during molten steel tapping into the ladle vessel to form a suitable slag for desulphurization. During the refining process, chemical reactions occur at the steel/slag interface zone resulting in sulphur removal from the molten steel.

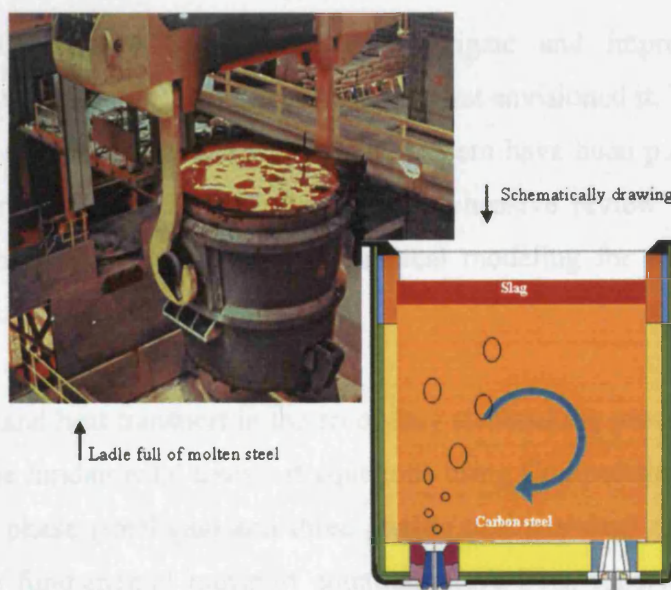


Figure-2. Schematic of steelmaking process.

Sulphur is considered to be a harmful impurity, because it causes hot shortness in steels. In the modern continuous casting route, sulphur should be 0.02 wt%. However, for special steel grades, the sulphur limit becomes as low as 0.005 wt%.

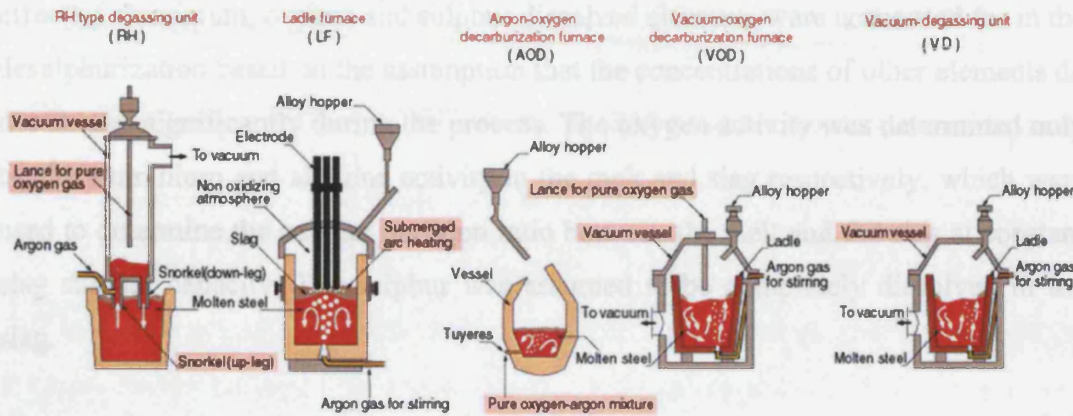


Figure-3. Schematic of typical facilities for secondary steelmaking refining process.

In certain application, e.g. shell plates, plates for off-shore oil industry and line pipes, the sulphur content should be less than 0.002 wt%, and there is more demand for Ultra Low Sulphur (ULS). An extensive steel desulphurisation can be achieved in the vacuum degassing unit (VD) in addition to hydrogen and some nitrogen removal. The vacuum degassing unit (VD) is shown schematically in figure 3.

Extensive efforts have been made to investigate and improve the secondary steelmaking process since Sir Henry Bessemer first envisioned it. Many mathematical and physical models of the gas stirred ladle system have been published in the past. Mazumdar and Guthrie [1] published a comprehensive review in the mid-nineties illustrating the great potential of mathematical modeling for metallurgical process enhancement.

Today, mass and heat transport in the secondary steelmaking process can be predicted by solving the fundamental transport equations using Computational Fluid Dynamics (CFD). Two phase (steel/gas) and three phase (steel/gas/slag) mathematical models based on the fundamental transport equations have been reported in the literature. Jonsson et al. [2] established a new approach to steel refining simulation. The Jonsson et al. [2] three phase axi-symmetric model was the only multiphase model accounting

for the slag phase found in the open literature to investigate the gas stirred ladle system. Therefore, it was taken as an example to follow. In the Jonsson et al. work, the three phase (steel/slag/gas) model was linked with a thermodynamic model to simulate the desulphurization process. Some simplifications were made. Only the effect of aluminium, oxygen and sulphur dissolved elements were accounted for in the desulphurization based on the assumption that the concentrations of other elements do not change significantly during the process. The oxygen activity was determined only by the aluminium and alumina activity in the melt and slag respectively, which were used to determine the sulphur partition ratio between the melt and the slag at constant slag sulphur capacity. The sulphur was assumed to be completely dissolved in the slag.

In this present work, a multi-phase-species (steel/gas/slag and dissolved elements such as Al, O, and S) mathematical model was developed using the Fluent commercial CFD package. In our analysis, this CFD package is iteratively linked with a thermodynamic prediction package called MTDATA and supplied by the National Physical Laboratory (NPL). MTDATA was used to predict the species exchange at the metal/slag interface. Figure 4 illustrates the core difference between the present model in comparison with the work of Jonsson et al. In the Jonsson work, the thermodynamic data is obtained initially and inserted into the CFD simulation. In contrast, in our approach, the iterative linkage allows updating of the thermodynamic parameters during the simulation. The MTDATA package gives enhanced thermodynamic prediction in comparison with Jonsson et al. , due to its capability for multi-component systems containing up to 30 elements. MTDATA is equipped with four different databases named NPLOX3, NPLOX_trace, TCFE, and SUB_SGTE from NPL.

Desulphurization is taken as an example in this analysis. The two commercial packages were linked together using the Visual Basic 6.0 environment. Also a simple data exchange code using a text file mechanism was created. As a result, in future this simulation model can be adapted to study other types of steelmaking processes involving slag-metal reactions. Comparison of the results calculated with data from the literature show the potential of this model.

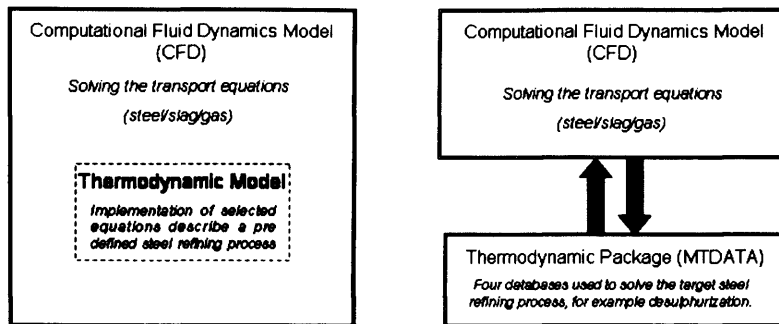


Figure-4. Sketch to illustrate Jonsson et al. approach (left), and the present approach (right).

The aim of this project was to link the Fluent CFD package and the MTDATA thermodynamic package in order to simulate ladle refining. Ladle refining is a very dynamic process. Therefore, in this present work, the different physical phenomena occurring in the multi-phase gas stirred ladle system, e.g. the two-phase region plume development, were investigated prior to building the mathematical model. In addition, attention was given to study the role of slag thermo-physical properties in the refining process. Due to the complex nature of slag structure, usually some of its properties, e.g. viscosity, are very sensitive to temperature and composition variation during the refining process. Therefore, different mathematical models of the slag melt properties were investigated to implement in this present mathematical model.

In this present work, the desulphurization process was taken as an example. The developed three phase (steel/gas/slag) mathematical model was used to study this refining process in secondary steelmaking. During the refining process the slag chemistry and temperature vary and this can have a dramatic influence on the slag physical properties as discussed later. In addition to the temperature influence, the Ca^{++} cation behavior in the multicomponent slag system $\text{CaO-Al}_2\text{O}_3\text{-SiO}_2\text{-MgO}$ was monitored at the steel/slag interface during the desulphurization process. A particularly novel aspect is that the precipitation of the CaS is allowed to occur in the molten slag once the solubility limit is exceeded. An advanced slag viscosity model was used to monitor the local slag viscosity changes due to the variation in CaO concentration.

The literature review and the established background related to gas stirred ladle refining is described in chapter 2. The three phase (steel/slag/gas) model development and the coupling approach for linking the CFD model with the thermodynamic package is given in chapter 3. In addition, analysis and comparison between the different available correlations/models describing particular issues for the system behavior, such as bubble size, drag coefficient, and slag viscosity are given in chapter 3. Results and discussion are given in chapters 4 and 5 respectively. Finally the conclusions and future work are given in chapters 6 and 7 respectively.

The following papers have been published on this work.

- M. Al-Harbi, H. Atkinson, and S. Gao, "*Modeling methodology to simulate of molten steel refining in a gas-stirred ladle using a coupled CFD and thermodynamic model*" Modeling of Casting, Welding and Advanced Solidification Processes-XI, Opio, France, May 2006, pp. 1089-1096.
- M. Al-Harbi, H. Atkinson, and S. Gao, "*Gas stirred ladle: Multi-phase-species mathematical model*" presented at The Association for Iron & Steel Technology (AIST), Indiana Convection Centre, Indianapolis, Ind. USA, May 7-10, 2007, (CD ROM AIST Proceedings)
- M. Al-Harbi, H. Atkinson, and S. Gao, "Simulation of secondary steelmaking refining process; gas-stirred ladle multi-phase-species mathematical model", presented at Saudi Innovation Conference 2007, Newcastle, UK, May 12, 2007. in press.
- M. Al-Harbi, H. Atkinson, and S. Gao, "*Sulphide solubility limit in multicomponents slag system and its influence on the desulphurization rate in steelmaking*" presented at Seventh International Conference on Clean Steel, Balatonfüred, Hungary, June 4-6, 2007, in press.

2. Literature survey

In steelmaking, and especially in secondary steelmaking many physical and chemical phenomena are important including fluid flow, thermodynamics, material property variations, and issues with the slag system that could influence the final product quality. In this chapter, these phenomena will be discussed.

Fundamental background about the fluid dynamic phenomena associated with the secondary steelmaking process is described below in section 2.1. The roles of slag in the steelmaking process, slag thermo-physical properties, and other issues with slag are described in section 2.2. The gas refining mechanism in the ladle degassing system and the multiphase gas stirred system simulation are described in sections 2.3 and 2.4 respectively.

2.1 Fluid dynamic phenomena in the gas stirred ladle system

Numerous physical phenomena occur associated with the multi-phase (steel/slag/gas) gas stirred ladle system. Several physical issues can be seen from the sketch in figure 5, namely gas/liquid interaction, two-phase region (gas/liquid) plume development, mass transfer between the steel and top layer slag, gas bubble behaviour, and so on. The plume characteristics and bubble behaviour are described in section 2.1.1, bubble size prediction is discussed in section 2.1.2, and mass transfer and mixing phenomena are described in section 2.1.3. Finally, the influence of convection on molten steel circulation is discussed in section 2.1.4.

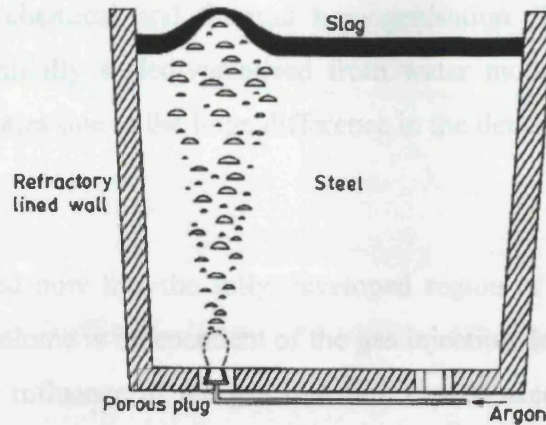


Figure-5. Schematic of gas stirred ladle.

2.1.1 Plume characteristics and bubble behaviour in liquid

The two-phase gas stirred molten steel within the ladle vessel can be divided into four different regions namely, primary bubble, free bubble, plume region and spout region as illustrated in figure 6. The plume region is the main section and is distinguished by a separate cap bubble in an air-water model [1].

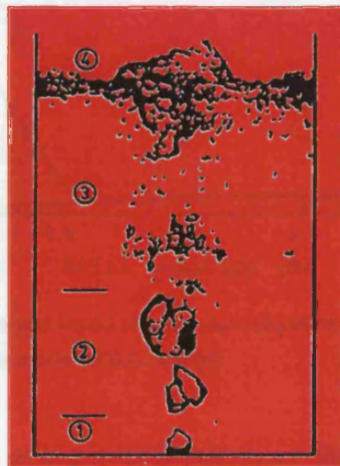


Figure-6. Characteristics of the two-phase air-water plumes in cylindrical vessel [1]

A two-phase plume region is formed due to the gas injection into the liquid phase within a cylindrical vessel using a nozzle located at the bottom as sketched in figure 5. This two-phase region consists of gas bubbles and liquid. The rise of the gas bubbles results in sufficient liquid circulation. In the secondary steelmaking refining process, inert gas injection is used as a driving mechanism for molten steel circulation to

achieve the target chemical and thermal homogenisation. The gas plume within molten steel was initially scaled/visualised from water model measurements, with significant uncertainties due to the huge difference in the density ratios and interfacial tensions [3].

It is widely accepted now that the fully developed region of the two-phase system within the control volume is independent of the gas injection device and pressure inlet conditions [1]. The influence of the gas injection device used (nozzle/porous plug) and the gas input kinetic energy is limited to the local area near the inlet [1, 4]. The injected gas velocity is drastically reduced within a short distance from the inlet due to the gas kinetic energy losses [4], as illustrated in figure 7.

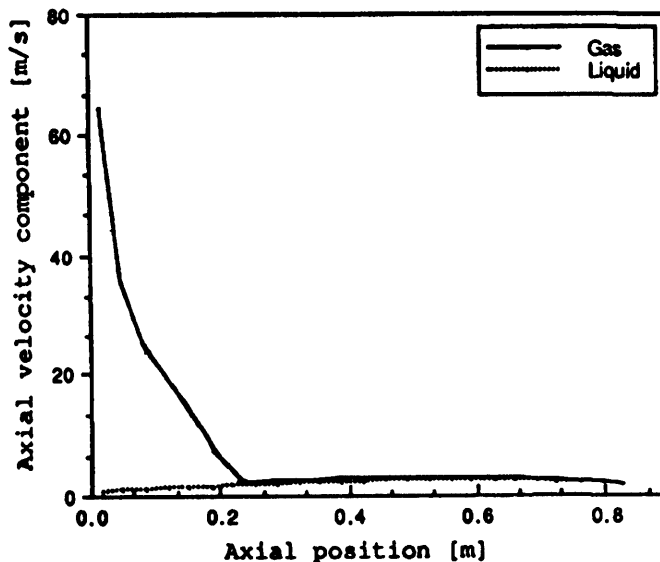


Figure-7. Gas and liquid phase axial velocities along the centre line [air/water model at 0.6 sec] [4].

Generally, any large bubbles at the inlet break down into an array of smaller bubbles shortly above. Bubble equilibrium size in the plume region is determined by the thermo physical properties of the system and not by the gas inlet pressure and velocity conditions. Furthermore, Komarov and Sano [5] found similar results, where the gas bubble size depends on gas flow rate, physical properties of the gas/liquid and temperature of the injected gas. Their experimental results using different kinds of gasses and injected into different liquids with variation in gas temperature are illustrated in figures 8 and 9. Helium produces larger bubble sizes than nitrogen for

similar experimental conditions due to the difference in gas properties, as shown in figure 9.

The surface tension influences the bubble diameters. The rising bubble average diameter at constant gas flow rate decreases with decrease in surface tension as illustrated in figure 8 [5]. Excluding the free surface and the primary region near the gas inlet the measured average bubble rise velocity at the axis of the plume is reasonably independent of the axial height at any given gas flow rate [1], as shown in figures 10 and 11.

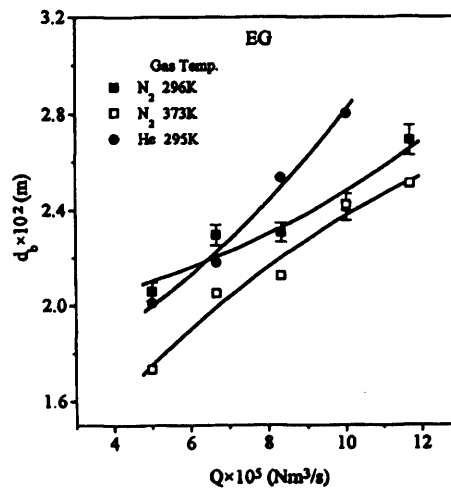
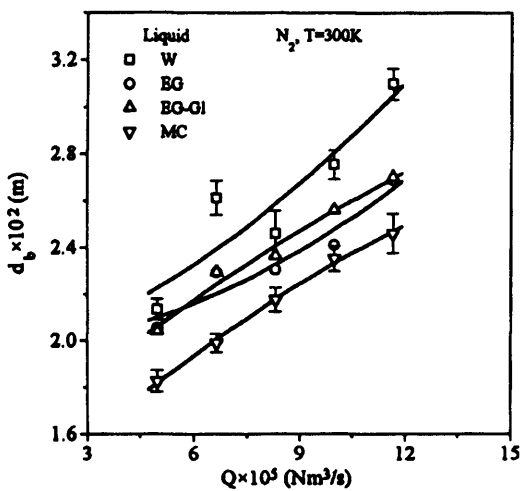


Figure-8. Gas bubble size as a function of flow rate in various liquid baths. [5]. The liquids W, EG, EG-GI, and MC are water, ethylene glycol, ethylene glycol glycerin and methyl carbitol respectively. The surface tension (kg/s²) for W, EG, EG-GI, and MC (at 293-373 K) are 0.07, 0.047, 0.05, and 0.036 respectively.

Figure-9. Gas bubble size as a function of flow rate for N₂ at 296 k and 373 K and He at 295 K [5] in Ethylene glycol

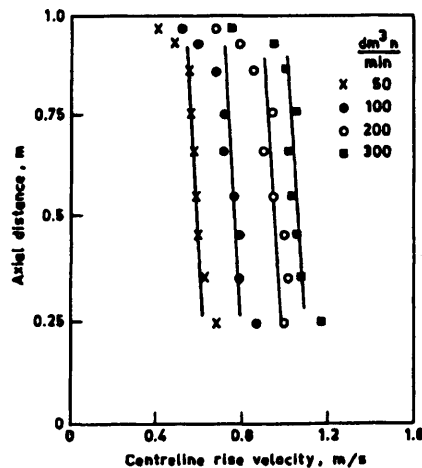
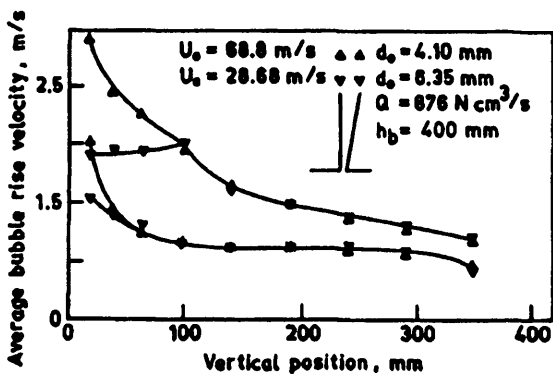


Figure-10. Bubble rise velocity as a function of axial height at the plume centreline [1]. The figure key was not defined in reference (1). However, U_o is expected to be the inlet gas injection velocity, d_o is the inlet nozzle diameter, and h_b is the vessel height.

Figure-11. Gas flow rate ($\text{dm}^3/\text{min} = 10^{-1} \text{ m}^3/\text{min}$) influence on liquid rise velocity at the plume centreline [1].

In a two phase system, bubble break up can be due to the following reasons [6]:

- Break up due to density variation; the maximum stable bubble size as a function of density variation can be expressed as:

$$d_{b,\max} \approx 4 \cdot \sqrt{\sigma/g \cdot \Delta\rho} \quad (1)$$

- Break up due to velocity gradients; a bubble in a shear field tends to rotate and deform. If the velocity gradients are large enough, interfacial tension forces are no longer able to keep the fluid bubble in one piece, and it breaks up into two or more smaller bubbles.
- Break up due to a turbulent fluid flow field.

Generally, it is reasonable to assume a spherical bubble shape with low Morton number ($M < 10^{-8}$) system [6].

The plume diameter near the top surface is expected to be larger in molten steel than water due to the higher density difference resulting in greater bubble expansion as the bubbles get closer to the top surface [7]. Xie et al. [8] studied the bubble behaviour using a low melting temperature alloy called Wood's metal of density (9.4 g/cm^3) as a liquid to model operation. The measured radial distribution of injected gas phase fraction using a centric nozzle at the bottom of the vessel is shown in figure 12. The plume is narrow at the base but gets wider towards the top. Figure 13 shows the gas fraction profile using an eccentric nozzle. The plume is different from the centric case, and it shifts towards the wall due to the difference in flow field velocity of the surrounding liquid that results in a pressure difference around the plume. This plume shift due to the use of an eccentric injection nozzle must be accounted for in the selection of the porous plug eccentric position at the bottom of the ladle to avoid extensive erosion of the refractory lining.

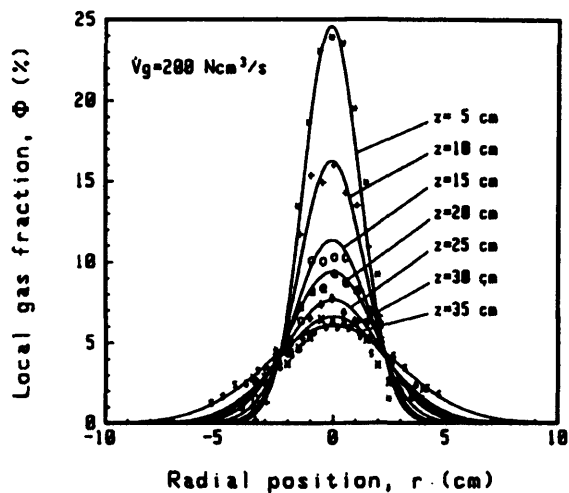


Figure-12. Gas fraction profile at various levels [8]. Z is the distance from the vessel bottom, and V_g is the gas volume flow rate.

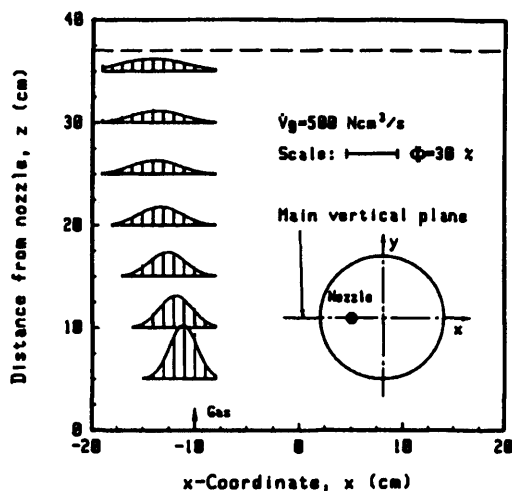


Figure-13. Gas fraction profile of eccentric injection case [8]. V_g is the gas volume flow rate, and Φ is the local gas fraction.

The presence of the top buoyant slag phase in the system results in a significant reduction of the system kinetic energy of motion at any given gas flow rate. The system energy is dissipating due to the deformation and entrainment of the slag phase within the bulk liquid phase. This results in slowing down the bulk motion of the liquid. Such a phenomenon is illustrated in figure 14 for dissimilar upper phase conditions [1]. Also, Mazumdar et al. [9] Iguchi et al. [10] and Ilegbusi et al. [11] reported a similar conclusion of the significant influence of the presence of the top slag layer on the molten metal motion at the recirculation region of the stirred metal. Furthermore, Iguchi et al. [10] define a critical viscosity value of the oil top layer in a water/oil model, where an oil with viscosity above this value would play a major role in the general overall water recirculation.

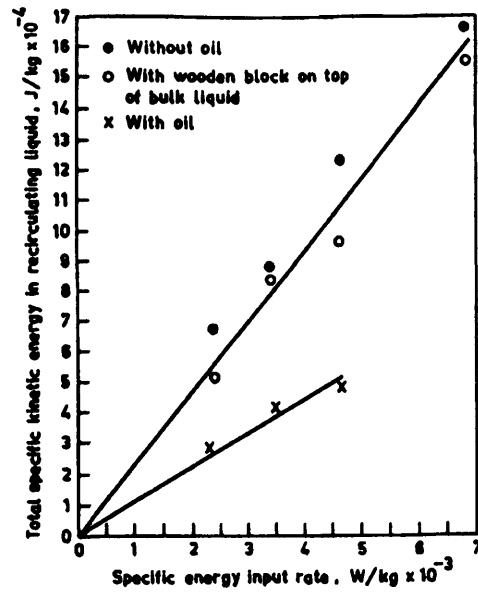


Figure-14. Total specific kinetic energy in recirculation vs. energy input rate for various slag conditions[1].

2.1.2 Bubble size prediction correlations

Turkoglu and Farouk [4] assumed an average bubble size of 10 mm over the entire domain of the gas injected iron bath numerical model. Xie et al. [8] suggest the correlation below to determine the mean spherical bubble diameter at a height of 10 (cm) above the nozzle position:

$$d_{b,mean} = 1.46 \cdot \left[\frac{Q_g}{z + H} \right]^{0.1} \quad (2)$$

where, $d_{b,mean}$ is the bubble diameter in (cm), Q is the injected gas flow rate in (cm^3/sec), and z and H are the vertical position and the metal path height respectively in (cm). However, the authors reported an insignificant gas bubble size change with respect to the vertical height as illustrated in figure 15. On the other hand, Mori et al. [12] present an empirical correlation to determine the bubble size immediately above the porous plugs on molten iron path:

$$d_b = \left\{ \left(\frac{6\sigma_l D_{i,n}}{\rho_l g} \right) + 0.0242 (q_g^2 D_{i,n})^{0.867} \right\}^{1/6} \quad (3)$$

where σ_l and ρ_l are the surface tension and the density of the liquid respectively, q_g is the gas flow rate, and $D_{i,n}$ is the inner diameter of the nozzle.

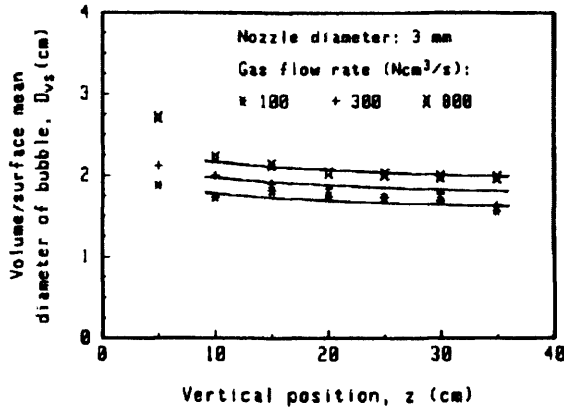


Figure-15. Volume/surface mean bubble diameter for various gas flow rate and heights [8].

Wang et al. [13] reported about the concept of the maximum stable gas bubble size in a turbulent flow. The bubble size is dependent on the flow turbulence intensity as per the following empirical formula.

$$d_{b,max} = \left(\frac{We_c \cdot \sigma_l}{\rho_l} \right)^{0.6} \cdot \frac{1}{\varepsilon^{0.4}} \quad (4)$$

where σ_l and ρ_l are the surface tension and the density of the liquid respectively, and We_c is the critical Weber number that was suggested to have the values 1.2 to 1.3, and ε is the dissipation rate of turbulent kinetic energy. In the turbulent region, the large bubbles would split into smaller bubbles due to the high velocity fluctuation that creates a large shear force on the bubble surface. Therefore, the bubble size decreases with increase of the flow turbulence intensity. The maximum stable bubble size for a given turbulent intensity can be estimated using equation (4); the bubbles larger than $d_{b,max}$ would collapse into smaller bubbles less than $d_{b,max}$. However, the smaller bubbles created would combine into a large bubble due to the relatively weak turbulent intensity in the ladle stirred system. Also, Oeters [14] proposed a relationship to determine the gas bubble size as a function of the drag coefficient in the complete flow domain except the region immediately above the porous plug position.

$$d_b = \left\{ 2 \left(\frac{6}{C_D} \right)^{1/3} \cdot \frac{\sigma_l}{0.52 \cdot g \cdot (\rho_g \cdot \rho_l)^{1/3}} \right\}^{1/2} \quad (5)$$

where C_D is the drag coefficient.

Relatively large gas bubbles in motion are subject to deformation resulting in breakup into small bubbles. The drag force applied by the liquid on moving bubbles encourages rotational and most likely a turbulent motion of the gas inside the bubble. This motion forms a dynamic pressure on the bubble surface; causing bubble breakup when this force exceeds the bubble surface tension. The associated energy with the drag force is much greater than the kinetic energy of the gas bubbles, due to the large ratio difference between the gas and liquid densities. Therefore, the gas velocity inside the bubble will be similar to the bubble velocity. On the basis of this theoretical analysis, the following equation was proposed for the critical bubble size as a function of bubble velocity [15]:

$$d_{b,c} = \left(\frac{3}{C_d \rho_g \rho_l^2} \right)^{1/3} \cdot \frac{2\sigma}{u_b^2} \quad (6)$$

where C_d , σ , and u_b are the drag coefficient, the surface tension and bubble rising velocity respectively.

Ilegbusi and Szekely [3] implement the bubble size expression in equation (7) with the assumption it is applicable to the gas stirred system:

$$d_b = 0.091 \left(\frac{\sigma}{\rho_l} \right)^{0.5} \cdot U_g^{0.44} \quad (7)$$

$$U_g = \frac{4Q}{\pi d_o^2} \quad (8)$$

where σ and ρ_l are the interfacial tension between the two phases (liquid and gas) and the liquid density respectively. Also, Q and d_o are the gas flow rate and the nozzle diameter respectively.

2.1.3 Mixing, heat and mass transfer phenomena in the gas stirred ladle

In an earlier study it was suggested that the mixing phenomena in metallurgical reactors occur mainly due to eddy diffusion and not by the bulk liquid phase recirculation. However, Mazumdar and Guthrie [1] illustrate that mixing phenomena are a function of both bulk circulation and eddy diffusion in the ladle gas stirred system.

Various investigations of mixing time have been reported over the years. The mixing time can be defined as the gas stirring time required to achieve 95% homogenisation [16]. Proposals for the correlation of mixing time with operating conditions and vessel geometry are shown in table 1 [1]. The discrepancies could be accounted for by the differences in gas flow rate and vessel aspect ratio (L/D), which do not match with the industrial expected conditions in the operation of the ladle refining. The industrial ladle in gas stirred systems tends to have an aspect ratio lying in the range of (0.5-2.0), and the molten steel is stirred with gas flow rate in the range of 0.0015 to 0.01 $\text{Nm}^3/(\text{min}\cdot\text{tonne})$ (N indicates 'normal' conditions i.e. 1 atm pressure and room temperature, "tonne" is a unit of mass equal to 1000 kg) [1].

In the system energy balance it is reasonable to consider the input kinetic energy of the injected gas. However, this energy contribution in the overall energy balance of the system is insignificant and typically less than 5% or so. On the other hand, the potential energy provided by the gas bubbles rising up due to the density difference can be considered as the main energy source of the system [1]. Expressions for the total specific energy input rate are given in table 2 [1].

Figure 16 illustrates the relation between the experimentally measured mixing time and the energy input rate for three different groups of researchers. In all of these results, two distinct ranges are present that suggest there is a transition from laminar to turbulent flow.

Table-1. A summary of mixing time correlation and applied experimental configuration reported by various researchers [1]. The reference numbers inside the table refers to the original source reference list, and are not listed in this report.

Investigators	Exp. tech.	Mixing criteria	Vessel dimensions and mass of fluid	Specific gas flow rates (m ³ /min/T)	Mixing time correlation
Nakanishi <i>et al.</i> ⁴⁷⁾	pH	Undefined	L=0.465 m, D=0.42 m; 64 kg	0.015 to 0.06	$\tau_m = 800 a_m^{-0.4}$
Asai <i>et al.</i> ⁴⁸⁾	Electrical conductivity	99%	D=0.405, 0.2 & 0.10; L/D=0.5 to 1; 52 kg (max) & 0.4 kg (min)	Numerous; say, 0.019 to 0.90 with ref. to D=0.405 m & L=0.40 m	$\tau_m = 274 a_m^{-0.33} L^{-1} R^{1.36}$
Sinha & McNellan ⁴⁹⁾	pH	97.7%	L=0.48 m, D=0.45 m; 76 kg	0.02 to 0.4	$\tau_m = 692 a_m^{-0.89}$
Themelis and Stapurewicz ⁵³⁾	Photocell	95%	L=0.67 to 1.0 m, D=0.66 m; 310 kg (max)	0.13 to 0.96	$\tau_m = 164 a_m^{-0.39} L^{0.39}$
Mietz and Oeters ⁵²⁾	Electrical conductivity & colorometry	95%	L=1.0 m, D=0.63 m; 311 kg	0.038 to 0.29	$\tau_m = C_1 Q_g^{-n} C_2$ and n are functions of tracer addition and monitoring locations
Mazumdar and Guthrie ⁵⁶⁾	Electrical conductivity	95%	L=0.5 to 1.1 m, D=1.12 m; 1000 kg	0.012 to 0.06	$\tau_m = 37 a_m^{-0.33} L^{-1} R^{1.66}$
Krishnamurthy <i>et al.</i> ⁵⁵⁾	Electrical conductivity	99.9%	L=0.1 to 0.45 m, D=0.48 m; 81 kg (max)	0.11 to 2.67	$\tau_m = C_1 Q_g^{-n} C_2$ and n are functions of flow regime and liquid depth

However, an outstanding correlation of the mixing time that gives a prediction of the mixing time with accuracy of 95% for a variety of gas stirring system in water models as well as actual industrial system is as follows [1]:

$$\tau_m = 71.84 \left(Q_g \frac{\rho_{g,n}}{\rho_{g,B}} \right)^{-0.38} D^{2.0} L^{-0.66} \quad (9)$$

where Q_g is the gas flow rate, $\left(\frac{\rho_{g,n}}{\rho_{g,B}} \right)$ is the gas density ratio at the normal and bath temperature, D is the ladle vessel diameter, and L is the height of the vessel.

Table-2. "Various expressions for rate of potential energy input to the gas stirred system and the corresponding estimates in an aqueous system for typical experimental situations. ($L=1.0\text{m}$, $D=1.0\text{m}$, $Q=1.10^{-4}\text{Nm}^3/\text{s}$, $T_L=298\text{k}$)" [1]. The reference numbers inside the table refer to the original source reference list, and are not listed in this report.

Investigators	Expressions for total specific energy input rate	Value of total specific energy input rate (W/t)
Nakanishi <i>et al.</i> ⁽⁴⁷⁾	$\frac{0.0285 \cdot QT_L}{W} \log\left(1 + \frac{L}{148}\right)$ [L (cm); Q (NI/min); W (t)]	14.54
Themelis and Stapurewicz ⁽⁵³⁾	$\frac{742 \cdot QT_L}{W} \ln\left(1 + \frac{L}{10.34}\right)$ [for water model only; Q (m^3/s)]	2.5
Mazumdar and Guthrie ⁽⁵⁶⁾	$\frac{\rho_L g Q L}{\rho_L \pi R^2 L}$ [Q (m^2/s)]	1.13
Sinha and Mcnallan ⁽⁵⁸⁾	$\frac{854 \cdot QT_L}{W} \log\left(1 + \frac{\rho_L g L}{P_s}\right)$ [Q (m^3/s)]	1.3
Krishnamurthy <i>et al.</i> ⁽⁵⁵⁾	$\frac{4QP_s T_L}{298.2\pi D^2 L} \ln\left(1 + \frac{\rho_L g L}{P_s}\right)$ [Q (Nm^3/s)]	1.29

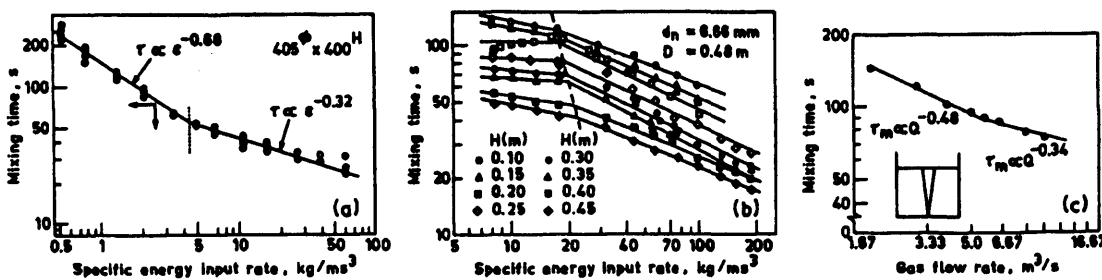


Figure-16. Relationship between mixing time and specific energy input rate/gas flow rate reported in the literature [1]. The figure key is not defined in reference (1). However, the parameters (τ), (Φ), (Q), and (H) can be the specific input energy, vessel diameter, gas flow rate, and vessel height respectively.

Han et al. [17] investigated the ladle flow characteristics using a water model with a top layer of oil. The mixing time decreased with the increase of gas flow rate. The presence of the top oil layer inhibited mixing, as illustrated in figure 17. Furthermore, mixing time increased with the increase of the thickness of the top oil layer as shown in figure 18.

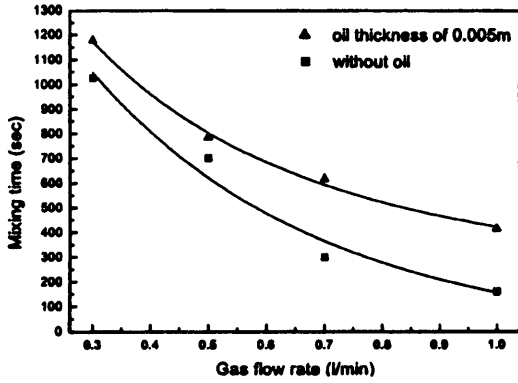


Figure-17. Gas flow rate influence on required mixing time [17].

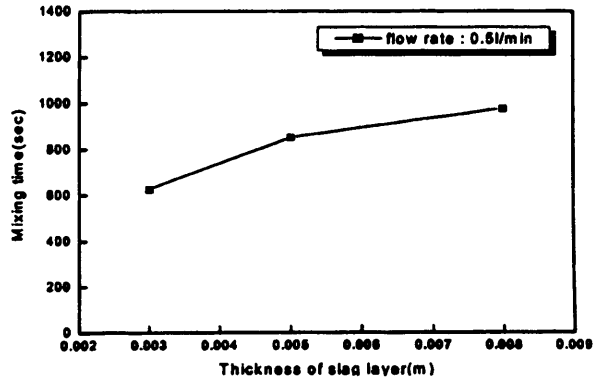


Figure-18. Slag layer thickness influence on mixing time at constant gas flow rate [17].

Figure 19 illustrates the effect of nozzle position on the required mixing time [18], but as discussed earlier, there must be sufficient distance between the wall side and the nozzle position to avoid extensive erosion/corrosion of the refractory lining.

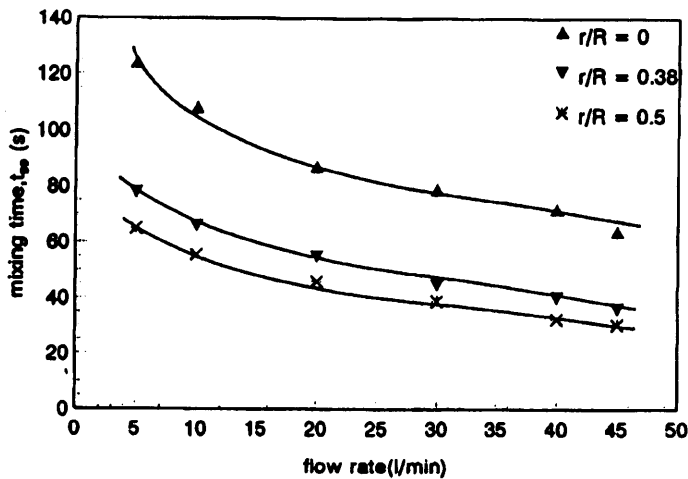


Figure-19. Nozzle position influence of mixing time [18]. The vessel radius value is R, and r is a point in the radius.

The reactions, which occur between the gas bubbles and the bulk liquid, play an important role in the removal of dissolved gases such hydrogen and nitrogen from the molten steel. Therefore, the gas injection device is playing an important role in the absorption rate in the system. A porous plug enhances significantly the gas absorption rates in comparison to a tuyere injection device. With a porous plug, a uniform distribution of small gas bubbles are obtained; this enhances the gas/liquid mass transfer rate due to the increase of the interfacial area between the gas and the bulk liquid (in comparison with a tuyere injection device). The mass transfer phenomenon between slag and molten steel in a gas stirred ladle was investigated using water models [1].

In a water-oil model, a flow visualization of the mixing zone between the bulk liquid and the buoyant phases was investigated as sketched in figure 20. It was found that a high gas flow rate led to a significant disturbance of the water oil interface, resulting in the creation of oil ligaments, droplets and entrainment, etc. In contrast, the interface would remain intact with a relatively low flow rate. However, the creation of the oil ligaments and droplets at the interface would result in a significant increase of the interfacial area, which enhances the mass transfer rate. Therefore, the gas flow rate must lie in the optimum range to provide sufficient mixing at the interface between the slag top layer and the bulk molten steel without any significant disturbance of the interface. Figure 21 illustrates the mass transfer coefficient as a function of gas flow rate [1].

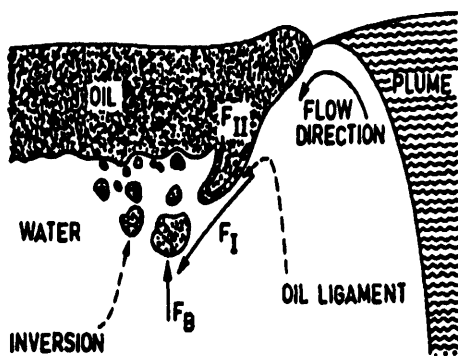


Figure-20. Schematic of plume, water, and oil top layer interaction in water-oil model [1].

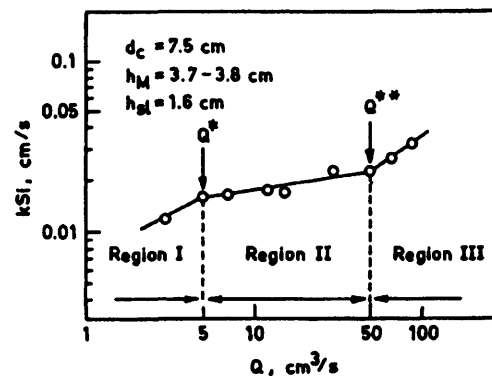


Figure-21. Influence of gas flow rate on mass transfer coefficient in gas/slag/metal high temperature system [1]. The parameters (d_c) (h_M) and (h_{sl}) are the vessel diameter, melts height and the slag thickness respectively.

More investigation demonstrates experimentally that the mixing between the upper slag and the bulk lower phase depends mainly on the density difference between the two phases. For low-density differences, the remixing was less at the interface and there was less entrainment [1].

Turkoglu and Farouk [4] used the classical Ranz and Marshal [19] heat transfer coefficient correlation to simulate the heat transfer during the ladle treatment. The Ranz and Marshall correlation which is applicable for a wide range of Reynolds number ($Re > 300$) [20] is expressed as follows:

$$Nu = 2.0 + 0.6 \cdot Re^{1/2} \cdot Pr^{1/3} \quad (10)$$

where, Nu = Nusselt number.
 Re = Reynolds number, based on the bubble diameter, liquid phase properties, and the slip velocity.
 Pr = Prandtl number.

A comprehensive theoretical and experimental investigation to study the heat transfer in gas bubble driven systems has been reported by Taniguchi et al. [21, 22]. This study demonstrates clearly that the classical Ranz and Marshall correlation underestimates the heat transfer rates by about 40 to 50% [1, 22]. In 1972, Whitaker [23] proposed a modified version of the classical Ranz and Marshall correlation. The Whitaker correlation produces a better estimation of the heat transfer rates, which become more suitable to be used for high temperature gas stirred bath systems [1]. The Whitaker correlation is expressed as follows:

$$(Nu - 2) = (0.4 \cdot Re^{1/2} + 0.06 \cdot Re^{2/3}) \cdot Pr^{0.4} \cdot \left(\frac{\mu_b}{\mu_o}\right) \quad (11)$$

where the fluid viscosity ratio (μ_b/μ_o) is the ratio of the viscosity evaluated at the mean bulk temperature to the viscosity evaluated at the mean wall temperature.

2.1.4 The role of convection in the molten steel circulation

In the industrial ladle vessel, the refractory lining usually includes an insulation layer to reduce the heat losses to the surroundings. However, due to the high working temperature of the molten steel ($\sim 1600^{\circ}\text{C}$), and the large size of the industrial ladle vessel, the heat losses cannot be eliminated. Therefore, during ladle holding, whilst waiting for processing, temperature variation within the molten steel occurs due to the heat losses from the ladle sidewalls, the ladle bottom and the top slag layer. This variation in temperature results in natural convection within the liquid phase. Xia and Ahokainen [24] conclude that, at an early stage of the ladle holding time, a single flow recirculation is formed where the molten steel flows upward at the ladle central region and downward along the wall side. This single recirculation loop provides the highest flow velocity due to natural convection. However, for holding times of more than 40 seconds more vortices are formed, leading to reduced flow velocity. The flow pattern gradually becomes unstable. Austin et al. [25] report that the flow velocity magnitude of the standing ladle decreases with the holding time as shown in figure 22, and the formed recirculation regions shrink.

Generally, during ladle gas stirring thermal homogenization is occurring. Therefore, the natural convection is eliminated. Furthermore, the maximum velocity magnitude reported by Xia and Ahokainen [24] due to the natural convection phenomena is roughly less than 20% of the maximum velocity magnitude reported by Jonsson and Jönsson [26] for a gas stirred ladle simulation of a similar size (100 tonne).

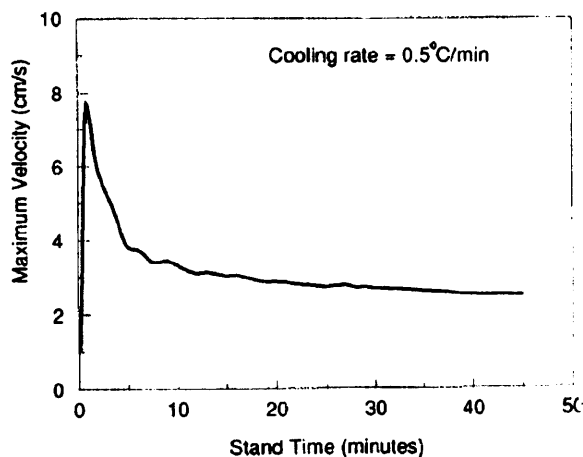


Figure-22. The melt circulation velocity variation with stand time [25].

2.2 The role of the slag in the steelmaking process

The metal sources of iron ores and scrap materials used in steelmaking production are usually mixed with various oxides and sulphides. The unwanted impurities for example, silicates, aluminates, and phosphates, remain as insoluble phases in the primary metal during the process. Furthermore, the product mechanical properties are affected by the presence of these impurities. Slags are designed to extract the unwanted elements from the molten metals. There is an old saying in steelmaking that illustrates the important role of the slag in the steelmaking industry, “Take care of the slag and it will take care of the metal”.

Lime (CaO), bauxite (Al(OH)₃), and dolomite (CaCO₃.MgCO₃) are usually added during molten steel tapping into the ladle vessel to form a suitable slag for desulphurization. This type of slag composition can be reasonably well illustrated using the CaO-Al₂O₃-MgO-SiO₂ system because these components represent more than 95% of the total slag composition. Usually, ladle slag compositions are designed to get close to lime and MgO saturations to achieve a maximum desulphurization potential and reduce slag refractory lining erosion respectively [27].

Herasymenko and Speight [28] established the ionic theory of slag-metal equilibria which considered an ionic slag structure. Molten slags consist of positively and negatively charged ions known as cations, like Ca⁺², and anions, like S⁻², respectively. X-ray and neutron diffraction investigation of glass and slag is the foundation of the knowledge of the slag structure. Silicate and phosphate glass structures are random networks in which the small atoms with a large positive oxidation number, called the “network formers”, such as Si⁺⁴ and P⁺⁵, are tetrahedrally surrounded by oxygen atoms (O⁺²) that form bridges between positive ions. In pure silica, the SiO₄ tetrahedra, sharing with neighbouring tetrahedra form complex networks as illustrated in figure 23, where the slag viscosity increases with the increase of silicate ion size. In steelmaking slag, the acid oxide network structure (SiO₄) is demolished due to the oxygen bridges being broken by the addition of basic oxides such as CaO, as illustrated in figure 24. This addition of basic oxide provides free ionic oxygen that improves the engineering properties of the slag. The acid slag that contains a high concentration of network formers cannot be used to extract impurities such as sulphur

from the melt. This is due to its low capacity for these impurities. Also the acid slags have a high viscosity, which reduces the mass transfer rates. Therefore, sufficient addition of basic oxides provides a molten slag with the required viscosity to achieve the objective of metal refining as a result of the broken network, and also provides free oxygen ions to increase the slag capacity [29-31].

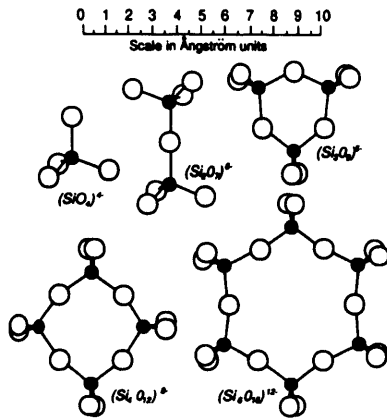


Figure-23. Crystalline silicates [29].

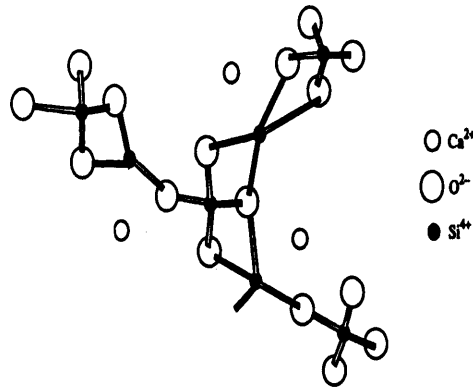


Figure-24. Crystalline silicates [30].

Thermodynamic fundamentals about slag are discussed in section 2.2.1. More details about slag thermo-physical properties and models of ionic melt properties are discussed in sections 2.2.2 and 2.2.3 respectively. Also slag cation diffusivity is discussed in section 2.2.4.

2.2.1 Thermodynamic fundamentals

Metallurgical thermodynamics predicts the possibility of the metallurgical process chemical reactions. All reactions are likely to move towards the thermodynamic equilibrium if sufficient time is provided and there are no kinetic barriers. In steelmaking processes, some of the reactions achieve the thermodynamic equilibrium within the given short time due to the high operation temperature [32].

The slag thermo-physical properties play a major role in the refining process. Therefore, the slag composition used in the modern secondary steelmaking process must be designed carefully to provide the target thermo-physical properties required

for a high quality refining process. Slag basicity and sulphur capacity are essential in the desulphurisation refining process. More details and discussion are given below.

i) Slag basicity

Slag basicity is a ratio between the basic and acid oxides in the slag. Slag basicity control is key to the steel refining process. In the early days, “CaO/SiO₂” was the simplest basicity ratio used by steelmakers, but other oxides were not considered in this ratio such as MgO, Al₂O₃, and FeO, which are often present in steelmaking slag [32]. Ladle furnace slag basicity can therefore be measured using the following mass concentration ratio [33]:

$$B_{LF} = \frac{\%CaO + 1.4 \times \%MgO}{\%SiO_2 + 0.6 \times \%Al_2O_3} \quad (12)$$

The free ionic oxygen present in the slag increases with increasing basicity. Actually, basic oxide dissociates into cations and ionic oxygen in the molten slag [32]. However, in practice, steelmaking slag usually contains undissolved CaO and MgO. Therefore, the slag chemical analysis must be corrected with respect to these oxides. Otherwise, the ratio would give unrealistic values of slag basicity that are much higher than those of the molten fraction of the slag.

Duffy and Ingram were the first to establish the concept of optical basicity (Λ) in 1976, but it was first applied to steelmaking slags in 1978. In the procedure for experimental measurement of optical basicity, a Pb²⁺ is used as a probe ion in the transparent media to trace the frequency changes. The electron donation by oxygen, in the slag, results in a reduction in the (6s-6p) energy gap, and this in turn makes a shift in frequency in the ultraviolet (UV) spectral band [32, 34].

The following empirical correlation was proposed to obtain the optical slag basicity based on experimental measurements [32, 34].

$$\frac{1}{\Lambda_i} = 1.35(\alpha_i - 0.26) \quad (13)$$

where α_i is the Pauling electro negativity of the cation in a single oxide i . (Λ_i) is known also as theoretical optical basicity ($\Lambda_{th, i}$). However, slag optical basicity can be calculated using the following correlation [32, 34].

$$\Lambda_{th} = \sum X_i' \Lambda_{th, i} \quad (14)$$

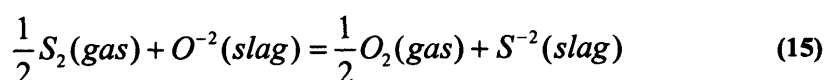
where X_i' is the equivalent cation fraction of oxide i .

Several methods have been published in the literature to estimate the slag optical basicity, but the above correlations are the most widely employed methods.

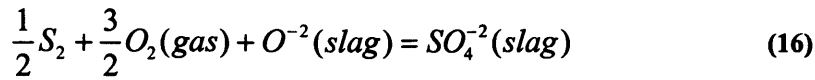
ii) Slag sulphur capacity

In the secondary steelmaking process, calcium-aluminate based slags are widely used in the ladle furnace due to their superior sulphide capacity. Turkdogan [35] showed that the CaF_2 which is added to the slag to achieve a low melting temperature has little or no effect on the sulphide and phosphate capacity of the slag. However, its use is limited because it is corrosive to the regular ladle refractory lining. Also molten slag is usually saturated with MgO for refractory protection [27, 36]. This also probably helps to achieve a fluid slag at steelmaking temperatures despite the high concentration of metal oxides [27, 36, 37]. In practice, according to Schuhmann [36] "it is satisfactory to assume that the behaviour of MgO in slags is substantially the same as that of CaO".

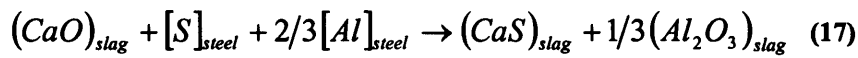
Richardson and Fincham [38] and Richardson [39] have shown that the sulphur is held in the slag totally in the form of sulphide at oxygen partial pressures less than $10^{-5} - 10^{-6}$ atm. Its concentration is controlled by the equilibrium:



At oxygen partial pressures greater than $10^{-3} - 10^{-4}$ atm, then the sulphur is held completely as sulphate and its equilibrium description is:



Furthermore [38, 40], sulphide capacity (C_s) is shown to be constant for a given temperature and composition for oxygen partial pressures less than 10^{-5} - 10^{-6} atm. In the steelmaking industry, the oxygen partial pressure is within the range of 10^{-8} - $10^{-9.2}$ atm. Therefore, the sulphur tends to be present as sulphide rather than sulphate. However, the overall desulphurization reaction for steelmaking refining is expressed as [41].



The solubility of CaS in calcium aluminate melts at 1600°C and lime saturation is (4.77 wt% CaS \equiv 2.12wt% S) [42]. During desulphurization using an insufficient amount of ladle slag, or when refining molten steel with a high sulphur content, the excess CaS which is formed can result in a decrease in the dissolved CaO content of the slag leading to a low rate of desulphurization. However, the local accumulation of sulphide in slag beyond the solubility limit could result in the precipitation of CaS phase [43]. The precipitation of CaS in slag is most likely to be in a solid form given the estimated melting temperature of 2600-3100 °C [44].

Richardson and Fincham [38] and Richardson [39] formulate the slag sulphide capacity (C_s) as a function of gas partial pressures in the molten slag and sulphur concentration present in the slag as:

$$C_s = (wt\%S) \times \left(\frac{P_{O_2}}{P_{S_2}} \right)^{1/2} = K \left(\frac{a_{O^{2-}}}{\gamma_{S^{2-}}} \right) \quad (18)$$

where K is the equilibrium constant for the reaction. Richardson and Fincham suggested this should be defined as follows:

$$K = \left(\frac{a_{S^{2-}}}{a_{O^{2-}}} \right) \times \left(\frac{P_{O_2}}{P_{S_2}} \right)^{1/2} = \frac{(x_{S^{2-}} \cdot \gamma_{S^{2-}})}{a_{O^{2-}}} \times \left(\frac{P_{O_2}}{P_{S_2}} \right)^{1/2} \quad (19)$$

where, a_i and γ_i are the thermodynamic activity of the dissolved element (i) and the activity coefficient of the element (i) respectively. The thermodynamic activity is defined as the ratio between the vapour pressure of components (i) in solution and the vapour pressure of pure components [45]. Thermodynamic activity can also be expressed as [45]:

$$a_i = x_i \cdot \gamma_i \quad (20)$$

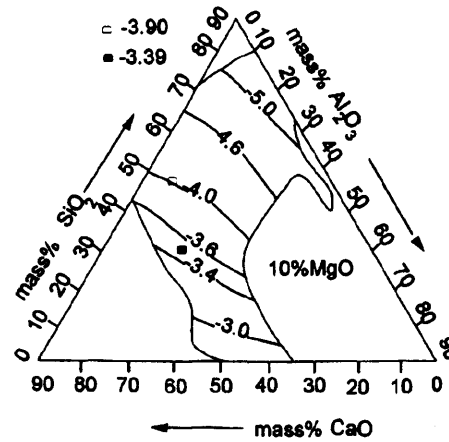
where x_i is the mole fraction of the component (i) in the solution.

2.2.2 Slag thermo-physical properties

Ladle refining is a very dynamic process. The slag composition is usually changing during the process due to inclusion and impurity pickup, reaction with the slag refractory lining, and other reactions. Nzotta et al. [46] reported an increase in the concentration of silica and alumina in the slag during ladle treatment. This is most likely to be due to inclusion absorption by the slag. However the slag chemical analysis used in this study before ladle treatment had shown an average SiO_2 slag content of (17.7 wt%). A recent study showed that the alumina inclusions contain between 10% and 40% silica [47]. Hence, slag composition is varying during the process and this changes its physical and thermal properties to different degrees.

Nzotta et al. [48] illustrate the dramatic effect of CaO concentration changes on sulphur capacity in a slag system containing about 50%wt CaO as shown in figure 25. Generally, slag sulphur capacity is sensitive to temperature and composition variation [48-50], as illustrated in figures 26 and 27.

Figure-25. Iso-sulphide capacity of $\text{Al}_2\text{O}_3\text{-CaO-MgO-SiO}_2$ system with (0.1 wt%) MgO at $T=1873\text{ k}$ [48].



In the field of process metallurgy, *viscosity* is an important melt property that must be measured to study the fluid flow behaviour and the kinetics of the melt-slag-gas reactions. For example, the rate of mass transfer of impurities such as sulphur and phosphorus from molten metals to slag is strongly affected by slag viscosity [51].

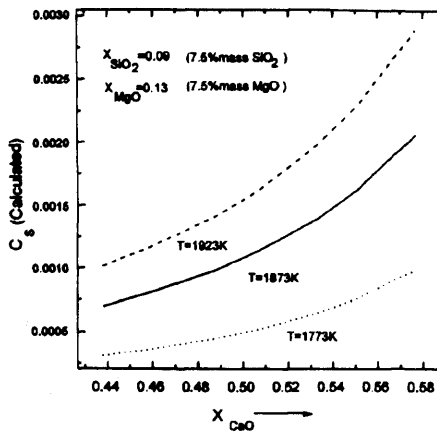


Figure-26. Replacement of Al_2O_3 by CaO influence on slag sulphide capacity at constant content of MgO and SiO_2 . (X_i) is the molar weight of the component (i).

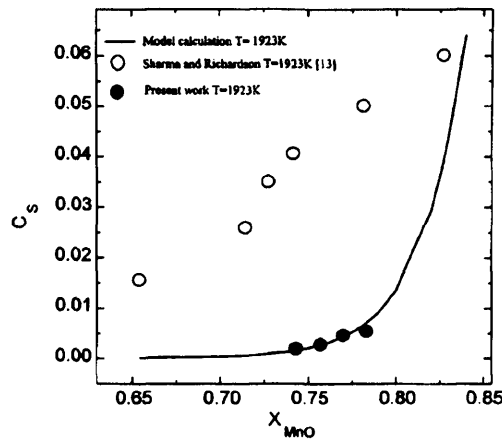


Figure-27. Composition effect on sulphide capacity in the $\text{Al}_2\text{O}_3\text{-MnO}$ system [48]. X_{MnO} is the molar weight.

The mixing zone created at the interface between the slag and the molten steel that is essential for the refining process increases with a decrease in the slag viscosity [51]. However, slag viscosity must be high enough to avoid any entrapment of the slag phase into the molten steel. Numerous investigations of the slag viscosity are reported in the literature. Slag viscosity is found to be very sensitive to temperature and composition changes as illustrated in figure 28.

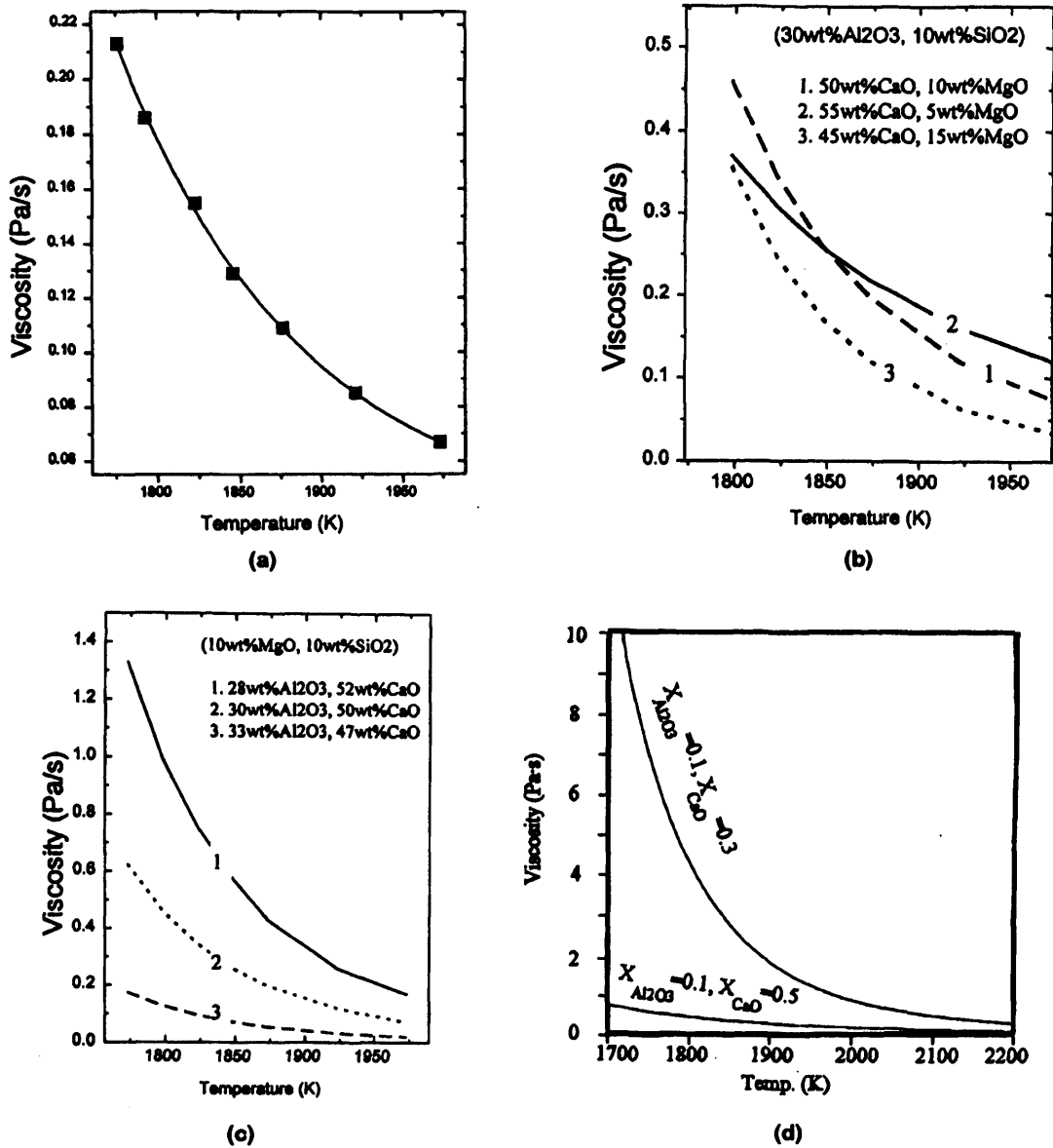


Figure-28. Illustration of slag viscosity sensitivity to temperature and composition variation. (a)- Measured viscosity of (30wt% Al₂O₃-50wt% CaO-7wt% MgO-13wt% SiO₂) slag system as a function of temperature [51]. (b)- Replacement of CaO by MgO influence on the viscosity [51]. (c)- Replacement of CaO by Al₂O₃ influence on the viscosity [51]. (d)- Calculated viscosity of Al₂O₃-CaO-SiO₂ slag system [67], where X is the molar weight.

Sulphur and oxygen dissolved in the molten steel have some effect on the slag metal interface tension. However, the oxygen has a greater effect [52]. Generally, the slag metal interface tension is influenced by the variation of the slag composition and temperature [52-54]. However, a constant interface tension value was suggested and applied in the multi-phase simulation models reported in the literature [2, 26].

2.2.3 Models of ionic melt properties

In the field of metallurgical process simulation, usually reliable extrapolations of the available experimental data over a wide range of temperature and slag compositions are required for effective simulation. Due to the complex nature of slag structure usually some of its properties like sulphur capacity and viscosity are sensitive to temperature and composition variation as illustrated above. Many mathematical models of slag melt properties have been reported with different degrees of complexity and success. Two models suggested by Nilsson et al. [50] and Sichen et al. [55] are described below to simulate slag sulphur capacity and viscosity respectively.

i) Slag sulphur capacity

As illustrated in the Slag Atlas [34], Sosinsky and Sommerville derived a temperature dependence correlation to describe the slag sulphur capacity over a range of optical basicity, but Young (in the Slag Atlas) has shown that this correlation is only applicable over a limited range of optical basicity and provides two correlations applicable for other ranges of optical basicity.

Nilsson et al. [50] established a mathematical model to predict the sulphur capacity as a function of temperature and slag composition. According to Nilsson et al. the equilibrium constant for the reaction (15), $[\frac{1}{2}S_2 + O^{2-} = \frac{1}{2}O_2 + S^{2-}]$, can be expressed as follows.

$$K = \exp\left(\frac{-\Delta G}{RT}\right) \quad (21)$$

where ΔG is the standard Gibbs energy change of the reaction. The Gibbs function difference is the driving force for phase change, just as the temperature difference is the driving force for heat transfer [56]. R and T are the gas constant and temperature in (K) respectively. Furthermore the authors provide a new expression of the $(a_{O^{2-}} / \gamma_{S^{2-}})$ ratio.

$$\left(\frac{a_{o^{2-}}}{\gamma_{s^{2-}}}\right) = \exp\left(-\frac{\xi}{RT}\right) \quad (22)$$

The ξ parameter is a polynomial function of both temperature and composition for a multi-component system and is expressed as:

$$\xi = \sum x_i \xi_i + \xi_{mix} \quad (23)$$

By combining equations 18, 21, and 22, the sulphide capacity, C_s , can be expressed as follows:

$$C_s = \exp\left(-\frac{\Delta G^\circ}{RT}\right) \exp\left(-\frac{\xi}{RT}\right) \quad (24)$$

where the subscript i denotes component i , and (x_i) is the mole fraction of this component in the system. The first term of the equation represents the “linear” variation of ξ for the pure component without considerations of any interaction with other components of the system. The second term represents the interaction between the different species of the system. In order to make reliable model predictions of sulphide capacities of multi-component slag, the model parameters up to ternary interactions should be used. Based on experimental studies, Nzotta et al. [48] optimized the model parameters of the multi-component slag system [Al₂O₃-CaO-MgO-MnO-SiO₂]. The model parameters of the multi-component slag system [Al₂O₃-CaO-MgO-SiO₂] used for this work exclude the MnO component and are presented in table 3. The term y_i shown in the table is the cation fraction of cation (i), defined as the number (N) of cation (i) over the total number of the system cations:

$$y_i = \frac{N_i}{\sum_{j=1}^n N_j} \quad (25)$$

Table-3. Slag sulphur capacity model parameters [48].

Unary	ξ
Al ₂ O ₃	1.57705276x10 ⁵
CaO	-3.3099425x10 ⁴
MgO	9.57307326x10 ³
SiO ₂	1.68872587x10 ⁵
Binary interaction	$\xi_{interaction}$
Al ₂ O ₃ -CaO	$y_{Al^{3+}} y_{Ca^{2+}} [9.82827968 \times 10^4 + 55.07340941 \times T]$
Al ₂ O ₃ -SiO ₂	$y_{Al^{3+}} y_{Si^{4+}} [1.86850468 \times 10^5]$
CaO-SiO ₂	$y_{Ca^{2+}} y_{Si^{4+}} [9.72717695 \times 10^4 + 72.8749746 \times T]$
MgO-SiO ₂	$y_{Mg^{2+}} y_{Si^{4+}} [6.97403222 \times 10^5 - 2.24084556 \times 10^2 \times T]$
Ternary interaction	$\xi_{interaction}$
Al ₂ O ₃ -CaO-MgO	$y_{Al^{3+}} y_{Ca^{2+}} y_{Mg^{2+}} [4.1659555 \times 10^6 - 1.0665663 \times 10^3 \times T - 3.04080189 \times 10^6 \times y_{Al^{3+}}]$
Al ₂ O ₃ -CaO-SiO ₂	$y_{Al^{3+}} y_{Ca^{2+}} y_{Si^{4+}} [-2.03579264 \times 10^6 + 6.86044695 \times 10^2 \times T]$
Al ₂ O ₃ -MgO-SiO ₂	$y_{Al^{3+}} y_{Mg^{2+}} y_{Si^{4+}} [1.56192588 \times 10^5 - 2.90498555 \times 10^2 \times T + 9.49447247 \times 10^5 \times y_{Al^{3+}}]$
CaO-MgO-SiO ₂	$y_{Ca^{2+}} y_{Mg^{2+}} y_{Si^{4+}} [-1.52649771 \times 10^6 + 6.25663842 \times 10^2 \times T + 1.48525598 \times 10^6 \times y_{Ca^{2+}}]$

The ξ expression for the slag system [Al₂O₃-CaO-MgO-MnO-SiO₂] is presented below. This can be down-graded to a lower order system, when the absent component mole and cation fractions are set to zero.

$$\begin{aligned}
\xi = & X_{Al_2O_3} \xi_{Al_2O_3} + X_{CaO} \xi_{CaO} + X_{MgO} \xi_{MgO} + X_{MnO} \xi_{MnO} + X_{SiO_2} \xi_{SiO_2} \\
& + \xi_{interaction}^{Al_2O_3-CaO} + \xi_{interaction}^{Al_2O_3-SiO_2} + \xi_{interaction}^{Al_2O_3-MnO} + \xi_{interaction}^{CaO-SiO_2} \\
& + \xi_{interaction}^{MgO-SiO_2} + \xi_{interaction}^{MnO-SiO_2} + \xi_{interaction}^{Al_2O_3-CaO-MgO} + \xi_{interaction}^{Al_2O_3-CaO-SiO_2} \\
& + \xi_{interaction}^{Al_2O_3-MgO-SiO_2} + \xi_{interaction}^{Al_2O_3-MgO-MnO} + \xi_{interaction}^{Al_2O_3-MnO-SiO_2} \\
& + \xi_{interaction}^{CaO-MgO-SiO_2} + \xi_{interaction}^{CaO-MnO-SiO_2} + \xi_{interaction}^{MgO-MnO-SiO_2}
\end{aligned} \tag{26}$$

The results reported in the literature show a reliable prediction of sulphur capacity with good agreement with the experimental measurement for different slag systems including (CaO-Al₂O₃-SiO₂-MgO) [48-50, 57].

ii) Slag viscosity

In simulation of the role of the slag in the metallurgical process, usually a huge amount of data on slag thermal properties is required over a wide range of complex slag compositions and temperatures to run the model. Various workers show dramatic increases in slag viscosity with the content of network formers such as SiO₂ that come within the range (1-100 Ns/m²) [30, 58-60], as illustrated in figure 29.

Unfortunately the available experimental results do not provide enough data over this wide range of complex compositions and temperature to run very dynamic models. The need for mathematical models that enable the estimation of the viscosities of complex slags systems is noticeable.

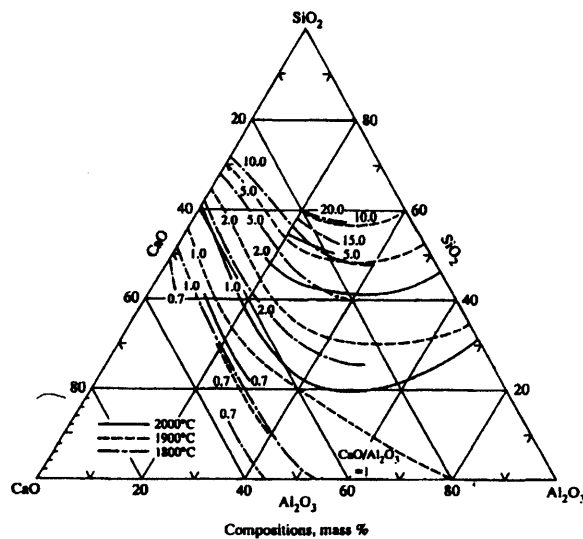


Figure-29. Isoviscosity lines of the slag system (CaO-Al₂O₃-SiO₂) at temperature 1500 °C, given in Poise (1 poise = 0.1 Ns/m²) [30].

A great effort has been made and a number of models have been developed [61]. Mills et al. [62] ran a “round robin” project to determine the accuracy of the prediction of the slag viscosities and the reliability of various sophisticated models. The different types of industrial slag were classified into various groups such as

mould slag, ladle slag, and more. The model performance was described by the difference between the calculated and the measured slag viscosities as per the formula below:

$$\delta = \frac{\eta_{cal} - \eta_{mea}}{\eta_{mea}} \times 100 \quad (27)$$

$$\Delta = \frac{1}{N} \sum |\delta| \quad (28)$$

where δ and Δ are the parameters describing the variation between the calculated and the measured values of the slag viscosity. Also η_{cal} and η_{mea} are the calculated and measured slag viscosity respectively. N is the number of samples.

More than ten models applicable for different slags were investigated in the “round robin” project. However, in this present work, the ladle slag system for the desulphurization process is of concern; this is a non-fluoride system. For such a non-fluoride slag system, the “round robin” project found Δ parameters of around 20% for Zhang and Jahanshahi [63] and the Royal Institute of Technology (KTH) [64] models. On the other hand the National Physical Laboratory (NPL) model [65] shows Δ parameter values to be in the range of (25-35%). This is considered to be very reasonable compared with the experimental errors ($\pm 20\%$). Detailed descriptions for each of the above models:- KTH; NPL; and Zhang and Jahanshahi; are given below. Further analysis and discussion of the model compatibility with the CFD analysis is given in section 2.2.3 (iii).

a) KTH slag viscosity model

Sichen et al. [55] developed a mathematical model named the KTH model in the “round robin” project- to estimate the multi-component ionic melt viscosity as a function of temperature and compositions. The composition of the ionic melt is represented by analogy with Temkin’s theory [66]. In this model, the slag viscosity (η) can be expressed as follows:

$$\eta = \frac{hN\rho}{M} \cdot \exp\left(\frac{\Delta G^*}{RT}\right) \quad (29)$$

where h = Planck's constant.
 N = Avogadro's number.
 ρ = Density of slag.
 M = Molecular weight.
 ΔG^* = Gibbs energy of activation per mole, calculated from experimental viscosity data.

The molecular weight of the melt can be expressed as follows:

$$M = \sum X_i \cdot M_i \quad (30)$$

where X_i and M_i represent the mole fraction and the molecular weight of the component (i) in the solution, respectively. Also, the density of the multi-component melt in the model is expressed as follows:

$$\rho = \sum X_i \cdot \rho_i \quad (31)$$

where ρ_i is the density of the pure components (i) in the liquid state.

ΔG^* in equation (29) can be expressed as follows:

$$\Delta G^* = \sum X_i \Delta G_i^* + \Delta G_{mix}^* \quad (32)$$

where ΔG_i^* is the Gibbs energy of activation of the pure component (i) in the liquid state which is usually a linear function of temperature. The second term on the right side of equation (32) represents the interaction between different species. More details are presented elsewhere [55, 67].

The model prediction shows good agreement with the experimental results, and good reliability in extrapolating the viscosity values of complex slag systems as a function of temperature and composition [55, 67]. The expression of the Gibbs energies for the viscosity for the system, for example, (CaO-Fe_nO-MgO-SiO₂) is as follows [68].

$$\begin{aligned} \Delta G^*(CaO - Fe_nO - MgO - SiO_2) = & \\ [X_{CaO}\Delta G_{CaO}^* + X_{Fe_nO}\Delta G_{Fe_nO}^* + X_{MgO}\Delta G_{MgO}^* + X_{SiO_2}\Delta G_{SiO_2}^*] + \Delta G_{Mix}^*(CaO - SiO_2) & \quad (33) \\ + \Delta G_{Mix}^*(Fe_nO - SiO_2) + \Delta G_{Mix}^*(MgO - SiO_2) + GCAFESI + GCAMGSI + GFEMGSI & \end{aligned}$$

The parameters, ΔG_{CaO}^* , ΔG_{FeO}^* , ΔG_{MgO}^* , ΔG_{MnO}^* , $\Delta G_{SiO_2}^*$, $\Delta G_{Mix}^*(CaO - SiO_2)$, $\Delta G_{Mix}^*(Fe_nO - SiO_2)$, $\Delta G_{Mix}^*(MgO - SiO_2)$, $\Delta G_{Mix}^*(MnO - SiO_2)$, $GCAFESI$, $GCAMGSI$, $GFEMGSI$, and more are illustrated in table 4 and table 5. Unfortunately, the model parameters for the Al₂O₃ component are not published in the open literature at the time of issue this report due to copyright restrictions. Therefore, this slag viscosity model cannot be implemented in the current ladle degassing system simulation model.

Table-4. Slag viscosity mathematical model parameters.[68]

Component <i>i</i>	Density (g/cm ³)	Molar weight (g/mol)	ΔG_i^* (J/mol)
CaO	3.3	56.079	1.853x10 ⁵
Fe _n O	4.7	71.846	1.3371x10 ⁵ -18.033.T
MgO	3.58	40.311	1.865x10 ⁵
MnO	5.43	70.937	1.327x10 ⁵
SiO ₂	2.3	60.085	5.331x10 ⁵ -53.298.T

Table-5. Slag viscosity mathematical model parameters.[68]

ΔG_{Mix}^* (J/mol)	
<i>Binary Interaction</i>	
CaO-SiO₂	$\Delta G_{Mix}^* (CaO - SiO_2) = y_{Ca}^{2+} y_{Si}^{4+} [-8.56218889 \times 10^5 + 103.733092 \cdot T + 2.64594343 \times 10^5 (y_{Ca}^{2+} - y_{Si}^{4+})]$
Fe_nO-SiO₂	$\Delta G_{Mix}^* ([Fe_nO - SiO_2]) = y_{Fe}^{2+} y_{Si}^{4+} [-9.70281422 \times 10^5 + 242.480930 \cdot T + 1.90586769 \times 10^5 (y_{Fe}^{2+} - y_{Si}^{4+})]$
MgO-SiO₂	$\Delta G_{Mix}^* (MgO - SiO_2) = y_{Mg}^{2+} y_{Si}^{4+} [-8.18430330 \times 10^5 + 91.3638027 \cdot T + 1.35009560 \times 10^5 (y_{Mg}^{2+} - y_{Si}^{4+})]$
MnO-SiO₂	$\Delta G_{Mix}^* (MnO - SiO_2) = y_{Mn}^{2+} y_{Si}^{4+} [-7.30955356 \times 10^5 + 85.8415806 \cdot T - 7.47554681 \times 10^4 (y_{Mn}^{2+} - y_{Si}^{4+})]$
<i>Ternary Interaction</i>	
CaO-Fe_nO-SiO₂	$\begin{aligned} \Delta G_{Mix}^* (CaO - Fe_nO - SiO_2) &= \Delta G_{Mix}^* (CaO - SiO_2) \\ &+ \Delta G_{Mix}^* (Fe_nO - SiO_2) + GCAFESI \\ GCAFESI &= y_{Ca}^{2+} y_{Fe}^{2+} y_{Si}^{4+} (1.14932406 \times 10^6 - 139.466890 \cdot T \\ &- 1.05268958 \times 10^6 y_{Ca}^{2+} - 1.18703224 \times 10^6 y_{Fe}^{2+}) \end{aligned}$
CaO-MgO-SiO₂	$\begin{aligned} \Delta G_{Mix}^* (CaO - MgO - SiO_2) &= \Delta G_{Mix}^* (CaO - SiO_2) \\ &+ \Delta G_{Mix}^* (MgO - SiO_2) + GCAMGSI \\ GCAMGSI &= y_{Ca}^{2+} y_{Mg}^{2+} y_{Si}^{4+} (1.07014539 \times 10^6 - 324.501809 \cdot T) \end{aligned}$
CaO-MnO-SiO₂	$\begin{aligned} \Delta G_{Mix}^* (CaO - MnO - SiO_2) &= \Delta G_{Mix}^* (CaO - SiO_2) \\ &+ \Delta G_{Mix}^* (MnO - SiO_2) + GCAMNSI \\ GCAMNSI &= y_{Ca}^{2+} y_{Mn}^{2+} y_{Si}^{4+} (-6.75779022 \times 10^5 + 504.161763 \cdot T) \end{aligned}$
Fe_nO-MgO-SiO₂	$\begin{aligned} \Delta G_{Mix}^* (Fe_nO - MgO - SiO_2) &= \Delta G_{Mix}^* (FeO - SiO_2) \\ &+ \Delta G_{Mix}^* (MgO - SiO_2) + GFEMGSI \\ GFEMGSI &= y_{Fe}^{2+} y_{Mg}^{2+} y_{Si}^{4+} (7.83484279 \times 10^5 - 271.089792 \cdot T) \end{aligned}$
Fe_nO-MnO-SiO₂	$\begin{aligned} \Delta G_{Mix}^* (Fe_nO - MnO - SiO_2) &= \Delta G_{Mix}^* (FeO - SiO_2) \\ &+ \Delta G_{Mix}^* (MnO - SiO_2) + GFEMNSI \\ GFEMNSI &= y_{Fe}^{2+} y_{Mn}^{2+} y_{Si}^{4+} (1.66129998 \times 10^6 - 891.715429 \cdot T) \end{aligned}$

b) NPL slag viscosity

Mills and Sridhar [65] in the NPL slag viscosity model, which is based on the corrected optical basicity [69], provide a reasonable estimation over a wide range of industrial slags. The model assumes Arrhenius behavior, as expressed by the following correlation:

$$\ln \eta = \ln A + B/T \quad (34)$$

where η is the viscosity. T is the temperature and A and B are functions of the corrected optical basicity (Λ^{corr}) as expressed below:

$$\frac{\ln B}{1000} = -1.77 + \frac{2.88}{\Lambda^{corr}} \quad (35)$$

$$\ln A = -232.69(\Lambda^{corr})^2 + 357.32 \cdot \Lambda^{corr} - 144.17 \quad (36)$$

$$\Lambda^{corr} = \frac{\sum x_i n_i \Lambda_i}{\sum x_i n_i} \quad (37)$$

where x_i and n_i are the component (i) mole fraction and the number of oxygen atoms in the molecule, e.g. one for CaO, respectively. Also, Λ_i is the optical basicity of component (i) as listed in table 6.

Table-6. Slag oxide optical basicity [65].

CaO	Al ₂ O ₃	SiO ₂	MgO	MnO	P ₂ O ₅
1.0	0.60	0.48	0.78	1.0	0.40

c) Zhang and Jahanshahi slag viscosity model

Zhang and Jahanshahi [63, 70] follow a different approach to develop their slag viscosity model. Various models proposed over the past decades were based on the equations for the viscosity of simple liquids, such as Weymann's equation. A slag

structural related model was developed. In this approach, the slag viscosity is linked with the degree of polymerization of the silicate melts. It is well known that in silicate melts viscosity decreases with the temperature increases for a given slag composition, also the melt viscosity increases with silica content for a given temperature. Therefore, Zhang and Jahanshahi define some parameters in their model to describe the influence of the temperature and composition on the melt viscosity. The proposed melt viscosity equation is expressed as follows:

$$\eta = A^W T \exp(E_\eta^W / RT) \quad (38)$$

where η is viscosity, A^W and E_η^W are a pre-exponential term and activation energy respectively, T is temperature and R is the gas constant. The viscosity composition dependence is described by the activation energy parameter E_η^W , which can be expressed as follows:

$$E_\eta^W = a + b(N_{O^0})^3 + c(N_{O^0})^2 + d(N_{O^{2-}}) \quad (39)$$

where a, b, c, and d are fitting parameters to be optimized against experimental data. N is the fraction of oxygen, where N_{O^0} and $N_{O^{2-}}$ are the oxygen bonded to two silicon atoms and the free oxygen ion respectively. These parameters can be obtained from experimental data or calculated from molecular dynamics simulations of silicate melts [63]. Also, the pre-exponential term A^W can be expressed as follows:

$$\ln(A^W) = a' + b' E_\eta^W \quad (40)$$

where a' and b' are unique coefficients for a particular system fitting to experimental data. Furthermore, the model was extended successfully to estimate the viscosity of a silicate melt containing alumina [71].

iii) Note on the use of the NPL model in the present work.

The slag viscosity estimation models due to KTH, NPL, and Zhang and Jahanshahi have been described in section 2.2.3 (ii). For the present work, a model must be integrated with the Fluent CFD package. Unfortunately, the KTH model cannot be integrated due to missing parameters covering the presence of Al_2O_3 in slag (in the present work the slag system includes 30 wt% Al_2O_3). This is essentially a copyright issue. The Zhang and Jahanshahi model cannot be implemented because model parameters have been developed specifically for a silicate slag system containing a minimum of 20 wt% SiO_2 (private communication with Dr. Ling Zhang). Therefore, the NPL model was employed in the present work. However, an experimentally determined relation between slag viscosity and temperature was used for some of the cases (see section 3.4).

2.2.4 Cation diffusivity in molten slag

“Diffusion is the process by which matter is transported from one part of a system to another as a result of random molecular motion” [72]. Slag is ionic in nature consisting of positively and negatively charged ions called cations and anions respectively. Cations are mobile species in slag and show much higher diffusivity rate than anions [73]. In addition the diffusivity coefficient of an element is of an order of magnitude greater in a liquid metal than in a molten slag [74, 75]. The diffusion coefficients are influenced by species concentrations in slag. Variations of the species concentration result in composition and viscosity changes of the slag, which in turn alter the coefficient of diffusion. Silicon concentration gradient has a significant influence on species diffusivity in silicate slags [74]. Also, the calcium cation diffusivity coefficient in lime-alumina slag is about four times the value in a silicate slag for the same temperature. In ternary silicate slag, the diffusivities for some cations are in the following order $[D_{\text{Fe}} > D_{\text{Na}} > D_{\text{Ca}} > D_{\text{Al}} > D_{\text{Si}}]$ [76]. In addition diffusivity coefficient variation with temperature gradient is not great [75]. Some of the interesting cation diffusivity coefficient values are given in table 7.

Table-7. Diffusion coefficients for some cations of interest in molten slag.

Slag composition Wt%	Cation	Diffusivity ($\times 10^{-6}$) cm^2/s	Temperature $^{\circ}\text{C}$	Ref
38CaO.20Al ₂ O ₃ .42SiO ₃	Ca	4.5	1450	[75]
	Si	0.047	1365	[76]
	Si	0.105	1430	[76]
50.1CaO.49.9Al ₂ O ₃	Ca ⁺²	19	1450	[75]
40CaO.20Al ₂ O ₃ .40SiO ₃	Ca ⁺²	0.2-0.45	1350	[76]
40CaO.20Al ₂ O ₃ .40SiO ₃	Ca ⁺²	1.5-4.0	1500	[76]

2.3. Gas refining in a ladle degassing system

In the continuous casting process, the subsurface blowholes tend to occur due to the high content of the H, N and CO dissolved in liquid steel [77]. Only a small amount of the hydrogen will diffuse out during the rapid cooling of a heavy casting section of steel. Due to the reduction of hydrogen solubility in steel with temperature drop, hydrogen gas pressure will build up in the steel matrix during the rapid cooling process. Therefore, internal cracking and flaking can occur in heavy sections if the hydrogen content is too high. Nowadays, heavy sections for critical applications are degassed to reduce hydrogen content. On the other hand slow cooling allows the diffusion of hydrogen out of the steel casting [78]. Nitrogen affects toughness and enhances the tendency for stress corrosion cracking [79].

During vacuum treatment process, the dissolved hydrogen is transferred from the liquid metal into the argon gas bubbles. In contrast, slag picks up hydrogen from the atmosphere and transfers it to the liquid metal. Actually, the slag hydrogen pickup is a result of the reaction of the slag with water vapour; hydrogen gas does not dissolve in significant amounts in slag [80]. Due to the moisture content of the lime-base slag [CaO-Al₂O₃-SiO₂-MgO], the initial hydrogen level is most likely to increase during the desulphurization process according to the reaction ($\text{H}_2\text{O} = 2[\text{H}] + [\text{O}]$) with the liquid steel [81].

The hydrogen removal mechanism in the degassing system gas stirred ladle can be described in three steps. First, the dissolved hydrogen in molten metal comes into contact with the argon gas bubbles. Secondly, hydrogen gas is formed at the surface

of the argon gas bubbles according to the chemical reaction ($2[\text{H}] = \text{H}_2 (\text{gas})$). Finally, the mass transfer of the gas formed into the argon gas bubbles. At steelmaking temperatures, the chemical reactions are usually very fast. The hydrogen gas formation at the bubble surface is occurring much faster compared to the hydrogen mass transfer in the liquid metal [82]. Therefore, the hydrogen removal rate is controlled by how fast the hydrogen rich steel can be transported into the gas plume region [82, 83]. In other words, the first step of the mechanism is controlling the hydrogen removal rate.

During the vacuum oxygen decarburization (VOD) process, Kitamura et al. [84] assumed that the nitrogen removal was controlled by the mass transfer of dissolved nitrogen in the liquid steel and by the chemical reaction [$2[\text{N}] = \text{N}_2 (\text{gas})$] occurring at the interface with the gas bubbles. Kitamura et al. [84] concluded that the early stage of the decarburization chemical reaction mainly happened at the interface with CO bubbles; however, as the CO bubble formation decreases during the process, then 70% of nitrogen gas formation occurred at the bath surface and only 30% occurred at the interface with the injected argon gas bubbles.

2.4. Gas stirred system simulation

Multiphase fluid flow modelling has received enormous attention over the last few years. Many mathematical models of the two-phase gas stirred system have been reported in the literature. The plume phase was predicted from first principles with good agreement with the experimental results. The transport equations were solved for each phase and connected with interaction parameters. The Launder and Spalding [85] $k-\varepsilon$ turbulent model is widely used in the field of gas stirred ladle system simulation.

Ilegbusi and Szekely [3] report results of a mathematical prediction of a gas stirred system with an excellent agreement with the experimental measurements as illustrated in figure 30. Furthermore, their mathematical model predicts a much narrower plume width for molten steel in comparison with the water model. More mathematical models studying different phenomena within the gas stirred system by solving the transport equations have been reported in literature with good prediction results [4,

17, 86-88]. However, recently a three phase model of a gas stirred bath including the top slag layer, has been developed by Jonsson and Jönsson [26]. The agreement of the steel surface velocity prediction with the experimental measurement was five times better than their previous two phase simulation model which had not considered the slag phase. The model was capable of predicting the slag and molten steel fractions in the mixing zone.

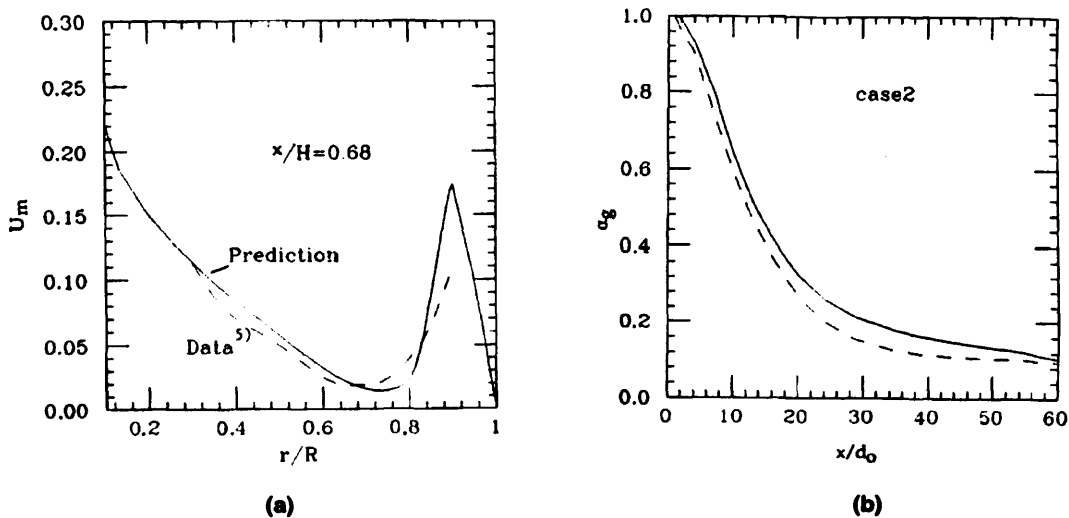


Figure-30. Mathematical model prediction compared with experimental measurement [3]. (a) Mean axial liquid velocity at 68% of the total liquid height from the vessel bottom ($x/H=0.68$). (b) Gas fraction variation along the axis in water model measurement and model prediction. (R) is the vessel radius and (r) is a point located on the radius. (d_0) is the axis length and x is a point on the axis.

Jonsson et al. [2] established a new approach to steel refining simulation. The multi-phase steel/slag/gas model was linked with a thermodynamic database to simulate the desulphurization process. The desulphurization thermodynamic equations were solved for each node every instant. However, some simplifications were made.

- Only the effect of aluminium, oxygen and sulphur dissolved elements were accounted for in the desulphurization, based on the assumption that the concentrations of other elements do not change significantly during the process.
- The oxygen activity was determined only by the aluminium and alumina activity in the melt and slag respectively; these activities were used to determine the sulphur partition ratio between the melt and the slag.

- Thermodynamic equilibrium was assumed to be achieved at each time step of the process.

The mass balance for each dissolved element (Al, O, and S) was determined at each time step based on the predictions of the thermodynamic changes.

The prediction results were in acceptable agreement with plant data. The success of the model illustrates the great potential of coupling the CFD analysis with thermodynamic modelling. Figures 31 and 32 show the predictions of sulphur concentration variation with refining time as well as other dissolved element content changes in molten steel as a result of the desulphurisation process.

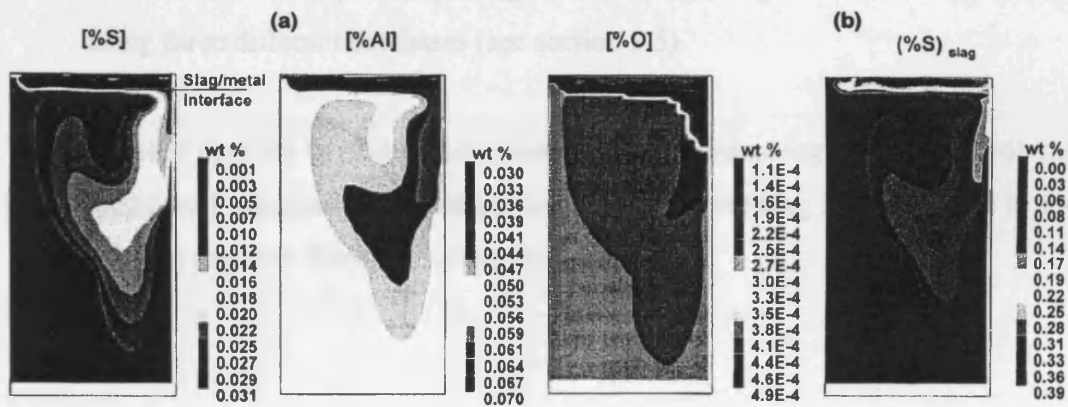


Figure-31. The sulphur, aluminium and oxygen content in molten steel phase, and sulphur content in slag phase 1 min after of the gas stirring process started [2].

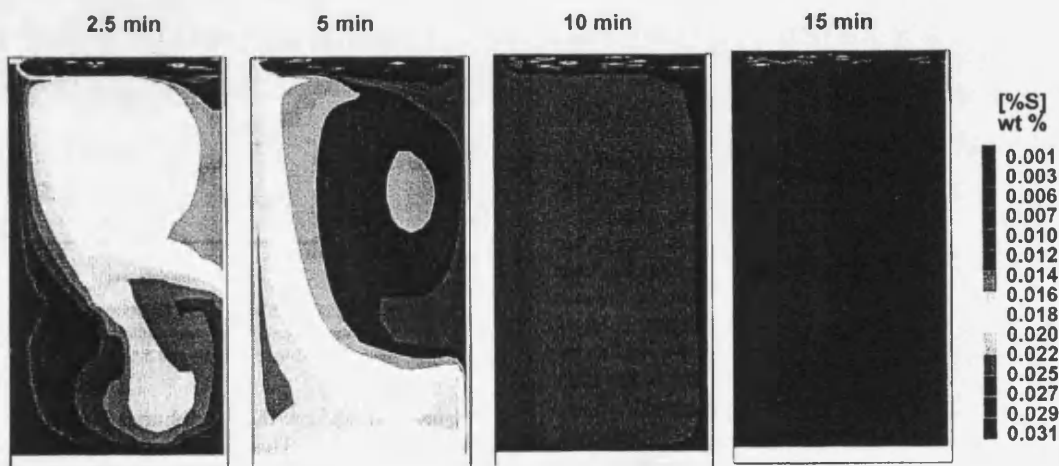


Figure-32. The sulphur content in molten steel changes with refining time [2].

The same model approach with some modifications was applied elsewhere for further investigation of other applications within gas stirred ladle systems with great success [83, 89-92].

In this present work which will be described in the next chapter some features are:

- Addition of a vacuum zone on the top of the slag layer, to avoid restricted heat losses from the top surface, and provide more freedom for the slag phase motion.
- Advanced thermodynamic prediction with minimal assumptions using the MTDATA thermodynamic package from National Physical Laboratory (NPL), using three different databases (see section 3.5).
- An easy upgrade to study more phenomena in steelmaking processes involving slag-metal reactions e.g. decarburisation at the steel/slag interface, due to the use of a separate thermodynamic package.

3. Simulation of the ladle gas stirred system

The aim of this project is to make a coupling between the ladle degassing system CFD model and the thermodynamic prediction package. A three phase (steel/gas/slag) mathematical model is developed using the Fluent commercial CFD package. MTDATA is used to predict the species exchange at the metal/slag interface. The CFD mathematical formulation and boundary conditions used are described in sections 3.1 and 3.2 respectively. The role of the drag coefficient correlation is discussed in section 3.3. More about the coupling methodology and the model development is discussed in sections 3.6 and 3.7 respectively.

3.1 Mathematical formulation

A 2D mathematical model of a gas-stirred ladle accounting for the steel, argon and slag phases was created as illustrated in figure 33. The Eulerian multiphase model approach was used to solve separate transport equations for each of the dissolved elements of interest such as Al, O, and S. Additional species (Ca^{++} and CaS) were accounted for when allowing Ca^{++} mobility and the precipitation of CaS phase in the slag phase. The simulation assumptions are described in section 3.1.1. A detailed list of the implemented transport equations is given in section 3.1.2.

3.1.1 Assumptions:

The simulation was based on the following assumptions:

- The ladle vessel is a symmetric system;

- The transient solution approach (as defined in Fluent) was used to run the simulation;
- A free vacuum zone occupied by gas on the top of the slag layer was assumed [4]. The return gas temperature at the outlet surface was assumed a constant. This temperature value was taken from steelmaking plant of a similar system;

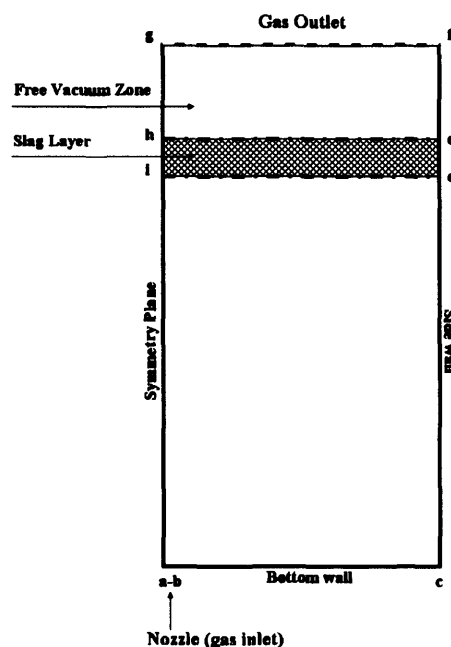


Figure-33. Schematic diagram of the two dimensional control volume domain of the gas stirred ladle system

- A non-slip boundary condition was assumed at the ladle sidewall and the bottom. An enhanced wall treatment provided by Fluent was used to define the velocity profile, turbulent kinetic energy, energy dissipation rate, and turbulent viscosity in the region near the wall. This method combines a two-layer model with enhanced wall functions. The two-layer model is an integral part of the Fluent enhanced wall treatment approach and is used to specify both the turbulent kinetic energy dissipation rate and the turbulent viscosity in the near-wall cells. The enhanced wall function is an amalgamation of the turbulent and laminar wall flows to obtain a

reasonable representation of velocity profiles and resolve the different conditions near the wall region (i.e., laminar sub-layer, buffer region, and fully-turbulent region). A constant heat loss rate (24600 W/m²) from the molten steel to the refractory lining was assumed [2];

- A homogeneous molten steel and slag composition and temperature were assumed as an initial condition prior to calculation;

3.1.2 Transport equations:

Based on the above assumptions in section 3.1.1, the following transport equations were solved to conduct the simulation.

- Mass conservation equation for each single phase and dissolved elements of interest.

$$\frac{\partial \rho}{\partial t} + \nabla \cdot (\rho \vec{v}) = S_m \quad (41)$$

where \vec{v} is velocity. Equation (41) is the general form of the mass conservation equation, where S_m is the source mass term.

- Momentum equation

$$\frac{\partial}{\partial t} (\rho \vec{v}) + \nabla \cdot (\rho \vec{v} \vec{v}) = -\nabla p + \nabla \cdot (\bar{\tau}) + \rho \vec{g} + \vec{F} \quad (42)$$

where p is the static pressure, $\bar{\tau}$ is the stress tensor described below, and $\rho \vec{g}$ and \vec{F} are the gravitational and external body forces respectively.

$$\bar{\tau} = \mu \left[\left(\nabla \vec{v} + \nabla \vec{v}^T \right) - \frac{2}{3} \nabla \cdot \vec{v} I \right] \quad (43)$$

where μ is the molecular viscosity, I is the unit tensor, and the second term on the right hand side is the effect of volume dilation.

- Energy conservation equation

$$\frac{\partial}{\partial t}(\rho E) + \nabla \cdot (\vec{v}(\rho E + p)) = \nabla \cdot (k_{\text{eff}} \nabla T - \sum_j h_j j_j + (\bar{\tau}_{\text{eff}} \cdot \vec{v})) + S_h \quad (44)$$

where k_{eff} is the effective conductivity, h_j and j_j are the sensible enthalpy and the diffusion flux of species j respectively, and S_h is the volumetric heat source e.g. heat of chemical reaction..

The turbulent flow was solved using a k - ε model [85]. The turbulence kinetic energy, k , and its rate of dissipation, ε , are obtained from the following transport equations:

$$\frac{\partial}{\partial t}(\rho k) + \frac{\partial}{\partial x_i}(\rho k u_i) = \frac{\partial}{\partial x_j} \left[\left(\mu + \frac{\mu_t}{\sigma_k} \right) \frac{\partial k}{\partial x_j} \right] + G_k + G_b - \rho \varepsilon - Y_M + S_k \quad (45)$$

$$\frac{\partial}{\partial t}(\rho \varepsilon) + \frac{\partial}{\partial x_i}(\rho \varepsilon u_i) = \frac{\partial}{\partial x_j} \left[\left(\mu + \frac{\mu_t}{\sigma_\varepsilon} \right) \frac{\partial \varepsilon}{\partial x_j} \right] + C_{1\varepsilon} \frac{\varepsilon}{k} (G_k + C_{3\varepsilon} G_b) - C_{2\varepsilon} \rho \frac{\varepsilon^2}{k} + S_\varepsilon \quad (46)$$

where u_i is the velocity tensor, and μ_t is the turbulent viscosity described as:

$$\mu_t = \rho C_\mu \frac{k^2}{\varepsilon} \quad (47)$$

$C_{1\varepsilon}$, $C_{2\varepsilon}$, $C_{3\varepsilon}$, σ_k , and σ_ε are the model constants shown in table 8. These constants have been estimated to fit a water/air experimental measurements, and its used widely in the field of steelmaking process simulation [93, 94].

Table-8. The K - ϵ turbulent model constants [85].

$C_{1\epsilon}$	$C_{2\epsilon}$	$C_{3\epsilon}$	C_μ	σ_k	σ_ϵ
1.44	1.92	1.3	0.09	1.0	1.3

G_k is the generation of turbulence kinetic energy due to the mean velocity gradients, described as per the following equation.

$$G_k = -\rho \overline{u_i u_j} \frac{\partial u_j}{\partial x_i} \quad (48)$$

where $\overline{u_i u_j}$ is the Reynolds stress. The term (Y_M) represents the influence of the compressible flow on the overall dissipation rate that is usually neglected for incompressible flow, as in the present model.

For a non-zero gravity field and temperature gradients, the generation of the turbulence kinetic energy due to buoyancy is accounted for by the term G_b expressed in equation (49). In Fluent, the influence of the buoyancy on the production of k is well known and can be described by the term G_b . On the other hand, its influence on the production of ϵ is less clear. Therefore, the term G_b is set to zero in equation (46) to neglect the buoyancy influence. However, it can be accounted for if required.

$$G_b = \beta g_i \frac{\mu_t}{Pr_t} \frac{\partial T}{\partial x_i} \quad (49)$$

where Pr_t is the turbulent Prandtl number and g_i is the gravity vector in the i th direction, and β is the thermal expansion coefficient.

The turbulent Prandtl number (Pr_t) is defined as the ratio of the eddy diffusivity of momentum to eddy diffusivity of heat. Turbulent Prandtl number for fluids with very low Prandtl number ($Pr \ll 1$) such as liquid metals, is noticeably greater than 1.0 [95-97]. A proper estimation of Pr_t is important to accurately predict the heat transfer rate by solving the energy equation [95]. Figure 34 illustrates the variation of Pr_t moving away from the wall in a fully developed flow in a flat duct for different Prandtl numbers.

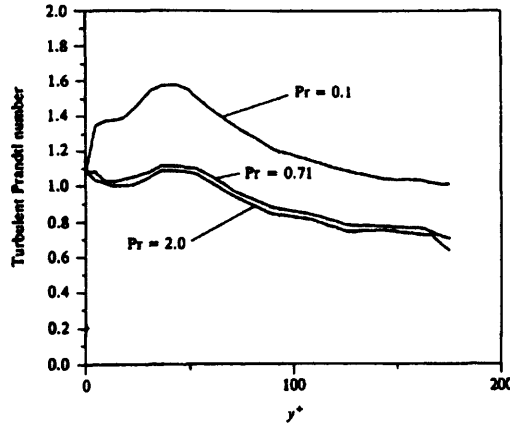


Figure-34. Calculated turbulent Prandtl number for a boundary layer in a fully developed flow in a flat duct [95]. y^* is the viscous sublayer thickness at the near-wall region.

Kays and Crawford proposed a correlation to estimate the value of Pr_t :

$$Pr_t = \frac{1}{\frac{1}{2 Pr_{t_\infty}} + C Pe_t \sqrt{\frac{1}{2 Pr_{t_\infty}} - (C Pe_t)^2} \left[1 - \exp\left(-\frac{1}{C Pe_t \sqrt{Pr_{t_\infty}}}\right) \right]} \quad (50)$$

where

$$Pe_t = Pr \frac{\varepsilon_M}{\nu} \quad (51)$$

Pe_t is the turbulent Peclet number, ε_M is the eddy diffusivity of momentum, Pr_{t_∞} is the value of Pr_t far from the wall, and C is a constant. Pr_{t_∞} and C are suggested to be 0.85 and 0.3 respectively [95, 96]. A plot of equation (50) for three different Prandtl number's is presented in figure 35.

Weigand et al. [97] propose a modification of Pr_{t_∞} in equation (50). Pr_{t_∞} is then not fixed to a constant value of 0.85 but expressed as follows:

$$Pr_{t_\infty} = 0.85 + \frac{D}{Pr Re^{0.888}} \quad (52)$$

where Re is the Reynolds number and D is a constant suggested to be 100.

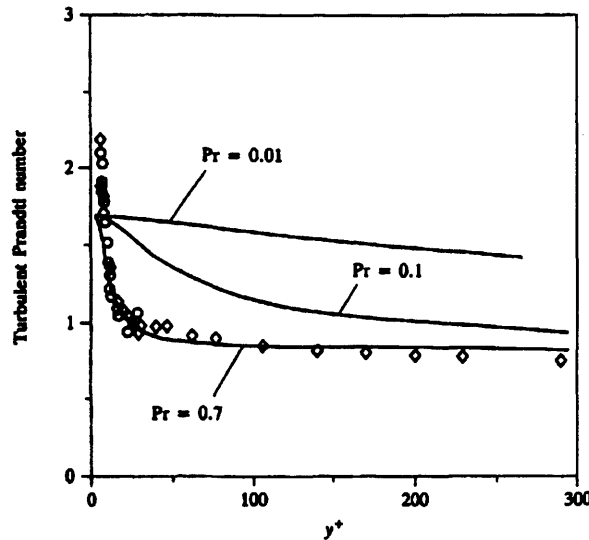


Figure-35. A plot of equation (50) Schematic diagram of the two dimensional control volume domain of the gas stirred ladle system [95]. y^* is the viscous sublayer thickness at the near-wall region.

Fluent can only accept a constant value for the turbulent Prandtl number. Therefore, equation (50) cannot be implemented in this present model. Fluent uses a default value of 0.85 which is widely accepted. However, further discussion to evaluate the optimum Pr_t constant value for this present analysis is described in section 4.1.1.

3.2 Boundary conditions

A diagram of the two-dimensional domain mesh is shown in figure 33 (page 48). The area (*h-e-d-i*) is occupied by slag phase of thickness 9 cm at the start of calculation. The free vacuum zone (*h-g-f-e*) on the top of the slag layer is occupied by gas under vacuum. The surface (*a-g*) stands for the system symmetrical plane. A homogenous temperature of value 1873 K was assumed at the start of calculation; this is the same value as used by Jonsson et al. [2]. The applied boundary conditions are described in the following sections.

3.2.1 Gas inlet nozzle:

Argon gas is injected into the domain volume by a nozzle located in the centre of the ladle bottom (position *a-b*) with a volume flow rate of 80l/min; again this is the same value used by Jonsson et al. [2]. The turbulence intensity is defined as the ratio of the

root-mean-square of the velocity fluctuations to the mean flow velocity. Fluent suggested that the turbulence intensity is ‘low’ if it is of order of 1% or less, and ‘high’ if it is of order of 10% or more. For internal flows, the turbulence intensity at the inlet is dependent on the history of the flow. If the flow is under-developed and undisturbed, then low turbulence intensity can be used. If the flow is fully developed, then the turbulence intensity at the core of a fully developed duct flow can be estimated from the following formula given in Fluent 6.2 documentations derived from an empirical correlation for pipe flows:

$$I = 0.16 \cdot (\text{Re})^{-0.125} \quad (53)$$

where I is turbulent intensity and (Re) is Reynolds number.

The turbulence intensity at the nozzle inlet for the ladle degassing system is required. As discussed in section 2.1.1, the fully developed region of the two-phase system within the control volume is independent of the gas injection device. Also the influence of the gas injection device used (nozzle/porous plug) and the gas input kinetic energy is limited to the local area near the inlet, and the gas velocity is drastically reduced within a short distance from the inlet due to the losses of the gas kinetic energy. For simplicity, equation (53) was used to calculate the initial turbulence intensity at the inlet. It was found to be (0.02%). The turbulence intensity can therefore be defined as ‘low’. The system then does not show any sensitivity to the turbulence intensity value at the inlet. The gas temperature injected at room temperature is increasing rapidly while it goes through the nozzle before it hits the steel at the nozzle steel side, therefore, the inlet gas temperature can be assumed to be 1273 K [26].

3.2.2 Ladle side and bottom walls:

A non-slip condition was assumed with the Fluent enhanced wall treatment which was applied. This non-slip condition was used to account for the wall friction influence on the flow velocity profile near the wall and the general flow pattern. The cells attached to these walls and merged with the molten steel phase were loaded with a volumetric

source term as described in the energy conservation equation (44). This energy source term was used to describe the assumed constant heat loss rate in (W/m^3) from the molten steel to the refractory lining [2] as described in section 3.1.1.

3.2.3. Pressure outlet;

Fluent provides a number of outlet boundary conditions for different applications such as compressible/incompressible flows. The process was operated under vacuum pressure condition. Therefore, the pressure outlet boundary condition was selected to define the outlet surface and applied a vacuum pressure at the gas exhaust surface ($g-f$). Also, as recommended by Fluent, the use of a pressure outlet boundary condition, instead of an outflow condition, not only provides an easy route for the application of the operational vacuum pressure, but also results in a better solution convergence. However, gas backflow is expected due to gas circulation in the free vacuum zone shown at the top in figure 33.

3.3 Interactions between two fluids

3.3.1 Drag coefficient models

The drag coefficient model is required to specify the drag function used in the calculation of the momentum exchange coefficients describing the interactions between the different phases.

Fluent provides different drag coefficient correlations to specify the interaction between two fluid phases. Kuo and Wallis [98] investigate bubbles rising in water (clean and tap water). The corresponding drag coefficient of the bubble behavior in various regions with rising speed is illustrated in figure 36

Jonsson et al. [2] (as discussed in section 2.4) and [26, 51, 89] used the Kuo and Wallis [98] drag coefficient correlations in regions 2, 2B, 4, and 5, as shown in figure 36, to specify the interaction between the three phases (steel/slag/gas). Detailed descriptions of selected drag coefficient correlations are given below.

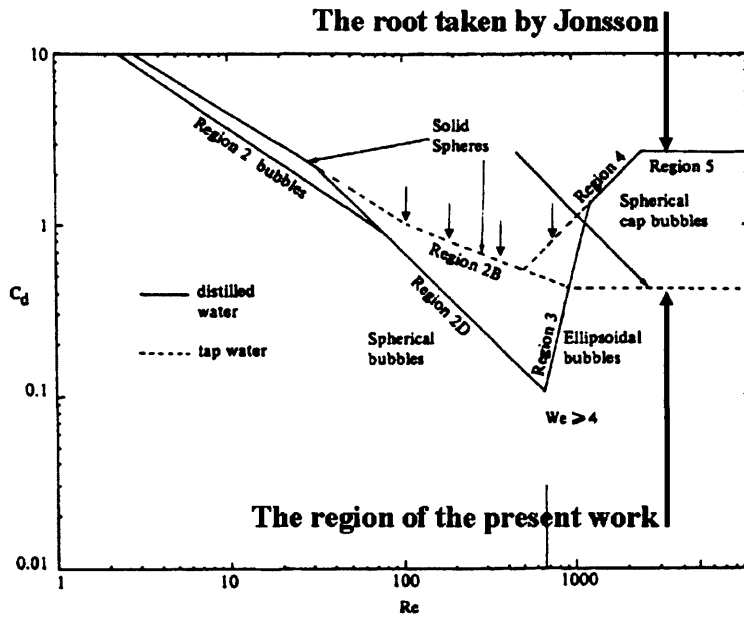


Figure-36. Drag coefficient for various regions with air bubbles rising in water[98] .

These correlations were selected because they have been used in ladle gas stirred systems. Fluent provides three drag coefficient models:- “Schiller and Naumann“; “Morsi and Alexander“; and “Symmetric” models, which are used to specify the drag function between two fluid phases. “Schiller and Naumann” [99] is the default model in Fluent, where the drag coefficient (C_d) is expressed in the following correlations.

$$C_d = \frac{24(1 + 0.15 \cdot Re^{0.687})}{Re} \quad \text{for } (Re \leq 1000) \quad (54)$$

and,

$$C_d = 0.44 \quad \text{for } (Re > 1000) \quad (55)$$

where Re is the Reynolds number.

Fluent recommends the Morsi and Alexander model as the most complete. The Morsi and Alexander [100] model adjusts the drag coefficient over a large range of Reynolds numbers as illustrated in the following correlations.

$C_d = 24.0/Re$	for	$Re < 0.1$	
$C_d = 22.73/Re + 0.0903/Re^2 + 3.69$	for	$0.1 < Re < 1.0$	
$C_d = 29.1667/Re - 3.8889/Re^2 + 1.222$	for	$1.0 < Re < 10.0$	
$C_d = 46.5/Re - 116.67/Re^2 + 0.6167$	for	$10.0 < Re < 100.0$	(56)
$C_d = 98.33/Re - 2778/Re^2 + 0.3644$	for	$100.0 < Re < 1000.0$	
$C_d = 148.62/Re - 4.75 \times 10^4/Re^2 + 0.357$	for	$1000.0 < Re < 5000.0$	
$C_d = -490.546/Re + 57.87 \times 10^4/Re^2 + 0.46$	for	$5000.0 < Re < 10000.0$	
$C_d = -1662.5/Re + 5.4167 \times 10^6/Re^2 + 0.5191$	for	$10000.0 < Re < 50000.0$	

where Re is the Reynolds number.

The symmetric model is recommended for flows in which the secondary phase is continuous in a region of the domain, just like the top slag layer, where the slag is a continuous secondary phase.

In addition, more drag coefficient correlations are published in the literature used for steelmaking process simulation. Xia et al. [94], suggests the following modified drag coefficient correlation for a ladle gas-stirred melt system:

$$C_d = \frac{2\sqrt{3}}{9} E_o^{1/2} \quad (57)$$

where, E_o is the Eotvos number defined as follows:

$$E_o = \frac{g(\rho_l - \rho_g)d_b^2}{\sigma} \quad (58)$$

where, ρ_l and ρ_g are the liquid and the gas phase densities respectively. Also, d_b is the gas bubble diameter in meters, and σ is the liquid phase surface tension.

Kuo and Wallis [98] suggested correlations for different ranges (regions 2, 2B, 4, and 5 in figure 36) of Reynolds and Weber number to determine the drag coefficient for the interaction between the gas bubbles and the liquid phase in a two-phase flow system as follows:

$$\begin{aligned}
C_d &= \frac{16}{Re} & Re \leq 0.49 \\
C_d &= \frac{20.68}{Re^{0.643}} & 0.49 \leq Re \leq 100 \\
C_d &= \frac{6.3}{Re^{0.385}} & Re \geq 100, \text{ AND } We \leq 8, \text{ AND } Re \leq \frac{2065.1}{We^{2.6}} \\
C_d &= \frac{We}{3} & Re \geq 100, \text{ AND } We \leq 8, \text{ AND } Re \geq \frac{2065.1}{We^{2.6}} \\
C_d &= \frac{8}{3} & Re \geq 100, \text{ AND } We \geq 8
\end{aligned} \tag{59}$$

where, Re and We are Reynolds and Weber numbers respectively.

In the Turkoglu and Farouk [4] mathematical model of the gas injected iron bath system, the drag coefficient in the bubbly flow regions was calculated after Clift et al. [101] proposal correlation.

$$C_D = \frac{24(1 + 0.15 \cdot Re_b^{0.687})}{Re_b} + \frac{0.42}{1 + \frac{4.25 \times 10^4}{Re_b^{1.16}}} \tag{60}$$

where Re_b is the Reynolds number based on the bubble diameter, the local continuous phase properties, and slip velocity.

In this present work, the Morsi and Alexander model is used to define the interaction between the molten steel phase (primary phase) and the gas phase (secondary phase). It is also used to define the interaction between the two secondary phases (molten slag and gas) due to the high stability compared with other models provided by Fluent. However, the symmetric model was used to define the interaction between the molten steel phase (primary phase) and the molten slag phase (secondary phase). Other models suggested in the literature have been compared with the Fluent built-in models and are discussed below in section 3.3.2.

3.3.2 Identification of the most appropriate drag coefficient and bubble size models

The drag coefficient models provided by Fluent and implemented in the gas stirred ladle system simulation were described in section 3.3.1. In this section the available drag coefficients model are evaluated to decide on which is to be used in this present work.

Figure 37 illustrates the estimated drag coefficient value using the available models plotted against Reynolds number. From inspection, the correlation suggested by Xia et al. [94] was excluded because it provides a constant value independent of the variation of the Reynolds number for the drag coefficient. This is not consistent with the estimated drag coefficient for air bubbles rising in water given in figure 36.

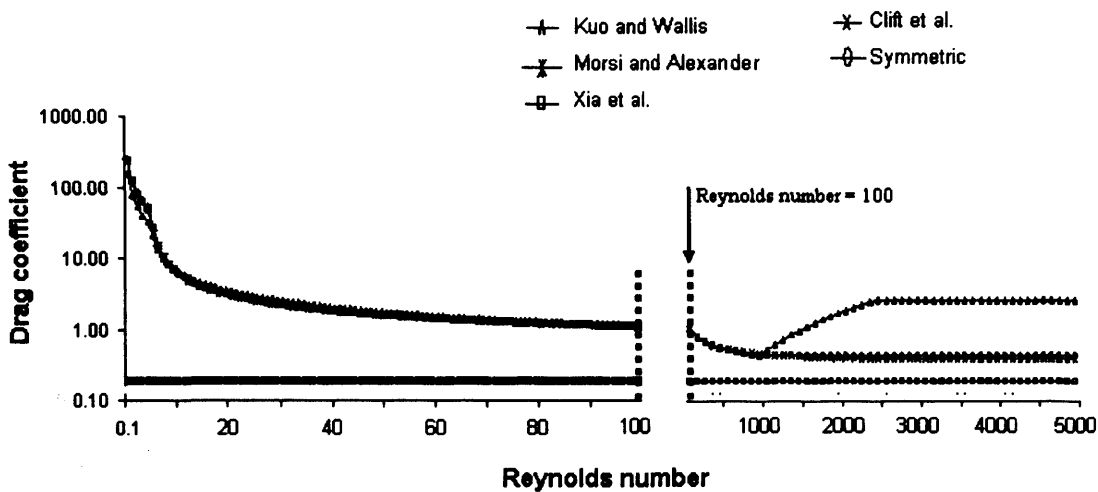


Figure-37. The estimation of the drag coefficient using a various correlations. A constant bubble size of 10mm was used in this calculation.

A significant divergence in the estimated drag coefficient value using the correlation proposed by Kuo and Wallis [98] starts at about ($Re=1000$). This sudden increase in follows the variation shown for regions 2, 2B, 4, and 5 in figure 36. In regions 4 and 5 in figure 36, the bubble shape is a spherical cap. As discussed in section 2.1.1 a spherical gas bubble shape was assumed in this present work. Therefore, the Kuo and Wallis [98] correlations for regions 4 and 5 in figure 36 are not consistent with the assumption of the spherical bubble shape. Furthermore, the correlation used to estimate the gas bubble size is applicable for a spherical bubble shape. However, the estimated drag coefficient value as per Kuo and Wallis [98] (as shown in figure 36)

for the spherical shape bubble is equivalent to the Morsi and Alexander [100] estimation and others shown in the figure. Therefore, Morsi and Alexander [100] correlation was selected as recommended by Fluent as the most complete model to be used in this present work to define the drag coefficient between the molten steel and the gas phase. The symmetry correlation recommended by Fluent was employed to define the interaction between the steel and the slag phase.

The gas bubble size estimation models based on drag coefficient discussed in section 2.1.2 were excluded (i.e. those due to Oeters [14] and Turkdogan [15]). This is due to the fact that the bubble size estimation is related to drag coefficient in these models but here we are aiming to calculate drag coefficient and hence an internal inconsistency develops. The model of Xie et al. [94] was excluded because the predicted bubble size is increasing with the path height and does not reduce once the steel/slag interface is reached, where bubble break up is expected (as discussed in section 2.1.1). The Mori et al. [12] empirical correlation to determine the bubble size immediately above the porous plugs was excluded because it predicted a relatively large bubble size which could not be resolved by the solver resulting in a solution collapsing. This correlation was implemented in parallel with Oeters [14] correlation [2, 26, 51, 82, 89] to predict the bubble size immediately above the nozzle and in the bulk respectively. Both correlations work smoothly with each other because Oeters correlation was predicting a relatively large bubble size. However, we have already excluded Oeters [14] correlation for reasons explained at the beginning of this paragraph. On the other hand Mori et al. [12] correlation didn't work successfully with Wang et al. [13] correlation due to the relatively smaller bubble size predicted by Wang et al. [13] in the region close to the nozzle which make a confliction resulting in a solution collapsing. In this present work, Wang et al. [13] correlation was selected to be used in the analysis.

3.4 Steel/slag physical and thermal properties

Table 9 illustrates the density and viscosity properties used for steel/slag/gas phases in the calculation. These are the same values as those used for Jonsson et al. [2] work.

Table-9. Steel/slag/gas material density and viscosity properties.

Phase	Density (kg/m ³)	Viscosity (kg/ms)
Steel	$\rho = 8.586 \times 10^3 - 0.8567 \cdot T^*$ [102]	$\mu = 0.3147 \times 10^{-3} \cdot \exp\left(\frac{46480}{8.3144 \cdot T}\right)$ [102]
Slag	$\rho = 2977.6 - 0.1536 \cdot T$ [89]	$\mu = 4.1909 \times 10^{-3} \cdot \exp\left(\frac{164022}{T}\right)$ [89]
Argon	1.6228 **	2.125×10^{-5} *

T is the temperature in (K). * Temperature range is (1812-1923 K). ** Data taken from Fluent materials database.

The slag thermal conductivity is in the range 0.5 to 1.2 W/mK [103]. Based on experimental data, the following correlation [103] can be used to estimate the slag thermal conductivity.

$$k = \frac{1.8 \times 10^{-5}}{V} \quad (61)$$

where

$$V = \frac{M}{\rho} \quad (62)$$

V and M are the molar volume and molar weight respectively. Using equation (61) with the slag system of concern in this study (55%CaO-30%Al₂O₃-7.5%SiO₂-7.5MgO) the thermal conductivity is (0.7689 W/mK) at 1600 °C.

The slag heat capacity is a combination of the individual component heat capacities as expressed in equations (63-67).

$$C_{p,CaO} = \frac{4.1868 \times 10^3}{56.079} \times \left(11.86 + 1.08 \times 10^{-3} T_s - \frac{1.66 \times 10^5}{T_s^2} \right) \quad (63)$$

$$C_{p,Al_2O_3} = \frac{4.1868 \times 10^3}{101.961} \times \left(28.804 + 2.197 \times 10^{-3} T_s - \frac{11.56 \times 10^5}{T_s^2} \right) \quad (64)$$

$$C_{p,SiO_2} = \frac{4.1868 \times 10^3}{60.084} \times \left(17.119 + 0.452 \times 10^{-3} T_s - \frac{9.335 \times 10^5}{T_s^2} \right) \quad (65)$$

$$C_{p,MgO} = \frac{4.1868 \times 10^3}{40.304} \times \left(11.707 + 0.751 \times 10^{-3} T_s - \frac{2.734 \times 10^5}{T_s^2} \right) \quad (66)$$

$$C_{p,slag} = (\%CaO)C_{p,CaS} + (\%Al_2O_3)C_{p,Al_2O_3} + (\%SiO_2)C_{p,SiO_2} + (\%MgO)C_{p,MgO} \quad (67)$$

where $C_{p,i}$ and T_s are the heat capacity and slag temperature respectively for the i th component. The present slag system (55%CaO-30%Al₂O₃-7.5%SiO₂-7.5MgO) heat capacity at 1873 K was calculated using equation (67). The variation in the heat capacity value over the working temperature range was neglected because Fluent can only accept a constant value for the heat capacity.

3.5 Basis for the use of the thermodynamic prediction package

In the steelmaking industry, the oxygen partial pressure within the steel/slag system is within the range of 10^{-8} - $10^{-9.2}$ atm. Therefore, the sulphur tends to be present as sulphide rather than sulphate (see section 2.2.1 (ii)). In addition, the aluminum present in the fully killed steel means that a reasonable assumption is that the desulphurization process is limited to the three main control elements (Al, O, and S) (see section 2.4) [2]. However, the influence of the presence of CaO on sulphur removal during the fully-killed steel refining process is illustrated in the overall desulphurization reaction expressed as [16]:

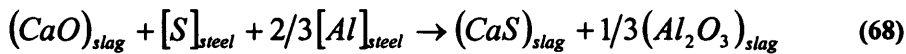


Figure 38 illustrates the influence of SiO₂ slag content on desulphurization. In addition, the notable influence of the initial content of FeO in the slag has been published in the literature [83].

The thermodynamic prediction of the desulphurization process is expected to be enhanced using the MTDATA package, due to its capability for making thermodynamic predictions for multi-component systems containing up to 30

elements. MTDATA is equipped with four different databases named NPLOX3, NPLOX_trace, TCFE, and SUB_SGTE. The database [NPLOX3] contains the data for the oxide system CaO-Al₂O₃-MgO-SiO₂-Fe-O, [NPLOX_trace] is used to trace the sulphur in the oxide phase, [TCFE] is the multi-component alloy database specific to steels containing the data about O/S solubility in steel, and finally, [SUB_SGTE] is the gas phase data source.

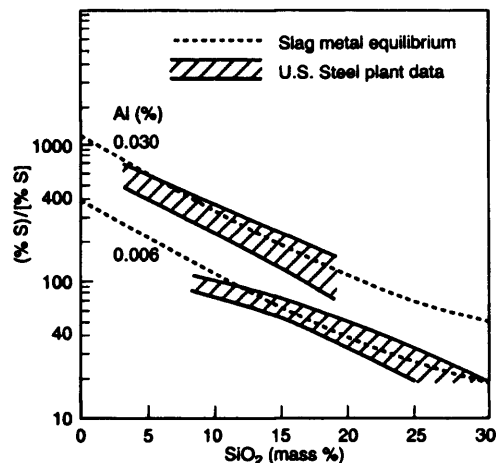


Figure-38. Slag/metal sulphur distribution ratio after desulphurisation with lime-saturated CaO-MgO-Al₂O₃-SiO₂ slags at 1600 +/- 15 °C [14].

3.6 Solution method strategy

A pre-defined CFD file was built and solved until the injected gas penetrates the top slag layer and a free slag hole is created which is called the ‘open-eye’ as illustrated in figure 39. This is taken as the start point for the coupling analysis (i.e. the iterative linking of the CFD program with the thermodynamic prediction package MTDATA) due to the stability of the system after the complete development of the two-phase plume and creation of the open eye. Also, there is high uncertainty about the required time for the gas phase to reach the top surface. This time is very sensitive to the numerical solution parameters used e.g. “time step” and also the grid used. In addition, before the development of the open eye, the steel circulation at the steel/slag interface is expected to be minimal.

A pre-defined thermodynamics file was created. The multiphase thermal system components are defined as (CaO-SiO₂-MgO-Al-Fe-O-S). In MTDATA the chemical

system can be defined either by its components like (CaO- Al₂O₃-SiO₂-MgO) or by its elements like (Ca-Al-Si-Mg-O), or a mix of both. In this present steel/slag system, aluminium dissolved in the molten steel is being lost at the steel/slag interface during the refining process. Therefore, to allow easier tracing of the aluminium element at the steel/slag interface, the alumina component of the slag system was defined by its elements. The aluminium element mass defined in the system is a combination of the aluminium forming the alumina from slag phase and the dissolved aluminium in the molten steel.

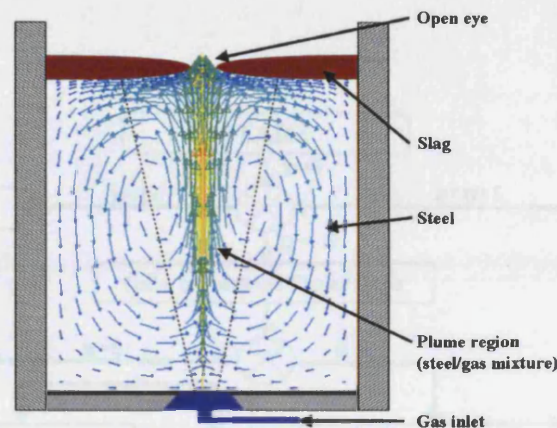
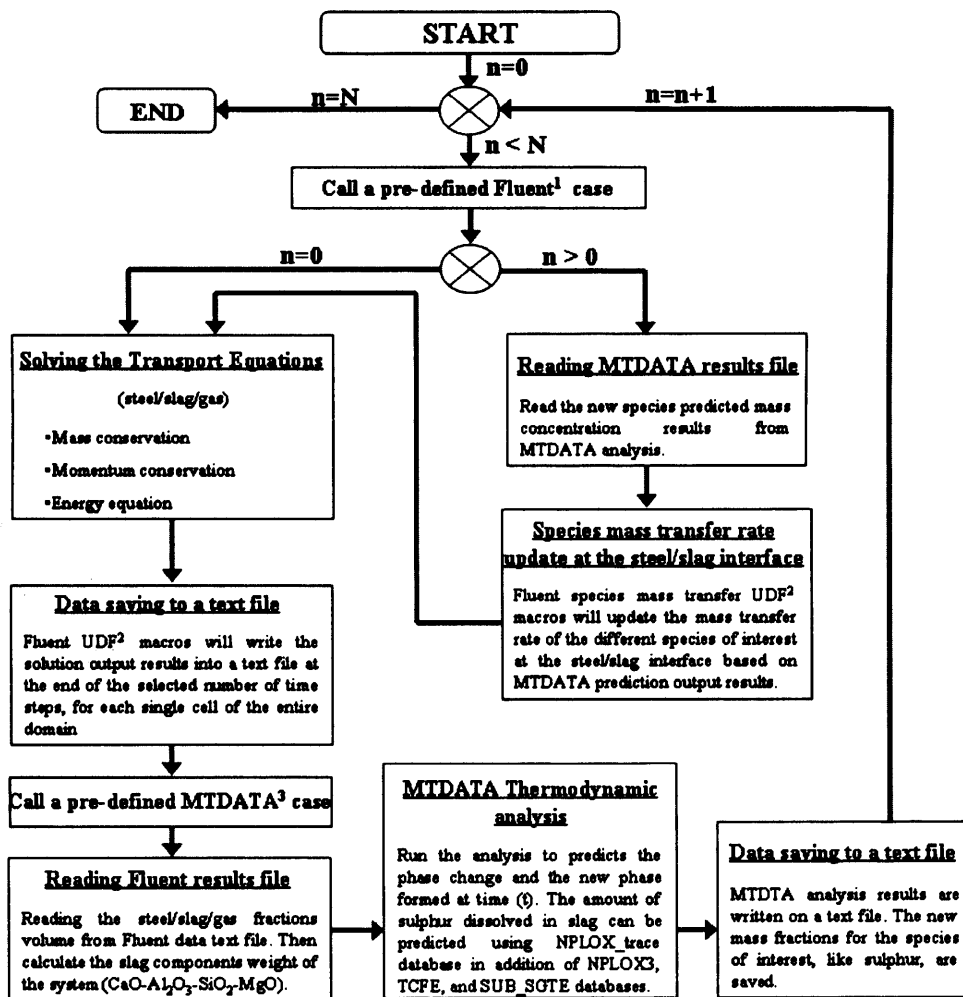


Figure-39. A schematic diagram showing the plume region and the open eye created at the top slag layer

A data exchange control macro was created using the Visual Basic 6.0 environment. Figure 40 illustrates the coupling flow chart. First, Fluent is executed to run the pre-defined file for a defined Δt time step. Then the volume fractions of the different phases in the mixture, temperature, and pressure values for each single cell are stored in a defined text file. Next, the macrocode reads the CFD results text file, and in each cell with steel/slag mixture, the molar weights of the multiphase thermodynamic system components are calculated from the steel/slag volume fractions. MTDATA is only executed for each cell that contains sufficient steel/slag mixture at the steel/slag interface (as opposed to the cells which contain steel or slag alone) as illustrated in figure 41. "Sufficient" mean that the steel/slag mass mixture fractions should satisfy the required conditions to call MTDATA for analysis. These conditions are:- (1) the steel and/or slag volume fraction should not be less than 5×10^{-2} of the cell volume, (Fluent predicts incorrectly a tiny amount of these phases is present in some cells due

to the numerical errors. This error cannot be avoided and does not influence the overall flow pattern); (2) the minimum mass values accepted by MTDATA are controlled to run the analysis with accepted accuracy. With reference to this second condition, the Gibbs energy minimisation algorithm used in MTDATA provides a very stable computation with high accuracy prediction, but does not allow the calculation of very small amounts of species down to six decimal places in composition. The MTDATA thermodynamic analysis was run for different steel/slag mass mixtures to define the criteria values. The minimum masses of steel and/or slag accepted to run the thermodynamic analysis properly are (0.001kg) and (0.0001kg) respectively.



1. Computational fluid dynamics package.
2. Fluent User Defined Function to customise the model.
3. Thermodynamic package from National Physical Laboratory (NPL).

Figure-40. Flow chart diagram of the coupling strategy method used to link Fluent CFD analysis with MTDATA thermodynamics package.

The selected values can be justified because of the large mass scale of the simulated system (100 tonne ladle). In addition, these minimum masses make the MTDATA computational analysis work very smoothly and with high accuracy.

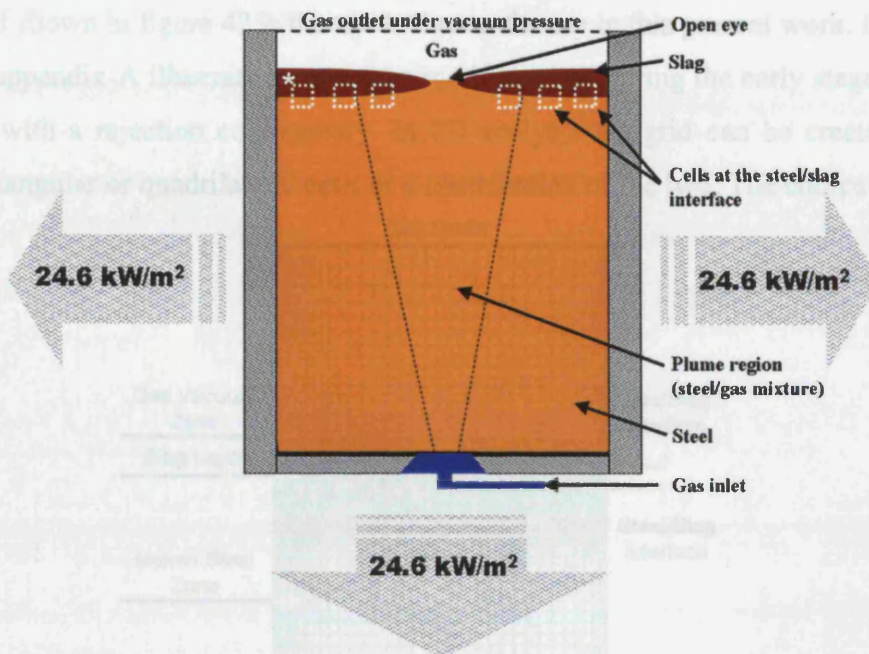


Figure-41. Sketch of the gas stirred ladle system. In each cell at the steel/slag interface, the mass mixture fraction is calculated. The steel/slag thermodynamic analysis is only solved for the cells which meet the mass mixture criteria (see section 3.6).

The thermodynamic results are stored in a text file. This first step is repeated until the end of the refining process. However, starting from the second step, at the beginning of the Fluent session, the species mass concentration at the steel/slag interface is updated by reading the MTDATA results text file from the previous time step, using the customised species mass transfer Fluent user define function (UDF). The predicted data is used by Fluent to calculate species mass transfer rate of elements of interest (Al, O, and S) at the interface. This mass transfer rate is updated to absorb the variation in chemistry and mixture mass fraction at the steel/slag interface. The time Δt determines how often Fluent interfaces with MTDATA. This is referred to later as the “interface rate”.

3.7 Mathematical model development stages

3.7.1 Grid development

The grid shown in figure 42 is the mesh chosen for use in this present work. Figures 1 to 8 in appendix-A illustrate some of the meshes tested during the early stages of this project with a rejection commentary. In 2D analysis the grid can be created either using triangular or quadrilateral cells or a combination of the two. The choice of

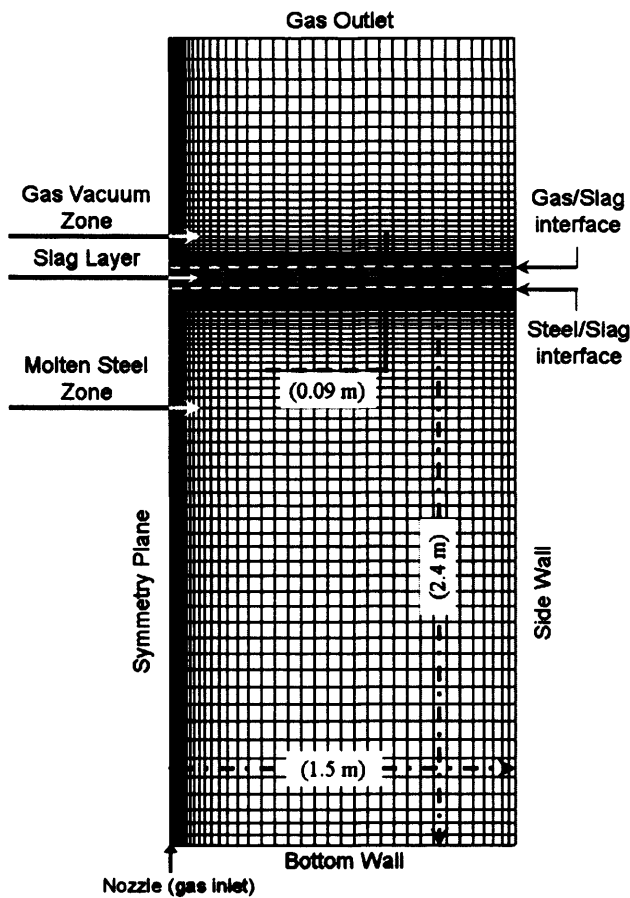


Figure-42. Quadrilateral cells grid. The grid used in this present analysis.

which mesh type to use depends on the application. In this present work, the slag phase is floating on the top of the molten steel primary phase, and also an extra gas phase is present on the top of the slag layer. Therefore, the grid cells at the interface zones between these three phases need to be carefully selected. They should be small enough to resolve reasonably the mixing phenomena occurring but the overall number of cells should be controlled to reduce the computational running time. The number of

cells covering the mixing zone at the steel/slag interface needs to be controlled to reduce the overall thermodynamic analysis computational running time; the number of times the thermodynamics package (MTDATA) is called equals the number of cells at the interface with a sufficient steel/slag mixture (for a definition of 'sufficient steel/slag mixture' see section 3.6).

It has been found that the use of a quadrilateral mesh in this application gives a better solution with far fewer cells than using a triangular mesh. The final chosen mesh consisted of (3744) quadrilateral cells as shown in the figure. The zones of concern in this system are reasonably refined, i.e. the steel/slag interface, gas/slag interface, gas/steel-mixing zone, and near the wall zones.

The creation process of this simulation model was to start simply with a two-phase water /air model. Water is used in the physical/numerical simulation of molten steel process due its equivalent kinematic viscosity [1, 18, 86, 88, 104-107]. In advancing this model from a two-phase water/air model into a multi-phase-species (steel/slag/gas + S/O/Al) model, many mesh grids were used. The grid that was suitable for a certain stage was not qualified for another. Figure (9) in appendix-A shows a grid that was suitable for the three-phase thermal analysis. The cells with high aspect ratio (length/width) in the slag phase caused a spurious rapid increase in the molten slag flow velocity, at variance with published results for a similar application [2, 26, 51], when the species formulation was added into the system. This is illustrated in figure 43.

Additional work was carried out to modify the final chosen grid to reduce the number of cells at the steel/slag interface and hence the overall thermodynamic analysis computational running time. However, at the time of issuing this thesis no mesh with fewer cells at the interface had been successfully created. Fortunately, this running grid was working very smoothly with the complexity of the present mathematical model. Other grids with fewer cells could not resolve the interaction between phases with high-density ratio at the slag/gas interface. In contrast with the Jonsson et al. [2] model grid (which has 1036 cells and one interface), the present model grid involves two interface zones namely, steel/slag and gas/slag interface zones. This results in an increase in the total cell number in the grid.

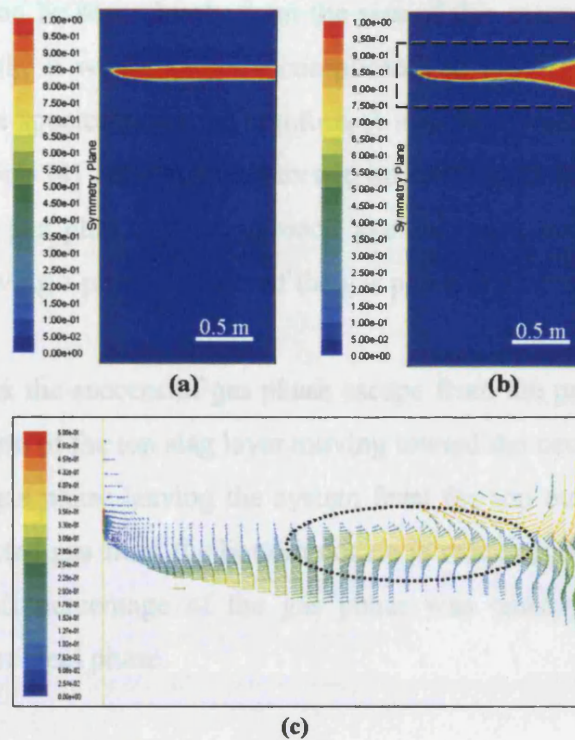


Figure-43. (a) Slag phase volume fraction after 40 sec., (b) Slag phase volume fraction after 45 sec., (c) Velocity magnitude vector (m/s) of slag phase (see dashed line in (b)) after 45 sec - the highlighted area shows the unrealistic growth of slag velocity.

3.7.2 Gas escape mechanism

The use of a top wall/symmetrical surface with a gas escape allowance is very popular to simulate the free surface in ladle stirred gas system [2, 17, 26, 51, 86, 89, 107-109]. Therefore, it was an obvious approach to start with in this present project. A simple source code allowing the gas phase escape was linked to the top wall surface.

However, the source code was insufficient to allow a proper escape of the gas phase in a two-phase system without influencing the flow pattern below the escape surface.

It was found that less than 30% of the gas left the system and the rest was recirculated as illustrated in figure 44, resulting in a collapse of the numerical solution before the injected gas phase reached the steel/slag interface zone.

A highly complex macro was then located in the Fluent UDF library. This macro links with Fluent 6.0 to define the free liquid surface boundary condition for a degassing

system. This macro was tested with the water/air two-phase system. The high complexity level can be seen clearly from the size of this macro; it is about twenty-text pages in length. It would be very complicated to modify it to work with the present multi-phase-species system. Therefore, it was more convenient to follow the Turkoglu and Farouk [4] approach and to add an extra zone on the top of the slag layer occupied by gas phase. This approach avoided the complexity of creating a source macro, allowing a proper escape of the gas phase from the top slag surface.

Figure 45 illustrates the successful gas phase escape from the primary phase (molten steel) and penetration of the top slag layer moving toward the occupied gas zone at the top, and then the gas phase leaving the system from the top outlet. In this approach almost all the injected gas from the bottom nozzle is reaching the steel/slag interface zone. Only a small percentage of the gas phase was entrapped by the slag and recirculated with the steel phase.

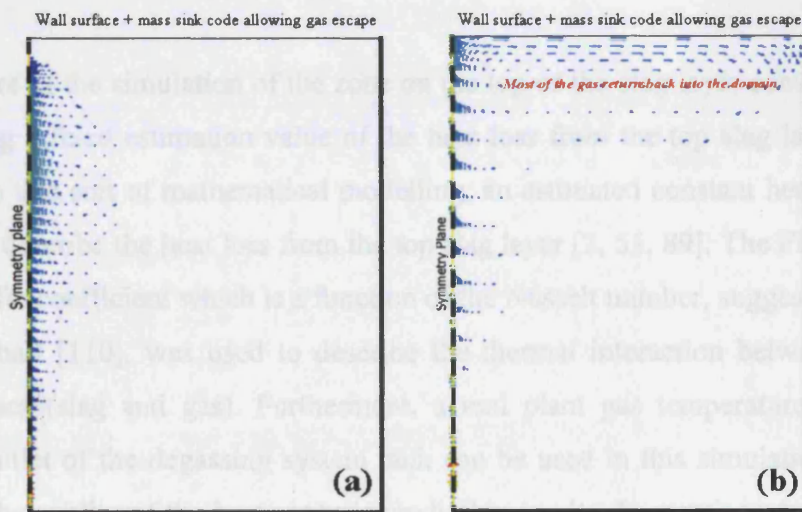


Figure-44. Gas phase velocity vectors (a) illustrating the plume region formed for the two-phase steel/gas system (slag phase not accounted for) before the gas phase reaches the top wall surface. (b) illustrating the improper circulation of the gas phase inside the control volume. The gas phase should leave the system from the top wall surface.

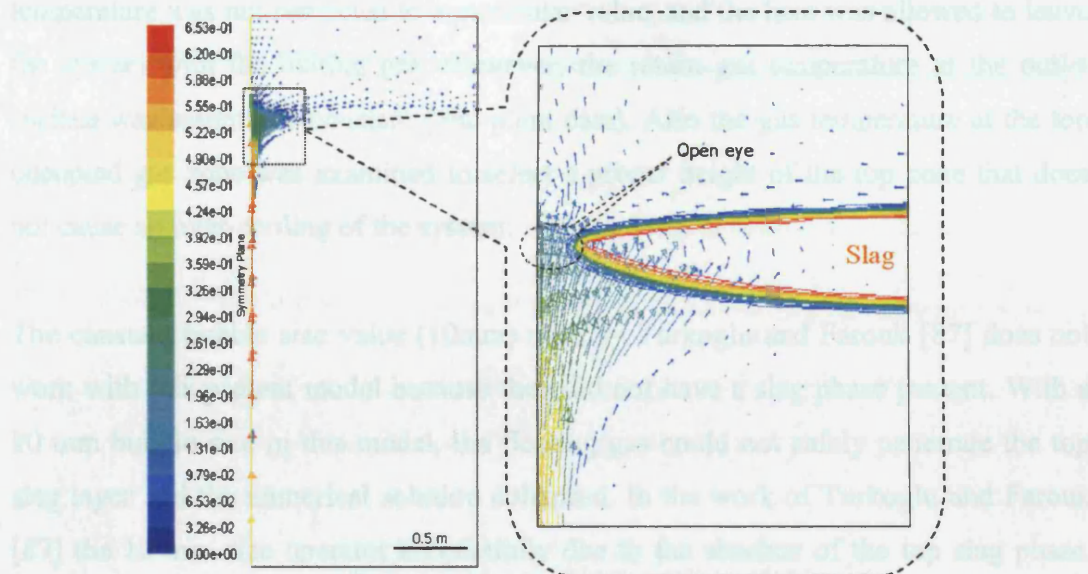


Figure-45. Showing the gas phase velocity magnitude vectors (m/s). The gas penetration of the slag layer with a top occupied gas zone is shown on the left. The formation of the open eye is shown on the right.

3.7.3 Thermal interaction between phases and gas bubble size influence

One feature of the simulation of the zone on the top of the slag layer occupied by gas is avoiding a fixed estimation value of the heat loss from the top slag layer surface. Usually in this sort of mathematical modelling, an estimated constant heat loss value is used to describe the heat loss from the top slag layer [2, 51, 89]. The Fluent default heat transfer coefficient which is a function of the Nusselt number, suggested by Ranz and Marshall [110], was used to describe the thermal interaction between the two fluid phases (slag and gas). Furthermore, a real plant gas temperature at the gas exhaust outlet of the degassing system tank can be used in this simulation model to improve the quality of the heat analysis prediction results. In practice when real plant data for the gas exhaust temperature was used in this simulation model, a huge reduction of the molten steel phase temperature near the top zone was predicted as illustrated in figure 46. The outlet surface is then working as a heat sink resulting in over-cooling of the system due to the underestimated fixed outlet temperature. This could be due to incorrect use of the low exhaust temperature very close to the path surface. This means that the temperature at the model outlet surface is expected to be higher than the given temperature. Therefore, this temperature value should not be used at this present outlet surface. In the results presented in section 4.1.2 the outlet

temperature was not restricted to a particular value, and the heat was allowed to leave the system with the exiting gas. However, the return gas temperature at the outlet surface was assumed a constant (real plant data). Also the gas temperature at the top occupied gas zone was examined to select a proper height of the top zone that does not cause an over-cooling of the system.

The constant bubble size value (10mm) used by Turkoglu and Farouk [87] does not work with this present model because they did not have a slag phase present. With a 10 mm bubble size in this model, the floating gas could not safely penetrate the top slag layer and the numerical solution collapsed. In the work of Turkoglu and Farouk [87] the 10 mm size operates successfully due to the absence of the top slag phase. With a smaller constant gas bubble size (2.5mm) the gas phase successfully penetrated through the top slag layer but with still a disturbance in the shape of the slag layer tip shape (figure 47 left hand diagram). With a smaller bubble size (1mm) still the shape is smooth (figure 47 right hand diagram).

The return gas temperature is set to 1373 K after a real plant estimation. A gas circulation is occurring in the occupied gas zone at the top. This return gas results in over cooling of the system.

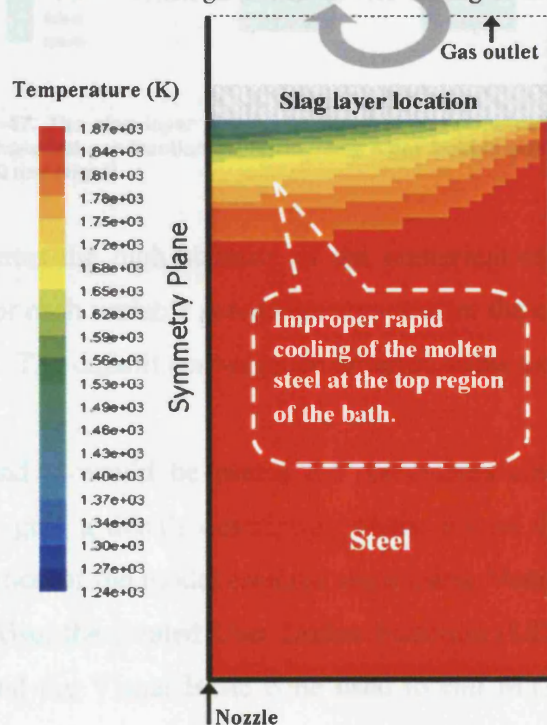


Figure-46. Molten steel phase temperature (K) distribution.

At this stage of the project the general flow pattern and the predicted mixing zone at the steel/slag interface using a model with a constant small value of the injected gas bubble size can be reasonably accepted for the following reasons:- firstly, as discussed in section 2.1.3, the mixing at the steel/slag interface is significantly influenced by the gas volume flow rate and not by the gas bubble size; secondly, the illustration of the gas bubble size influence shown in figure 47 is limited to the open-eye zone and not the entire slag layer as shown in the figure. Note that in this work the refining process for gases such as hydrogen and nitrogen which depends on the predicted gas bubble size, as discussed in sections 2.1.3 and 2.3, is not accounted for.

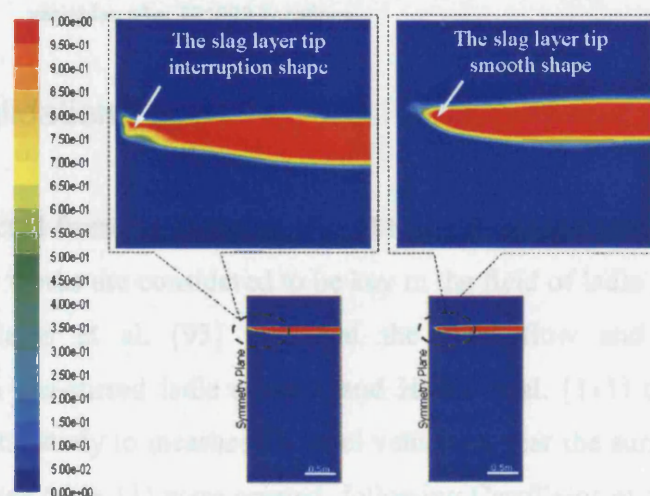


Figure-47. The slag layer shape shortly after gas penetration occurs. The slag phase volume fraction is shown using a gas bubble size of 2.5 mm (left) and 1.0 mm (right)

Figure 48 illustrates the high stability of the numerical solution. In this figure the residual values for each variable solved are shown after the creation of the open eye in the top slag layer. The default convergence criterion value used by Fluent is 10^{-3} . A

The authors found it would be useful for researchers continue working with this present work, to give a details description of the model development using Fluent package. Description of the model creation steps using Fluent CFD package are given in appendix-B. Also, the created User Define Function (UDF) library written in “C” language code and the Visual Basic code used to call MTDATA are printed to the attached CD.

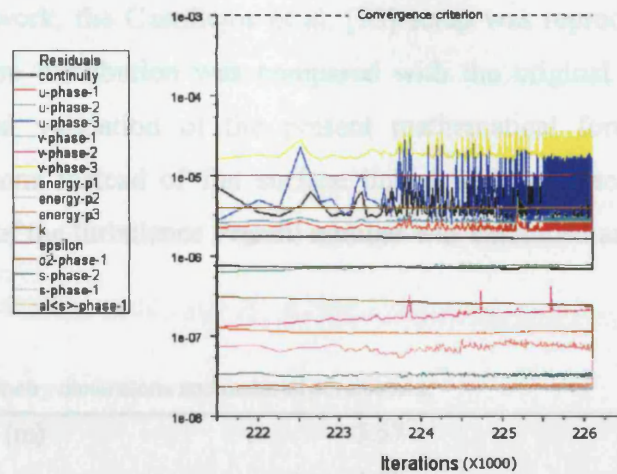


Figure-48. Residual values of the mathematical model simulation variables after 221500 iterations.

3.8 Model validation.

Two works selected from the literature [93, 111] are described below in section 3.8.1 and 3.8.2. These works are considered to be key in the field of ladle gas stirred system analysis. Castillejos et al. [93] modelled the fluid flow and the temperature distribution in a gas-stirred ladle system, and Hsiao et al. [111] conducted a plant scale experimental study to measure the steel velocities near the surface. Two models (cases 1 and 2, see table 11) were created, following Castillejos et al. [93] and Hsiao et al. [111], in the present work for purposes of validation. The results will be shown in section 4.1.1.

3.8.1 Thermal validation of the present mathematical formulation.

Castillejos et al. [93] studied fluid flow and the temperature distribution in a gas-stirred ladle system of 250 tonnes. The gas was injected using a nozzle located at the centre of the ladle bottom. Ladle geometry dimensions and important mathematical model parameters are listed in table 10. Initially, a linear distribution of the liquid steel temperature from the bottom to the top of the steel bath with a 40 °C temperature difference was assumed, and a uniform distribution in the radial direction. Furthermore, a constant heat loss value of 1.25×10^4 W/m² through the ladle wall was assumed. The authors reported a complete temperature homogenisation achievement after approximately 180 seconds.

In the present work, the Castillejos et al. [93] setup was reproduced. The predicted steel temperature distribution was compared with the original published results to make a thermal validation of the present mathematical formulation (e.g. extra occupied gas zone instead of flat surface linked with gas escape macro). Also, a different value of the turbulence Prandtl number was examined as discussed in section (3.1.2).

Table-10 Ladle geometry dimensions and material parameters.

liquid path depth (m)	3.57
vessel radius (m)	1.79
nozzle diameter (m)	0.013
gas flow rate (m ³ /s)	7.96×10^{-3}
T stratification (K)	40 (1813 to 1853)
ρ_l (kg/m ³)	7500
ρ_g (kg/m ³)	0.933
μ_l (kg/ms)	6.2×10^{-3}
k_l (W/mK)	41
C_{pl} (J/kgK)	755
C_{pg} (J/kgK)	520

3.8.2 Fluid dynamic validation of the present mathematical formulation.

Hsiao et al. [111] conducted a plant scale trial to study the fluid flow in a 60 tonne gas stirred ladle. A direct measurement of the steel velocities near the surface was taken during the experimental work. Various gas flow rates were applied during the experimental work over the range of [0.025 – 0.465 Nm³/min]. The measurement was taken using a gauge system capable of working in a molten steel environment, developed at MEFOS in Sweden in collaboration with the University of Luleå.

The ladle height and diameter are 2.88 m and 2.44 m respectively. However the bath height (i.e. the depth of the molten steel) was only 1.35 m, and the gas was injected through a central porous plug located at the bottom of the ladle. The slag layer was removed prior trials. To mimic the Hsiao et al. experimental work, a two phase model was set up (without the slag layer) with identical physical parameters.

4. Results

Fundamental background about the fluid dynamics phenomena associated with the secondary steelmaking process was discussed in chapter 2, along with the role of slag in the steelmaking process, slag thermo-physical properties and the influence of slag on the overall flow pattern and refining process in the gas stirred system. The aim of this project is to make a coupling between the ladle degassing system CFD model and the thermodynamic model. A three phase (steel/gas/slag) mathematical model has been developed using the Fluent CFD package with MTDATA used to predict the species exchange at the metal/slag interface. The CFD mathematical formulation, boundary conditions, drag coefficient correlations, and the coupling strategy were described in chapter 3.

100 and 150 tonne ladle sizes with different gas injection configurations were investigated in this present work. The first ladle (100 tonne) comes with a single nozzle located at the centre of the bottom wall. This is directly comparable with the ladle in the Jonsson et al. [55]. work. The second ladle (150 tonne) has two off-centre nozzles and mimics that used in industry. To mimic Castillejos et al. [93] and Hsiao et al. [111] works, two phase models were set up (without the slag layer) with identical physical parameters as described in section 3.8. Several cases described in table 11 were investigated to validate and study different operating conditions and slag viscosity models.

In this chapter the results of the cases listed in table 11 are presented. The results are presented in two main categories; gas stirred system CFD results (section 4.1); and CFD linked to the thermodynamic model (section 4.2).

Case No	Ladle size (tonne)	Nozzle No	Nozzle position	Slag viscosity model	Gas flow rate (l/min) per Nozzle	Bubble size model	Two phase or Three phase	Comment
1	250	1	centre	Temperature correlation [*]	see table 10	10 mm [87]	2	• Mimic of Castillejos et al. [93].
2	60	1	centre	Temperature correlation [*]	50, 100	Wang et al. [13]	2	• Mimic of Hsiao et al. [111]. • Isothermal system. The system temperature set to 1873 K.
3	100	1	centre	Temperature correlation [*]	80	Wang et al. [13]	3	• Slag system 1.
4	100	1	centre	Temperature correlation [*]	400	Wang et al. [13]	3	• Slag system 1.
5	100	1	centre	NPL model	80	Wang et al. [13]	3	• Slag system 1.
6	100	1	centre	NPL model	400	Wang et al. [13]	3	• Slag system 1.
7	100	1	centre	NPL model	80	Wang et al. [13]	3	• Allowing Ca ⁺⁺ mobility and CaS precipitation in slag phase. • slag system 1.
8	150	2	off-centre	NPL model	200	Wang et al. [13]	3	• Slag system 2.

Table-11. The cases investigated in this present work.

- The slag viscosity given in table 9 [$\mu = 4.1909 \times 10^{-3} \cdot \exp(164022/T)$].
- Slag system 1 is (55 wt% CaO-30 wt% Al₂O₃-7.5 wt% SiO₂-7.5 wt% MgO), the initial wt% of (Al, O, and S) in steel are 0.052, 0.00044, and 0.031 respectively.
- Slag system 2 is (50.92 wt% CaO-29.37 wt% Al₂O₃-6.07 wt% SiO₂-10.3 wt% MgO), the initial wt% of (Al, O, and S) in steel are 0.06, 0.0777, and 0.012 respectively.
- The heat loss from the wall is set to 24600 W/m² except in cases 1 and 2. The heat loss from the wall in case 1 is set to 12500 W/m².

4.1 Gas stirred system, CFD results

A three phase Eulerian model was used to simulate the gas stirred ladle system. As a feature of this present work, an additional gas occupied zone was added on the top of the slag layer instead of the classical top wall linked with a gas escape code, as discussed in section 3.6.2. The model validation, the predicted flow pattern, gas bubble size, and the temperature distribution at the gas stirred ladle system are presented below in sections 4.1.1, 4.1.2, 4.1.3 and 4.1.4 respectively. Different cases have been used to explore different issues.

4.1.1 Model validation

i) Thermal validation

Case 1 mimics Castillejos et al. [93] and predicts a homogenous temperature of 1831.6 K. The homogenous temperature predicted by Castillejos et al. [93] was 1832.65 K.

The Castillejos et al. [93] set up was examined using three different values of the turbulent Prandtl number as selected within the estimated range suggested by equation (50) (see section 5.1.3 (ii)). Before showing the calculated results it should be noted that the initial steel temperature distribution used by Castillejos et al. [93] is given in figure 49 where the temperature varies with height in the bath with a 40 degree difference from the bottom to the top. The sketch given in figure 49 shows the eight selected points located near the wall and far into the steel bulk to evaluate the influence of the turbulent Prandtl number on the steel temperature variation over the entire domain during the process in case 1. Figures 50-52 present the steel temperature variation at the eight selected points over the domain during process time.

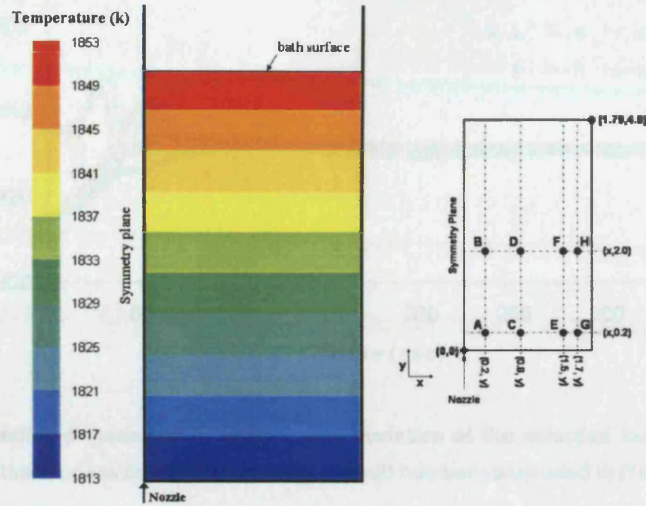


Figure-49. The initial molten steel temperature distribution assumed by Castillejos et al. [93] (left). A sketch show the eight selected points located near the wall and far in the steel bulk to evaluate the influence of the used turbulent Prandtl number on the steel temperature variation over the entire domain during the process (right).

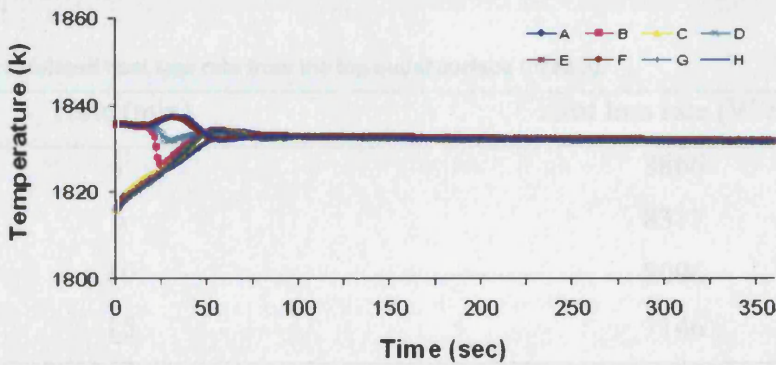


Figure-50. The predicted molten steel temperature variation at the selected locations described in figure (49) during the process time. The turbulent Prandtl number value used is (0.85).

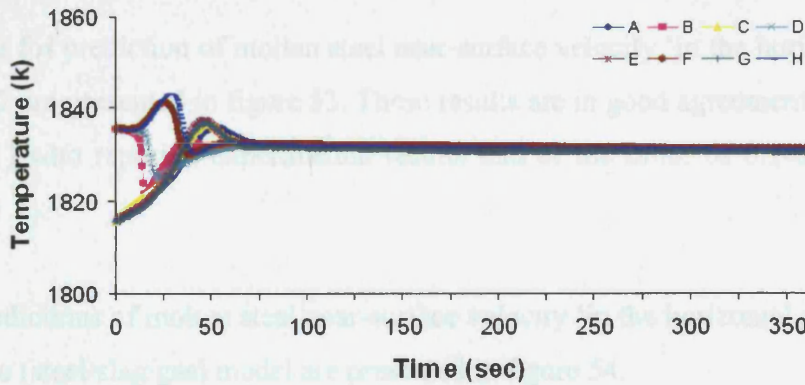


Figure-51. The predicted molten steel temperature variation at the selected locations described in figure (49) during the process time. The turbulent Prandtl number value used is (3.0).

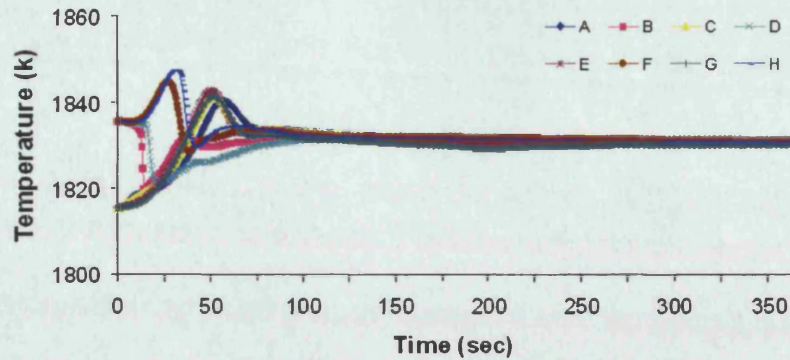


Figure-52. The predicted molten steel temperature variation at the selected locations described in figure (49) during the process time. The turbulent Prandtl number value used is (10.0).

These results will be further commented in section 5.1.3 (ii).

The predicted heat loss rate in case 3 at the outlet surface of the 100 tonne ladle applying 80 l/min during the refining process is given in table 12.

Table-12 The calculated heat loss rate from the top outlet surface (case 3).

Time (min)	Heat loss rate (W/m ²)
1	8866
5	8317
10	8096
15	7146

ii) Fluid flow validation

The results for prediction of molten steel near-surface velocity 'in the horizontal axis' with case 2 are presented in figure 53. These results are in good agreement with Hsiao et al. [111] who reported experimental results that of the order of 0.1-0.4 m/s (see section 5.1.1).

Case 3 predictions of molten steel near-surface velocity 'in the horizontal axis' for the three phase (steel/slag/gas) model are presented in figure 54.

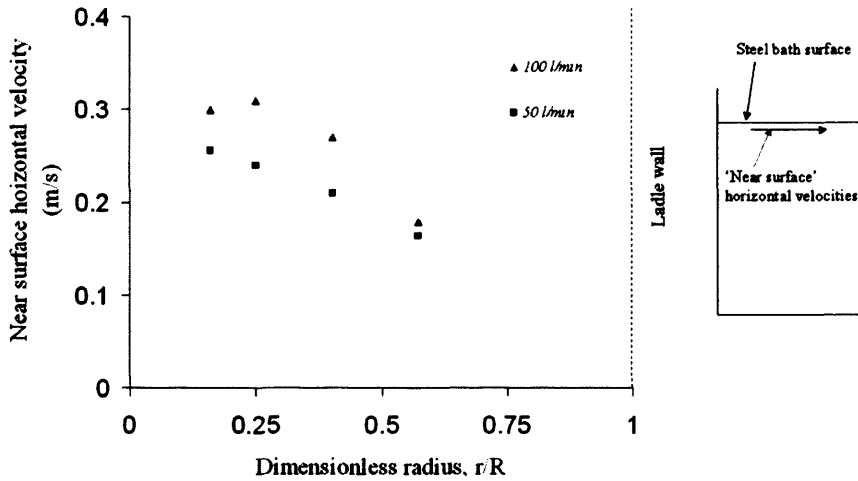


Figure-53. The predicted results in the present work (case 2) for the near-surface velocities for different gas flow rates (60 tonne).

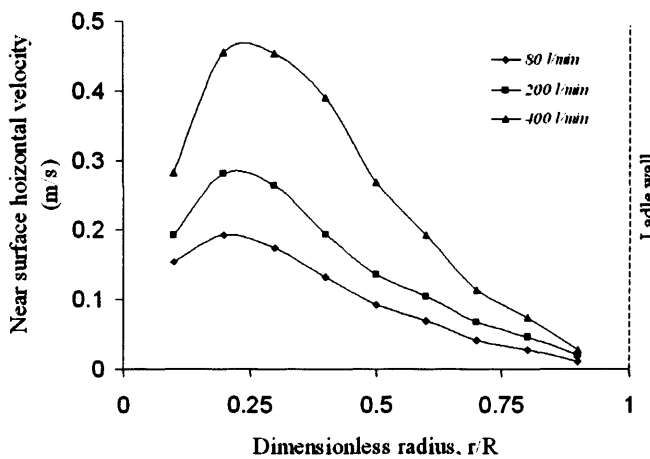


Figure-54. Predicted values in the present work of the molten steel near-surface velocities 'in the horizontal axis' along the radius of a 100 t ladle vessel at various gas flow rates (case 3).

4.1.2 Fluid flow inside gas stirred ladle vessel.

The predicted velocity vectors of the steel flow field in the gas stirred ladle system for cases 3 and 4 using gas flow rates of 80 and 400 l/min respectively are shown in figure 55. The velocity vector of the steel flow field for case 8 using a total gas flow rate of 400 l/min through two off centre nozzles is presented in figure 56. The stream flow is different in comparison with Jonsson [2] work using similar operation conditions. This is discussed later in chapter 5.

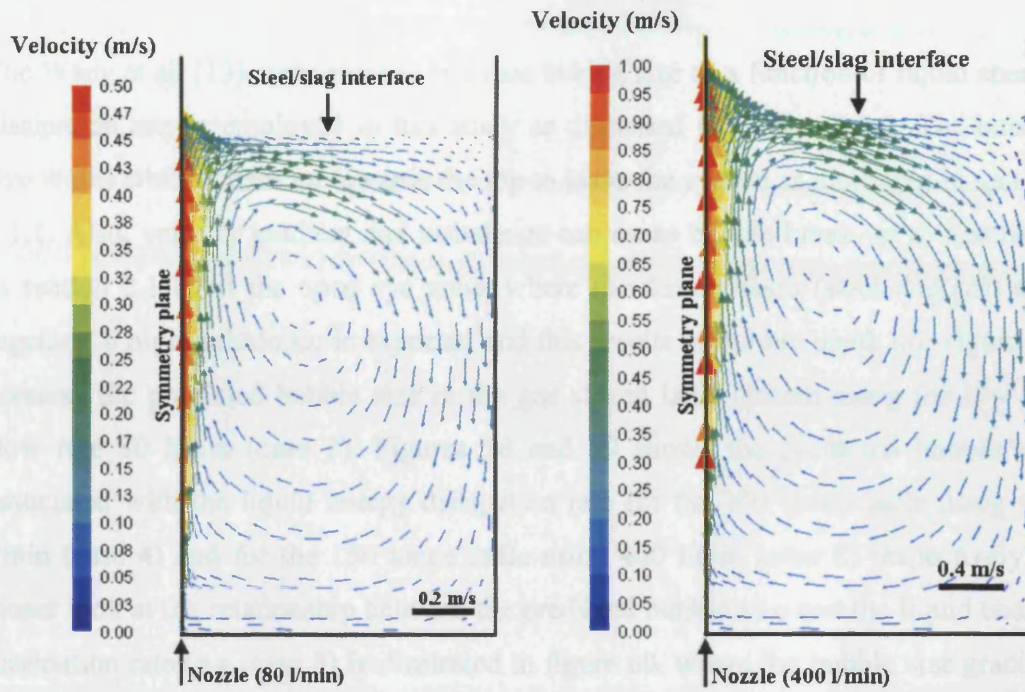


Figure-55. Velocity vectors for the molten steel flow field in the 100 tonne ladle. Two gas flow rates were used 80 l/min (left) and 400 l/min (right).

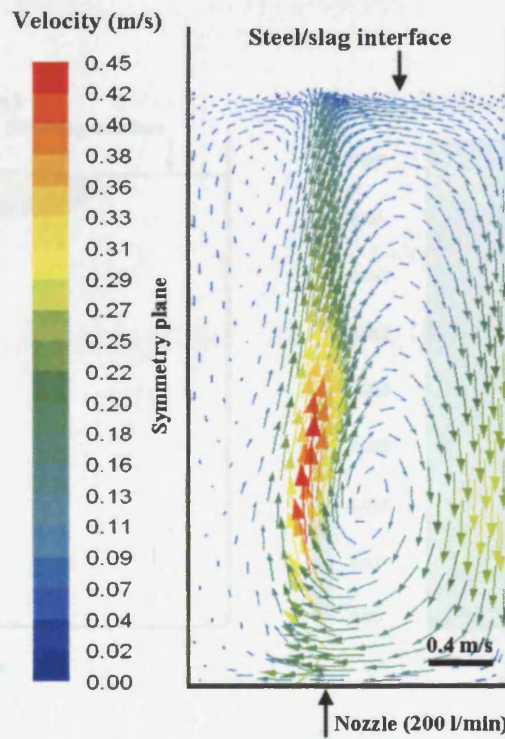


Figure-56. Velocity vectors for the molten steel flow field in the 150 tonne ladle. Two off centre nozzle located at the bottom wall where the gas flow rate used is 200 l/min per nozzle.

4.1.3 Bubble size and energy dissipation rate.

The Wang et al. [13] correlation to estimate bubble size as a function of liquid energy dissipation rate is employed in this study as discussed in section 3.3.2. The bubble size varies while it rises up towards the top to leave the system as discussed in section 2.1.1. Also, velocity gradient and turbulence can cause bubble break-up as discussed in section 2.1.1. At the open eye zone, where the three phases (steel/slag/gas) mix together, a high turbulence is expected and this results in bubble break up. Figure 57 presents the predicted bubble size in the gas stirred ladle system using the low gas flow rate 80 l/min (case 3). Figures 58 and 59 shows the predicted bubble size associated with the liquid energy dissipation rate for the 100 tonne ladle using 400 l/min (case 4) and for the 150 tonne ladle using 400 l/min (case 8) respectively. A closer look at the relationship between the predicted bubble size and the liquid energy dissipation rate (e.g. case 3) is illustrated in figure 60, where the bubble size gradient along the symmetry axis line is drawn against the calculated liquid energy dissipation rate for the 100 tonne ladle using 80 l/min. Figure 61 illustrates the variation in the bubble rising velocity during the refining process time in case 3.

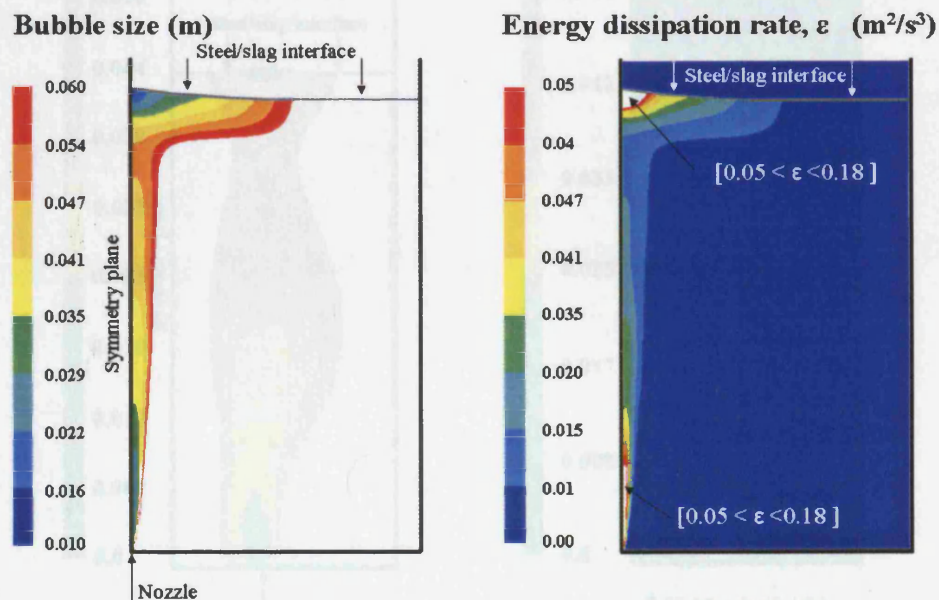


Figure-57. The estimated bubble size contours in the 100 tonne ladle (left). The associated liquid energy dissipation rate (right). The gas flow rate used is 80 l/min (case 3).

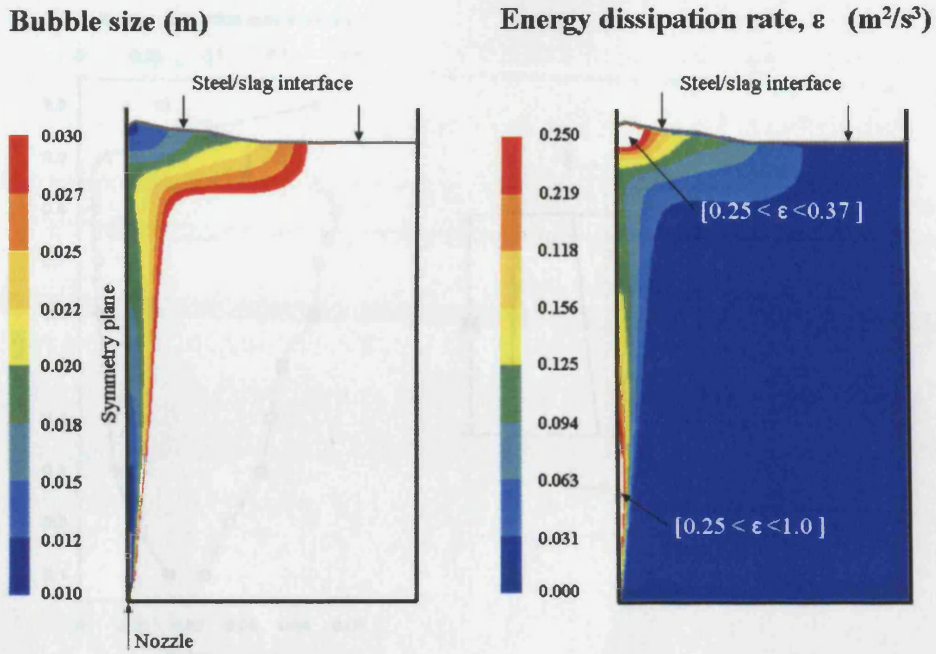


Figure-58. The estimated bubble size contours in the 100 tonne ladle (left). The associated liquid energy dissipation rate (right). The gas flow rate used is 400 l/min (case 4).

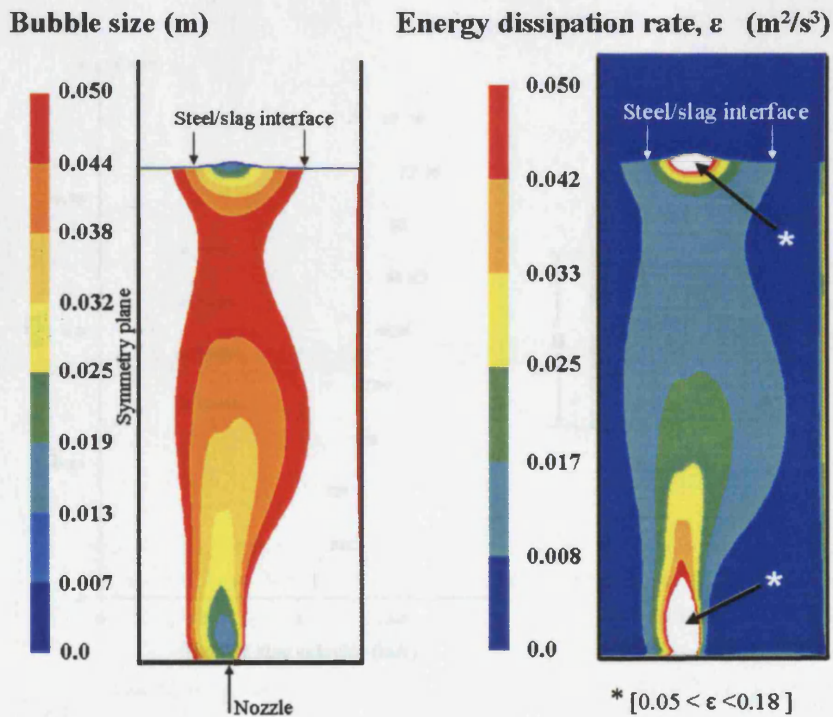


Figure-59. The estimated bubble size contours in the 150 tonne ladle (left). The associated liquid energy dissipation rate (right). Two off centre nozzles were located at the bottom wall and the gas flow rate used is 200 l/min per nozzle (case 8).

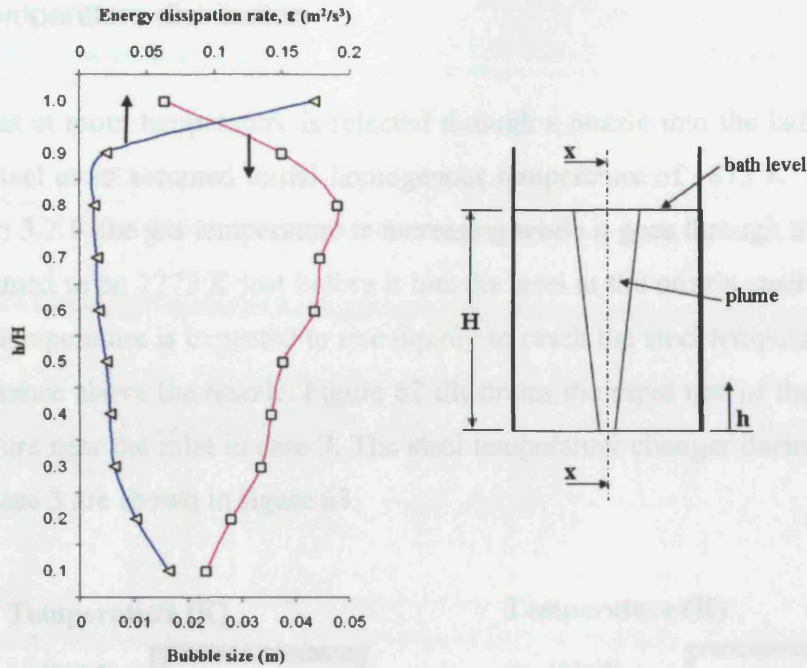


Figure-60. The estimated bubble size along the xx axis (exposed in the right sketch) drawn in comparison with the variation in the liquid energy dissipation rate along the same axis in the 100 tonne ladle. The gas flow rate used is 80 l/min (case 3).

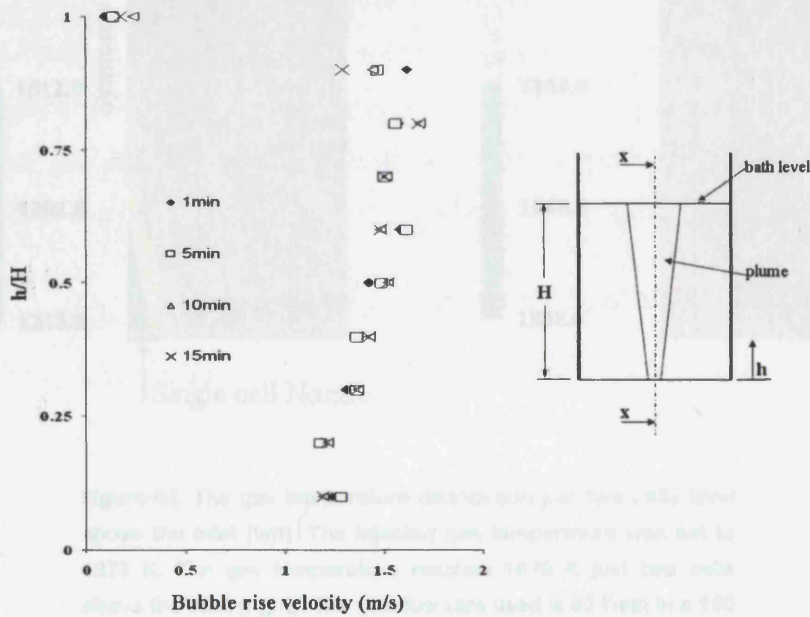


Figure-61. The variation in the bubble rise velocity along the xx axis (exposed in the right sketch) during the refining process in the 100 tonne ladle. The gas flow rate used is 80 l/min (case 3).

4.1.4 Temperature distribution

Argon gas at room temperature is injected through a nozzle into the ladle filled with molten steel at an assumed initial homogenous temperature of 1873 K. As discussed in section 3.2.1, the gas temperature is increasing while it goes through the nozzle and it is assumed to be 1273 K just before it hits the steel at the nozzle steel side surface. The gas temperature is expected to rise rapidly to reach the steel temperature within a short distance above the nozzle. Figure 62 illustrates the rapid rise of the injected gas temperature near the inlet in case 3. The steel temperature changes during the process time in case 3 are shown in figure 63.

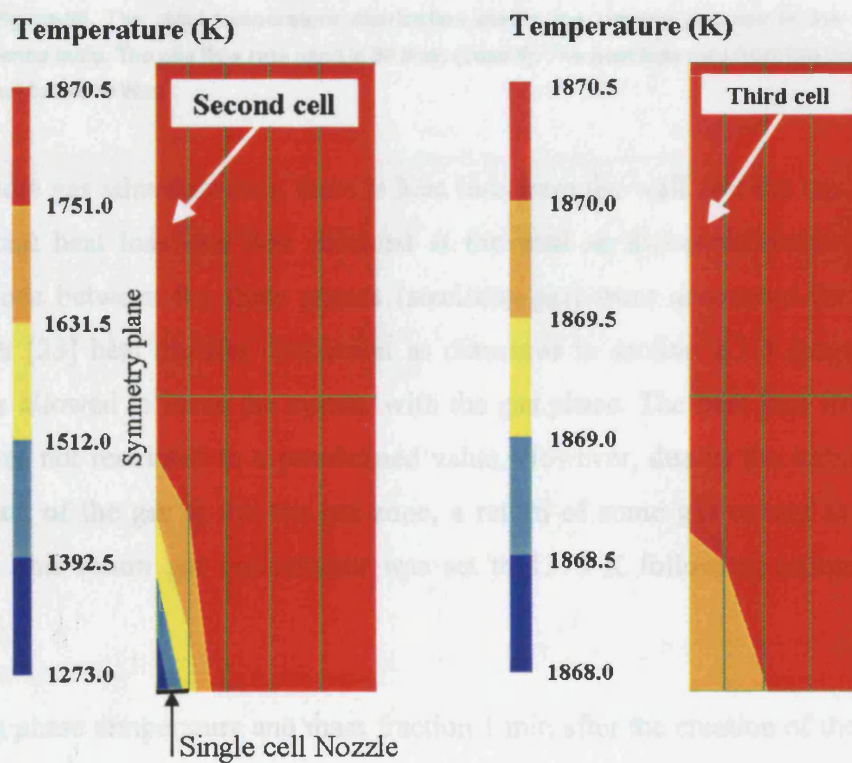


Figure-62. The gas temperature distribution just two cells level above the inlet (left). The injected gas temperature was set to 1273 K. The gas temperature reaches 1870 K just two cells above the inlet (right). The gas flow rate used is 80 l/min in a 100 tonne ladle (case 3).

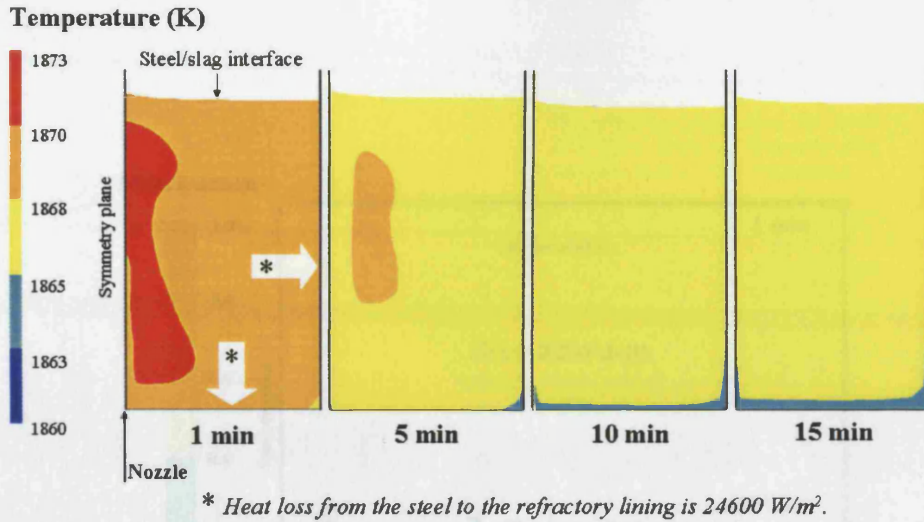
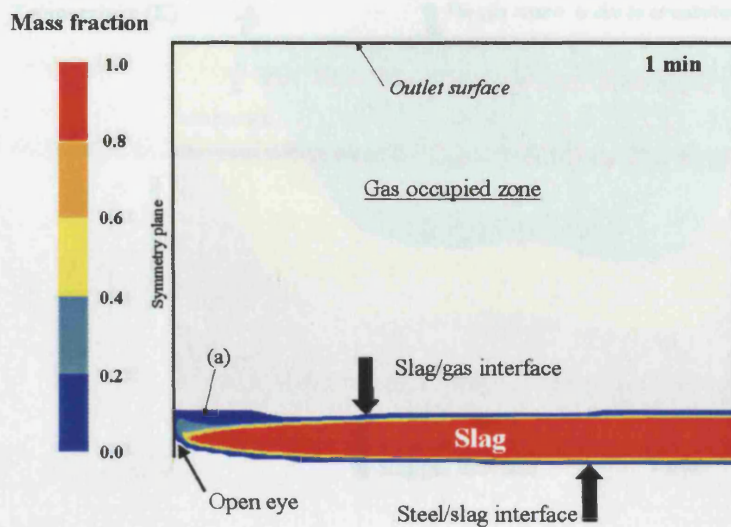


Figure-63. The steel temperature distribution during the refining process in the 100 tonne ladle. The gas flow rate used is 80 l/min (case 3). The heat loss rate from the wall is set to 24600 W/m^2 .

In the ladle gas stirred system, there is heat loss from the wall and the top slag layer. A constant heat loss rate was assumed at the wall as discussed earlier. The heat interactions between the three phases (steel/slag/gas) were accounted for using the Whitaker [23] heat transfer coefficient as discussed in section 2.1.3 (page 16). The heat was allowed to leave the system with the gas phase. The heat loss from the top outlet was not restricted to a pre-defined value. However, due to the turbulence and circulation of the gas at the top gas zone, a return of some gas occurs at the outlet surface. This return gas temperature was set to 1373 K following estimation from industry.

The slag phase temperature and mass fraction 1 min after the creation of the open eye in case 3 are given in figures 64 and 65 respectively. The initial slag and gas temperature were assumed to be 1873 K. The change in the gas temperature distribution during the process time is illustrated in figures 66 to 69.



(a) Slag gas mixture consisting of more than 80% gas.

Figure-64. The slag phase mass fraction 1 min after the creation of the open eye. The lower side of the slag is mixing with the molten steel, and the upper side of the slag is mixing with the gas. At point (a) near the open eye a high turbulence rate occurs due to the gas leaving. Except near the open eye zone, the slag mass fraction remains the same during the refining process. The gas flow rate used is 80 l/min in the 100 tonne steel (case 3).

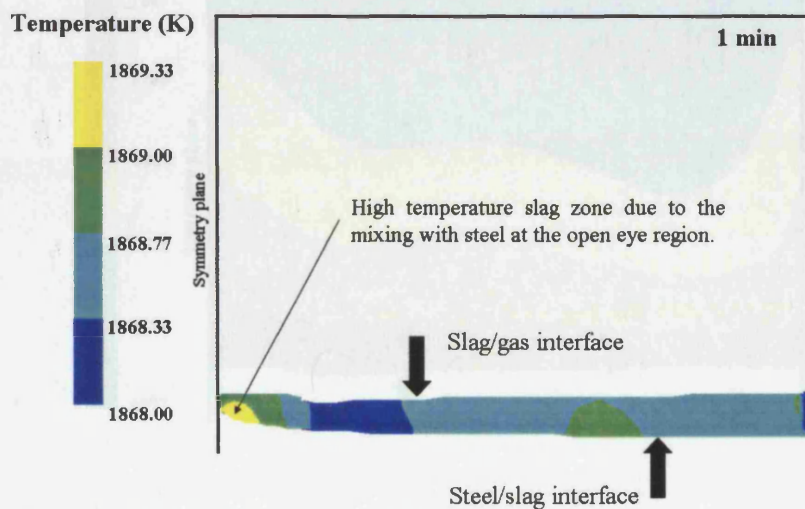


Figure-65. The slag phase temperature distribution 1 min after the creation of the open eye. The lower side of the slag layer near the open eye has a hot spot where the slag mixes with the steel. The gas flow rate used was 80 l/min in the 100 tonne steel vessel (case 3).

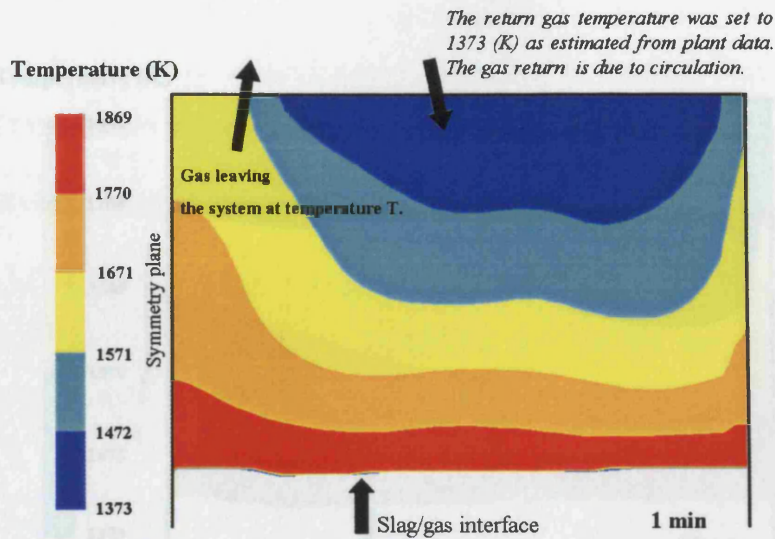


Figure-66. The gas phase temperature distribution in the upper occupied gas zone 1 min after the creation of the open eye. The gas temperature at the slag/gas interface is high due to the heat exchange between the two materials. The gas flow rate used was 80 l/min in the 100 tonne steel vessel (case 3).

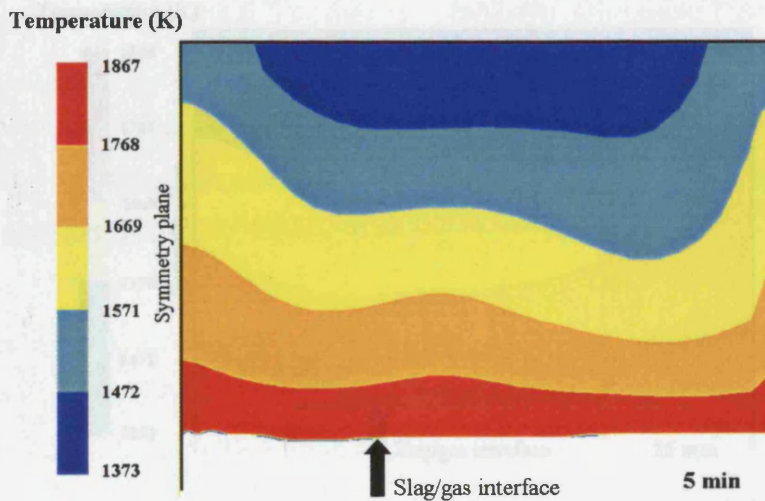


Figure-67. The gas phase temperature distribution in the upper occupied gas zone 5 min after the creation of the open eye. The gas flow rate used was 80 l/min in the 100 tonne steel vessel (case 3).

4.2 CFD and thermodynamic coupling results

Following scrutiny of the CFD results (see discussion in section 5.1), the gas stirred ladle system was modelled in a 2D axisymmetric geometry using the thermodynamic package MTDATA. The model was run using the same parameters as those used in the previous work.

The temperature distribution in the upper occupied gas zone 10 min after the creation of the open eye is shown in Figure 68. The gas flow rate used was 80 l/min in the 100 tonne steel vessel (case 3).

The influence of a low CaO mobility and the precipitation of CaS phase in the slag on the desulfurization rate was investigated (case 7). These results are shown in Figure 69.

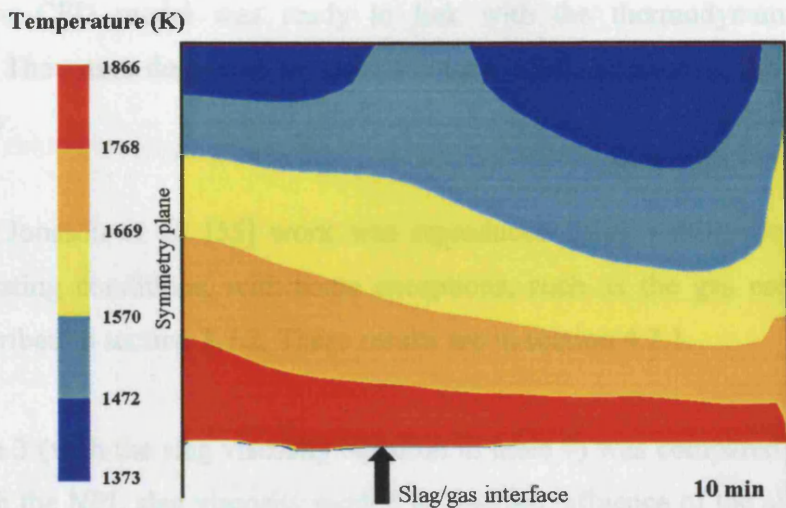


Figure-68. The gas phase temperature distribution in the upper occupied gas zone 10 min after the creation of the open eye. The gas flow rate used was 80 l/min in the 100 tonne steel vessel (case 3).

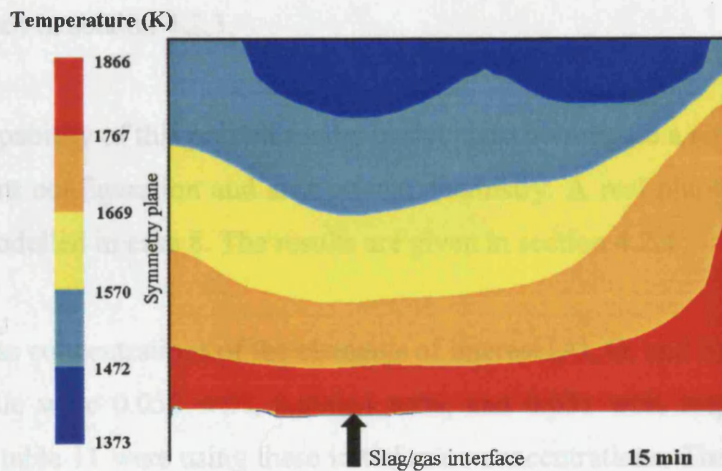


Figure-69. The gas phase temperature distribution in the upper occupied gas zone 15 min after the creation of the open eye. The gas flow rate used was 80 l/min in the 100 tonne steel vessel (case 3).

4.2 CFD and thermodynamic coupling results

Following scrutiny of the CFD results (see discussion in section 5.), the gas stirred ladle system CFD model was ready to link with the thermodynamic package MTDATA. The cases described in table 11 were used to examine the four major issues below.

- The Jonsson et al. [55] work was reproduced using similar boundary and operating conditions, with some exceptions, such as the gas escape system described in section 3.7.2. These results are in section 4.2.1.
- Case 3 (with the slag viscosity equation in table 9) was compared with case 5 (with the NPL slag viscosity model) to find the influence of the slag viscosity model on the desulphurization rate. Also, the influence of the gas flow rate on the desulphurisation rate was investigated (cases 3, 4, 5 and 6). These results are given in section 4.2.2.
- The influence of allowing Ca^{++} mobility and the precipitation of CaS phase in the slag on the desulphurisation rate was investigated (case 7). These results are given in section 4.2.3.
- The capability of this present model to switch to investigate a new system with different configuration and slag system chemistry. A real plant data example was modelled in case 8. The results are given in section 4.2.4

The initial mass concentrations of the elements of interest (Al, O, and S) in steel in the 100 tonne ladle were 0.052 wt%, 0.00044 wt%, and 0.031 wt% respectively. The cases (3-7) in table 11 were using these initial mass concentrations. The slag contains 55 wt% CaO, 30 wt% Al_2O_3 , 7.5 wt% SiO_2 , and 7.5 wt% MgO. The applied gas flow rate for each case is given in table 11. In case 7 the CaS phase was accounted for and allowed to precipitate, and the reduction in CaO mass fraction in the slag phase due to the CaS precipitation was monitored. The variation in slag viscosity due to

composition changes in case 7 was detected using the NPL slag model discussed in section 2.2.3 (ii (b)).

The initial mass concentrations of the elements of interest (Al, O, and S) in steel in the 150 tonne ladle were 0.06 wt%, 0.0777 wt%, and 0.012 wt% respectively (estimation from industry). The slag contains 50.92 wt% CaO, 29.37 wt% Al₂O₃, 6.07 wt% SiO₂, and 10.3 wt% MgO with less than 1.0 wt% FeO, MnO, and P₂O₅. FeO, MnO, and P₂O₅ were not accounted for in this study. One of the advantages of the MTDATA package is the ease with which these additional elements and oxides can be added into the analysis.

4.2.1 Model validation

For case 3 figure 70 illustrates the way in which the concentration of the elements of interest (Al, S, O) changes over the first minute of refining. The change in steel sulphur content during the refining process is shown in figure 71. Figure 72 illustrates the high sulphur concentration in the slag near the bubble zone. This is in agreement with experiment [112]. The predicted desulphurization rate over time is shown in figure 73 and is in good agreement with [2]. Also the sensitivity of the calculation for sulphur content to the MTDATA interface rate is illustrated in figure 73.

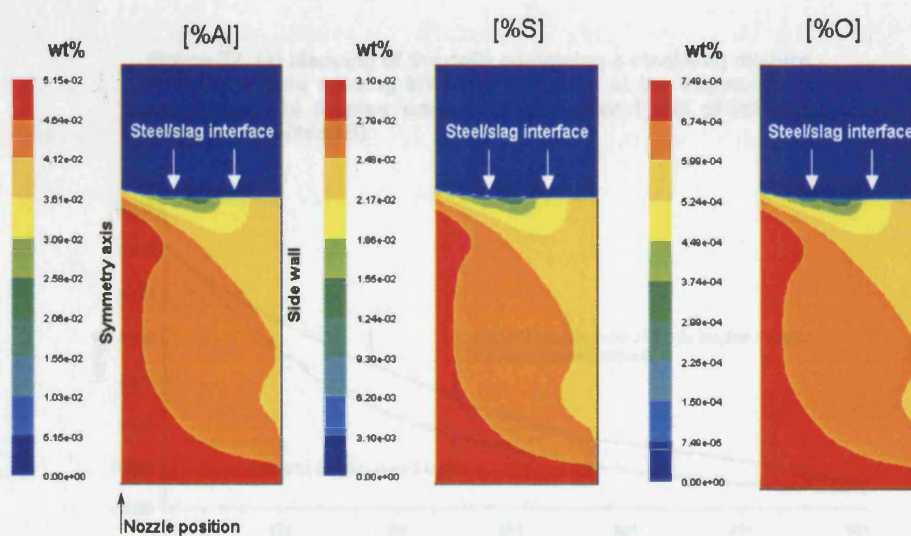


Figure-70. The aluminium, sulphur and oxygen mass concentration in steel after 1 min of refining process (case 3).

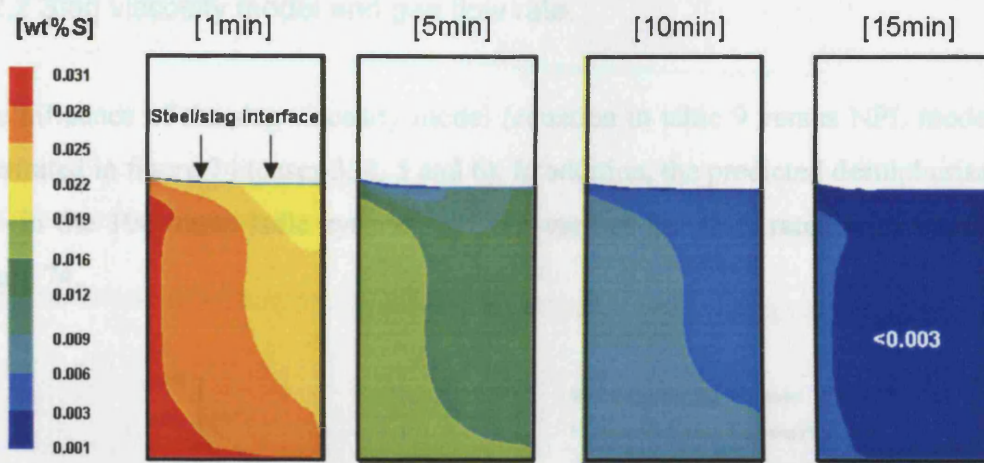


Figure-71. Sulphur mass concentration changes during the steel refining process (case 3).

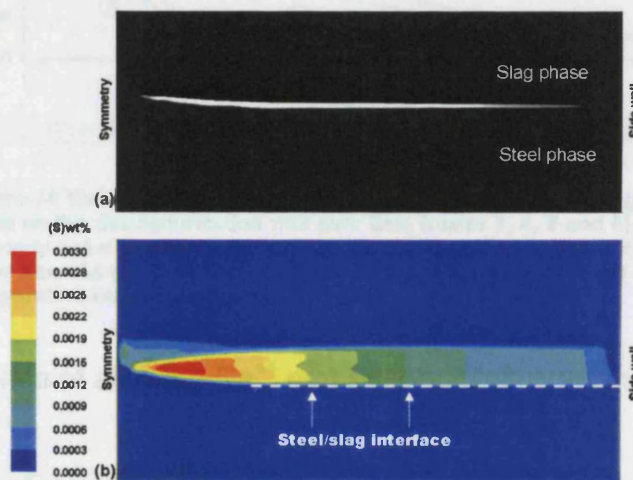


Figure-72. (a) Mapping of the cells containing a steel/slag mixture at the interface causing MTDATA execution at the beginning of calculation. (b) Sulphur content in slag after 1 min of refining process start (case 3).

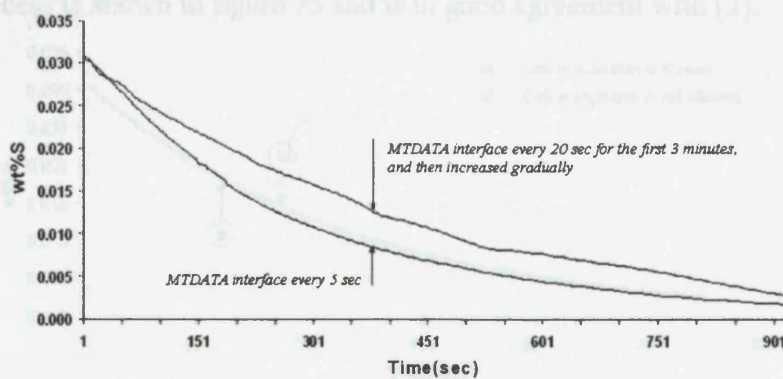


Figure-73. Sensitivity of the prediction of sulphur content to the MTDATA interface rate (case 3).

4.2.2 Slag viscosity model and gas flow rate.

The influence of the slag viscosity model (equation in table 9 versus NPL model) is illustrated in figure 74 (cases 3, 4, 5 and 6). In addition, the predicted desulphurisation rate in the 100 tonne ladle system applying various gas flow rates is illustrated in figure 74.

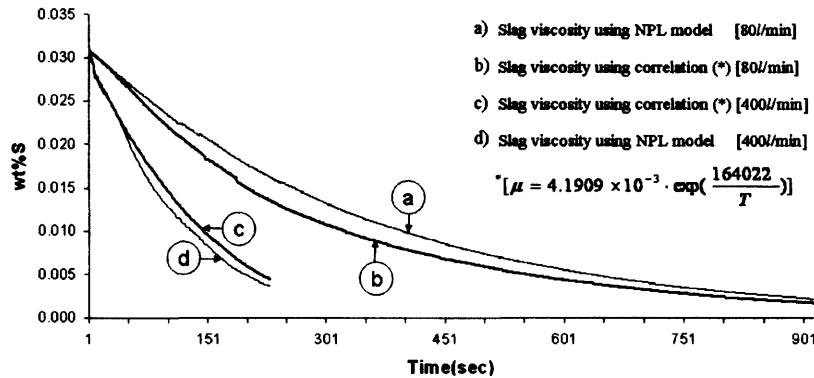


Figure-74 The influence of the gas flow rate and the estimated slag viscosity value on the desulphurization rate over time (cases 3, 4, 5 and 6). The slag viscosity value predicted by the correlation (equation in table 9) is about three times larger than that predicted by the NPL model over the operation temperature range (see figure).

4.2.3 The influence of allowing Ca^{++} mobility and CaS precipitation

In this present work case 7 was run to study the influence of allowing Ca^{++} mobility and CaS precipitation on the desulphurization rate (see section 3.1). Figure 75 presents the desulphurization rate over time, comparing with case 5 where the slag compositions are assumed to be constant. The desulphurization rate during the refining process is shown in figure 75 and is in good agreement with [2].

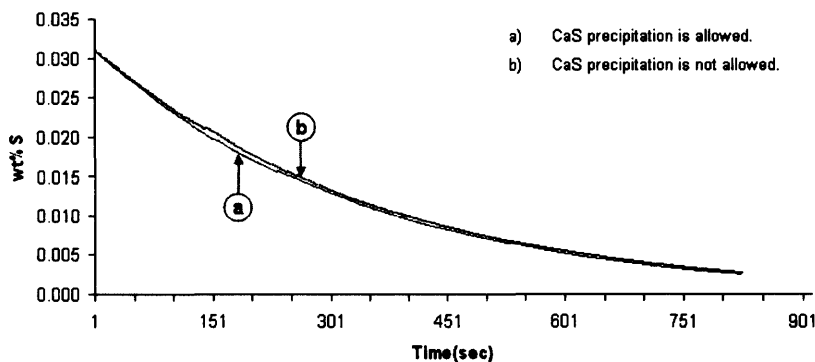


Figure-75. The predicted desulphurization rate during the refining process ((a) case 7, (b) case 5).

4.2.4 Real plant data

In this present work case 8 was run to model real plant data (case 8) with some simplifications in the ladle geometry (as discussed in section 5.1.1, see figure 80). The desulphurization rate during the refining process is shown in figure 76.

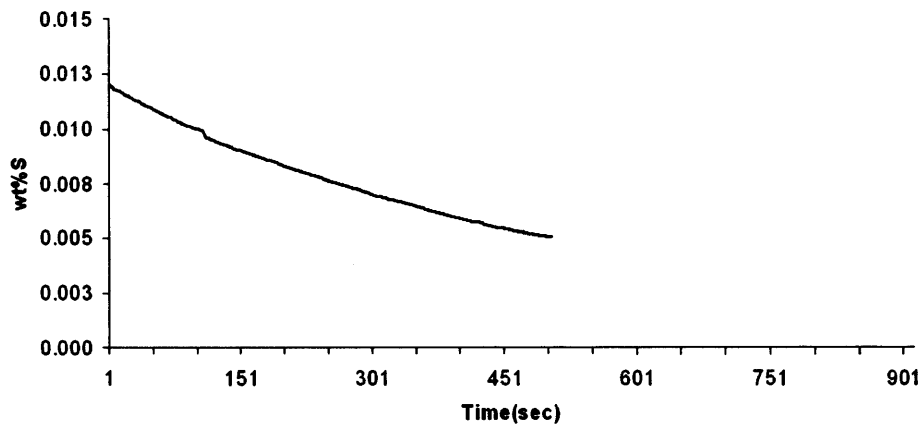


Figure-76. The predicted desulphurization rate during the refining process (case 8). The shadow region indicates the final acceptable sulphur level in steel for this particular production.

5. Discussion

In this chapter the results given in chapter 4 are discussed in the following order:

- Gas stirred system, CFD results.
 - Fluid flow in the gas stirred ladle vessel.
 - Gas bubble size.
 - Temperature distribution.

- CFD and thermodynamic coupling results.
 - The effect of the change in the rate of interfacing between Fluent and MTDATA
 - The influence of the use of the NPL slag viscosity model
 - The influence of allowing CaS precipitation
 - Real plant case

5.1 Gas stirred system, CFD results discussion

In this present work a selected combination of mathematical correlations describing steel/slag/gas thermo physical properties and the interactions between those phases were set and solved using a numerical algorithm. The Turkoglu and Farouk [4] approach was applied for the first time in the three phase steel/slag/gas model. Therefore, a proper validation of such a comprehensive model is essential. As discussed in section 3.8 two cases (cases 1 and 2) from the literature were selected for the fluid flow and heat transfer validation.

The developed model formulation and features were examined against selected experimental and mathematical work published in the literature. The mathematical formulation and features described in chapter 3 can be summarized as follow:

- The transport equations were solved separately for each phase.
- Eulerian multiphase model was employed
- Wang et al. [13] bubble correlation as a function of the liquid energy dissipation rate was applied to estimate the gas bubble size.
- The improved Whitaker [23] heat transfer correlation was used instead of the classical Ranz and Marshal [110] correlation.
- An extra gas occupied zone on the top of the top slag layer was added to the system instead of the classical wall/symmetry plane linked with a gas escape sink source.
- Two drag coefficient correlations (“Morsi and Alexander” and “Symmetry”) were used to define the momentum exchange between the three phases steel/slag/gas.

The CFD model prediction results given in section 4.1 are discussed and validated as required in the following sections 5.1.1, 5.1.2, and 5.1.3.

5.1.1 Fluid flow inside the gas stirred ladle vessel

The steel flow field velocity vectors given in section 4.1.2 (gas flow rate of 80 l/min in a 100 tonne ladle vessel, case 3) is in good agreement with Jonsson [2] where a single circulation of a similar velocity order was predicted. On the other hand the stream flow is different in comparison with Jonsson [2] work using the similar operation conditions as illustrated in figure 77. This could be due to the addition of the gas zone on the top of the slag layer to allow gas escape and the difference in the predicted gas bubble size as discussed in section 4.1.3. However, the prediction of molten steel near-surface velocity ‘in the horizontal axis’ shows in figure 53 is in good agreement with Hsiao et al. [111] who reported experimental results that are of the order of 0.1-0.4 m/s. Figure 78 presents case 2 prediction of the molten steel near-surface velocity ‘in the horizontal axis’ in comparison with Hsiao et al. [111].

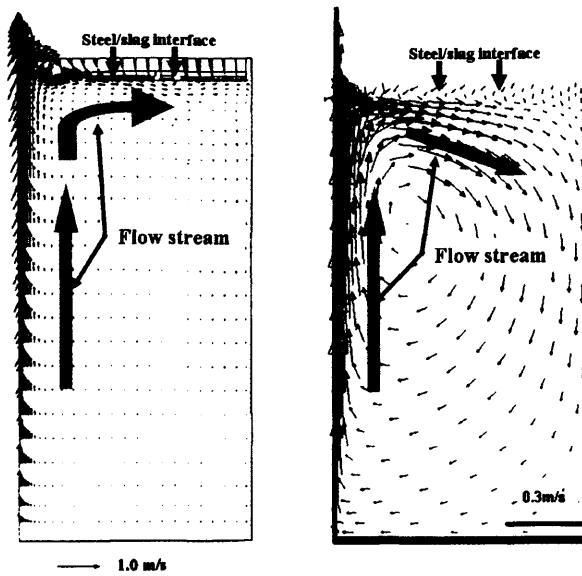


Figure-77. The velocity vectors for the molten steel flow field in the 100 tonne ladle (right). Jonsson et al. [55] predicted velocity vectors in the 100 tonne ladle (left). The flow stream pattern shows some variation between the two predictions. The gas flow rate is 80 (l/min).

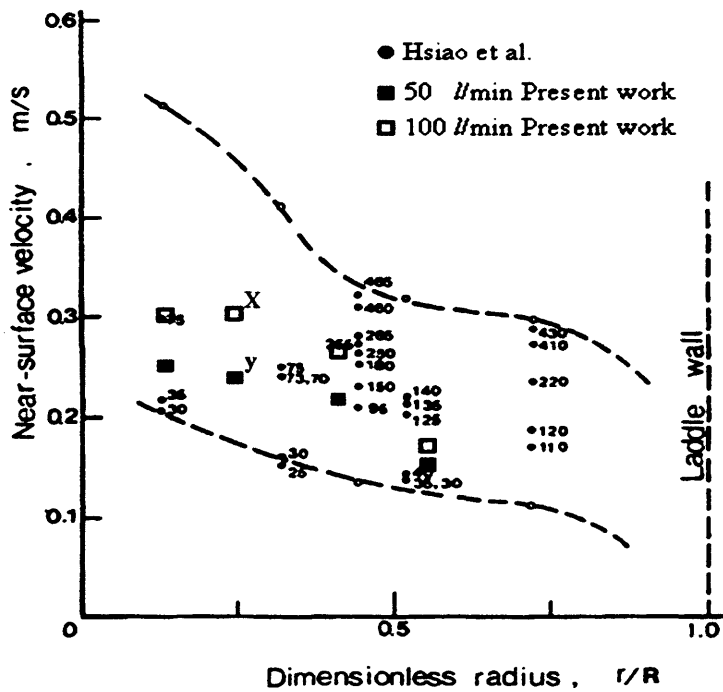


Figure-78. The measured molten steel near-surface velocities by Hsiao et al. [111] along the radius of a 60 tonne ladle vessel. Numbers on the diagram are gas flow rate. The predicted results in the present work (case 2) for the near-surface velocities for different gas flow rates are placed on the diagram for comparison. The gas flow rates are in (l/min). Points x and y will be referred to in the text.

The present approach was compared with Hsiao et al. [111] experimental work on 60 tonne ladle. The velocities near the surface increased with an increase of the gas flow rate. Hsiao examined a 40 tonne ladle reported by Jonsson and Jonsson [26] which showed a similar behaviour where the near surface velocities increased with an increase of the gas flow. Unfortunately not enough consistent data about the 40 tonne ladle geometry were available. However, Jonsson and Jonsson [26] predicted that the near surface velocities at half the radius of the 40 tonne ladle were not increasing with the gas flow rate as illustrated in figure 79. Jonsson [82] concludes that their approach to model the free surface might need some improvements in order to achieve a better prediction of the velocities near the surface.

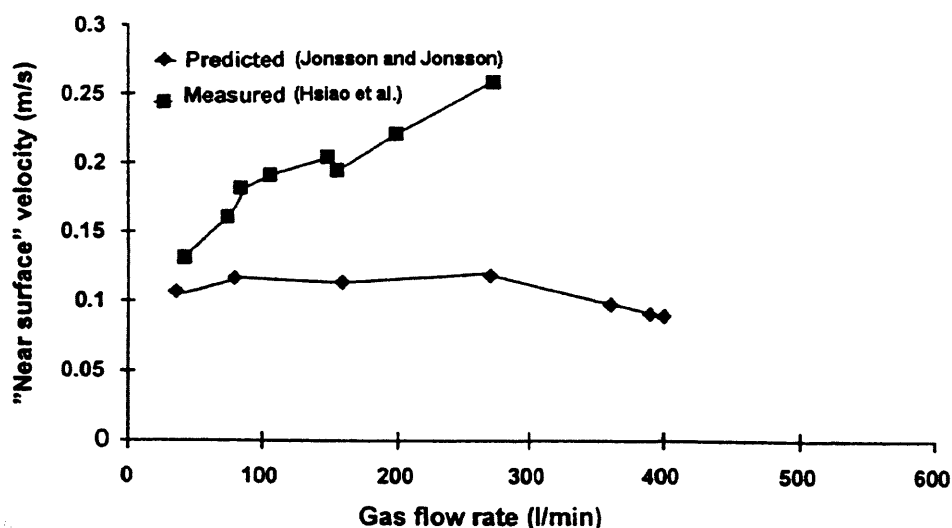


Figure-79. A comparison between the predictions by Jonsson and Jonsson [26] and measured near-surface velocities [111] at location half radius from the centre. The experimental work was done using a 40 t ladle vessel.

The slag layer was removed prior to the trials in the Hsiao et al. [111] experimental work. Therefore, a two phase (steel/gas) model was built (case 2) to simulate the experimental work to produce the prediction results illustrated in figure 53 (page 81). In this two phase model, one drag coefficient correlation was required to define the momentum interaction between the two phases (steel/gas). Morsi and Alexander [100] drag model discussed in section 3.3 was used in this case. Due to the high density variation between the two materials (steel/gas) a lot of numerical difficulties arose at the steel/gas interface zone (and not at the plume area). Due to the gas injection the molten steel inside the ladle vessel started to circulate. This results in a creation of a

wavy surface of the steel bath. This behavior was absorbed easily in the three phase model (steel/slag/gas) due to the presence of the slag layer between the steel bath and the top gas zone. The presence of the slag layer solves two main problems; first the density variation between phases; secondly it allows the use of more than one drag correlation to define the interaction between phases as discussed in section 3.3. The wavy surface of the steel bath in the three phase model was solved easily due to smaller density difference at the steel/slag interface in comparison with the two phase model where the steel bath surface interacts with the gas phase directly. On the other hand, the slag phase density is still much larger in comparison with the gas density. This was countered by the creation of a finer mesh at the slag/gas interface and most importantly the top surface of the slag layer at the slag/gas interface was still until the creation of the open eye where a sort of stability was achieved. Also, the symmetry drag coefficient was employed to define the interaction between the steel and the slag phases in the three phase model. This is recommended for use in the case of a continuous secondary phase as discussed in section 3.3. The use of the symmetry drag coefficient provides a high stability to the solution with respect to the interaction at the steel bath surface in the three phase (steel/slag/gas) model.

Examining figure 78, in the results for 100 l/min, the second point (labelled x) is slightly higher than the first. For the 50 l/min, the second point (labelled y) is lower than the first. This inconsistency might occur because this calculation is a two-phase calculation. Figure 54 shows the same calculation for three-phases (but for the system under consideration here and not for Hsiao et al. system). In this case, the curve rises before falling.

In contrast to Jonsson and Jonsson [26] and Grip and Jonsson [92] the present predicted open eye size in a 100 tonne ladle increases with the gas flow rate increase [113]. The most likely reason for this is the use of the top occupied gas zone as a gas escape mechanism.

The steel flow field velocity vectors given in section 4.1.2 (gas flow rate of 200 l/min per nozzle in a 150 tonne ladle) show an almost straight column of the gas phase inside the molten steel bath (figure 56). This creates an open eye in the top slag layer in line with the nozzle location in the bottom wall. This results in a creation of two

open eyes in the top slag layer in the full system (the diagrams presented here are only one half of the symmetrical system). However, the author's personal observation during a visit to industry arranged in Feb 2006 was that only a single giant open eye was created. This inconsistency can be explained as follows. In the industrial plant the nozzles are in fact not location on the same diameter, one is off-set (see figure 80). The model has to be 2-D rather than 3-D because of time concerns and issues of complexity. The location of the nozzles has therefore been simplified so that both lie on a single diameter (figure 80). The new nozzle locations change the energy balance inside the system causing twin open eyes rather than a single open eye. Figure 81 illustrates the influence of the nozzle location on the created gas stream/column place [114].

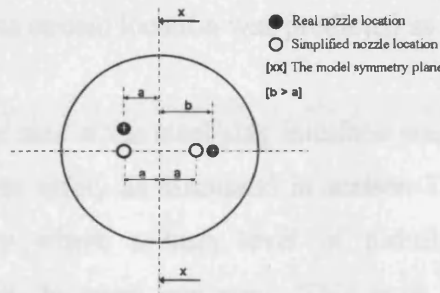


Figure-80. A schematic diagram showing the location of the nozzles in the bottom wall. 'Real' = location in the industrial plant. 'Simplified' = location in the 2-D model.

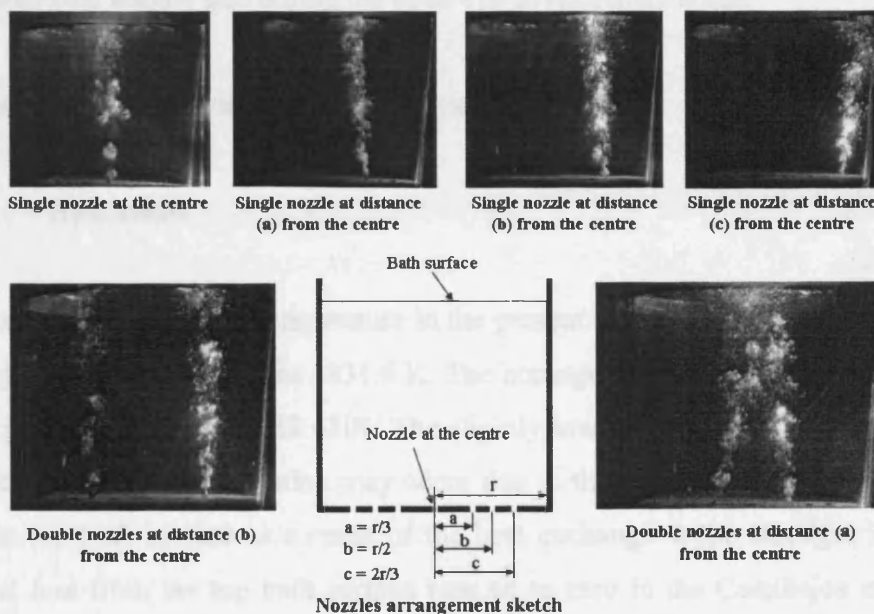


Figure-81. Photographs illustrating the influence of the nozzle(s) location on the formed gas beam. A prototype air/water ladle model was used to conduct this experimental work. The sketch in the middle presents the define nozzle locations [114].

5.1.2 Bubble size

As discussed earlier in section 2.1.1, the bubble size varies while it rises to the top. Also the variation in velocity, pressure, and turbulence will cause a bubble to break up. Therefore, a proper model to describe these variations is essential. The incorrect estimation of the bubble size could cause incorrect prediction of the domain flow pattern. This was experienced in this present work and is described here to illustrate the effect of bubble size. Case 8 was loaded (using Wang model) with a bath height of 2.4 m for a 100 tonne ladle when it should have been 3.2 m. The bubble size above this height (2.4m) was set to a constant value of a 0.0001 m. The gas stream/column was shifted to the wall side instead of giving a straight stream/column as shown in figure 56, matching with the experimental results given in figure 81. When the case was corrected a proper gas stream location was predicted as discussed in section 5.1.1.

A relatively small bubble size at the steel/slag interface was required to allow the gas to penetrate the slag layer safely as discussed in section 3.7.3. This agrees with the bubble break up theory where a high level of turbulence is expected at the steel/slag/gas interface at the open eye zone. This zone would stabilize after the creation the open eye and a larger bubble size was predicted at this zone than the initial predicted bubble size during the open eye development stage.

5.1.3 Gas stirred ladle system thermal analysis

i) Heat losses

The predicted homogenous temperature in the present mathematical formulation after Castillejos et al. [93] work was 1831.6 K. The homogenous temperature predicted by Castillejos et al. [93] was 1832.65 K. The slightly lower temperature value predicted by the current model formulation may occur due to the fact that heat loss is allowed from the top bath surface as a result of the heat exchange at the steel/gas interface. The heat loss from the top bath surface was set to zero in the Castillejos et al. [93] work. This would indicate the successful implementation of the estimated constant heat loss rate.

During secondary steelmaking, the system loses heat to the surroundings. The molten steel loses heat through the walls and the top slag layer. Also some heat is lost with the leaving gases. As discussed in section 3.2.2, Castillejos et al. [93] suggest a constant heat loss rate through the wall, but the heat loss from the top surface was ignored. The heat loss through the top slag layer had an estimated constant rate (4000 W/m^2) in work by Jonsson [82], (6000 W/m^2) in work by Jonsson and Jonsson [26], and in other places [2, 89] it was set to (43800 W/m^2). In this present work, the estimation/neglect of the heat loss from the top slag layer was avoided by using the top occupied gas zone discussed earlier. A proper selection of the height of the top occupied gas zone (see section 3.7.3) provides a reasonable estimation of the gas/slag interface temperature variation given in section 4.1.3. The drop of the gas temperature leaving the system does not affect the slag/steel temperature as discussed earlier in section 3.7.3 during the early stages of this model development.

As shown in table (12) (section 4.1.1 i) the heat loss rate from the outlet surface decreases during the process time. This is consistent with the overall system temperature which decreases during the process time as can be observed from the steel temperature (the heat source) drop during the process given in section 4.1.3. The range of the predicted heat losses from the outlet surface (table 12) is in reasonable agreement with the value estimated by Jonsson and Jonsson [26] (6000 W/m^2).

Looking at the predicted steel temperature variation during the refining process given in figure 63 (assuming a constant heat loss rate, page 87), the steel temperature drop during the process time (15 minutes) was about 8 degrees. In secondary steelmaking the estimated steel temperature drop rate is about 1 to 2 degree per minute. This predicted low temperature drop rate could be due to the use of the 2D model rather than an axi-symmetric model (Jonsson et al. [2] model was an axi-symmetric). This results in a lower cooling rate. However, the agreement is taken to be reasonable given that in the industrial practice the heat loss rate will not be constant.

ii) Choice of the turbulent Prandtl number

The role of the Turbulent Prandtl number was discussed in section 3.1.2. The Kays and Crawford [115] equation, equation (50), was used to calculate the turbulent

Prandtl number over the entire domain of the gas stirred ladle system. Figure 82 shows the calculated turbulent Prandtl number using the constant ($Pr_{\text{too}}=0.85$) in comparison with Weigand et al. [97] modification described in equation (52).

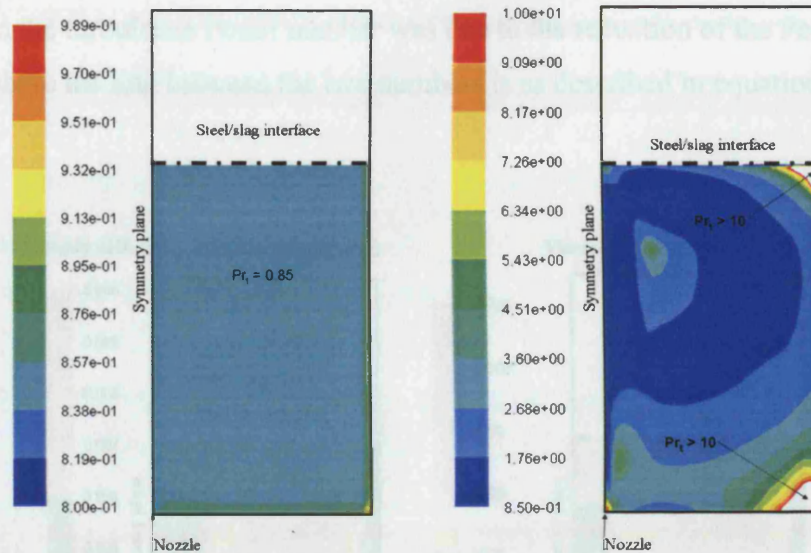


Figure-82. The calculated turbulent Prandtl number using the constant ($Pr_{\text{too}}=0.85$) (left). The calculated turbulent Prandtl number using Weigand et al. [97] modification (right). The gas flow rate used is 80 l/min in a 100 tonne ladle (case 3).

The calculation using the Weigand et al. [97] modification described in equation (52) results in a prediction of a very high turbulent Prandtl number at the locations shown in figure 82. These corners could be named “dead zones” where the flow velocity is very low as illustrated in figure 55 with the molten steel velocity vectors. This results in a reduction of the turbulence viscosity. Therefore the eddy diffusivity of the

momentum defined as $\left(\varepsilon_M = \frac{\mu_t}{\rho}\right)$ and the turbulence viscosity ratio (μ_t/μ) are also reduced in those corners as illustrated in figure 83.

The reduction in the turbulence viscosity ratio results in a reduction of the Peclet number defined in equation (51) that can be replaced by the following [95]:

$$Pe_t = Pr \left(\frac{\mu_t}{\mu} \right) \quad (68)$$

where the eddy diffusivity of the momentum is defined as $\left(\varepsilon_M = \frac{\mu_t}{\rho}\right)$ and the kinematic viscosity is $\left(\nu = \frac{\mu}{\rho}\right)$, where μ is the dynamic viscosity. Therefore, the rapid increase in the turbulence Prantl number was due to the reduction of the Peclet number where the link between the two numbers is as described in equation (50, page 52).

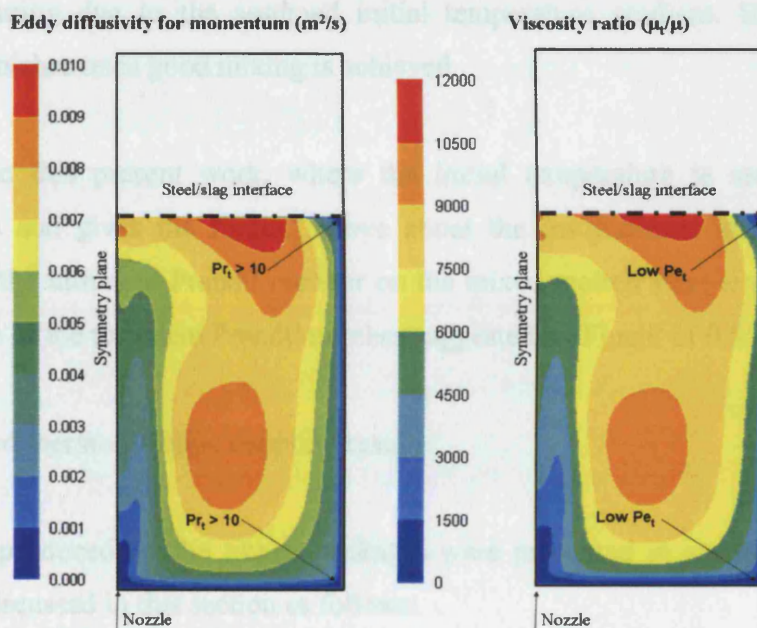


Figure-83. The estimated eddy diffusivity for momentum (left), and the estimated viscosity ratio (right) associated with the calculation of turbulent Prandtl number using Weigand et al. [97] modification. The gas flow rate used is 80 l/min in a 100 tonne ladle (case 3).

As discussed in section 3.1.2, only a constant value for the turbulent Prandtl number can be fed into the Fluent codes. The default Fluent turbulent Prandtl number is 0.85 and it is recommended that the default setting is not changed unless necessary. The Castillejos et al. [93] set up was examined using three different values of the turbulent Prandtl number (0.85, 3, and 10) selected within the range suggested by equation (50, page 52) and illustrated in figure 80. Figures 50-52 present the steel temperature variation at the eight selected points over the domain during the process time. Castillejos et al. [93] report a variation of the melt steel temperature over the entire domain of less than 4 degrees. Here complete homogenization of the melt was

achieved after 180 s. Therefore, running the analysis for 350 s is quite acceptable to absorb all the expected changes in the melt temperature.

Comparing the three figures 50, 51, and 52 (pages 79 and 80) it can be seen that quite good homogenization was achieved within 100 s from the start of the analysis for all the three turbulent Prandtl numbers examined. The final homogenised temperatures for the turbulent Prandtl numbers of 0.85, 3, and 10 are 1831.6 K, 1830.9 K, and 1830.85 K respectively. The influence of the turbulent Prandtl number was significant at the beginning due to the assumed initial temperature gradient. However, this influence vanishes once good mixing is achieved.

Therefore, in this present work, where the initial temperature is assumed to be homogenous and gives the finding above about the insignificant influence of the variation of the turbulent Prandtl number on the mixed molten steel temperature, the default value of the turbulent Prandtl number suggested by Fluent of 0.85 was used.

5.2 CFD and thermodynamic coupling results

The results produced by the linked packages were presented in section 4.2. These results are discussed in this section as follows:

- The effect of the change in the rate of interfacing between Fluent and MTDATA (section 5.2.1).
- The influence of the use of the NPL slag viscosity model (section 5.2.2).
- The influence of allowing CaS precipitation (section 5.2.3).

5.2.1 The effect of the change in the rate of interfacing between Fluent and MTDATA.

The accuracy of the predicted desulphurization rate improves using a high MTDATA interface rate as illustrated in figure 73. However the required running time increases dramatically. In this present work, 2.5 hr of CFD running time was required to solve 1min of refining process time excluding the flow field creation time. In addition, each

MTDATA run required on average 20 minutes. A PC computer loaded with a Pentium-4 processor of speed 2.8 GHz and 512MB RAM was utilized.

The mass fraction ratio of the steel/slag phases at the cells at the steel/slag interface is not a constant. This mass fraction varies during the process time due to the gas stirring resulting in a fluctuation of the steel path surface. Also the species concentration in the steel varies due to the refinement which is occurring during the process time. Therefore, the predicted species mass exchange rate between the steel and the slag phase cannot be simply estimated by a single value. Figure 84 illustrates the variation in the steel/slag mass fraction at the steel/slag interface during the process time. Following the highlighted zone in the figure would give a sense of the mass fraction ratio variation during the process time.

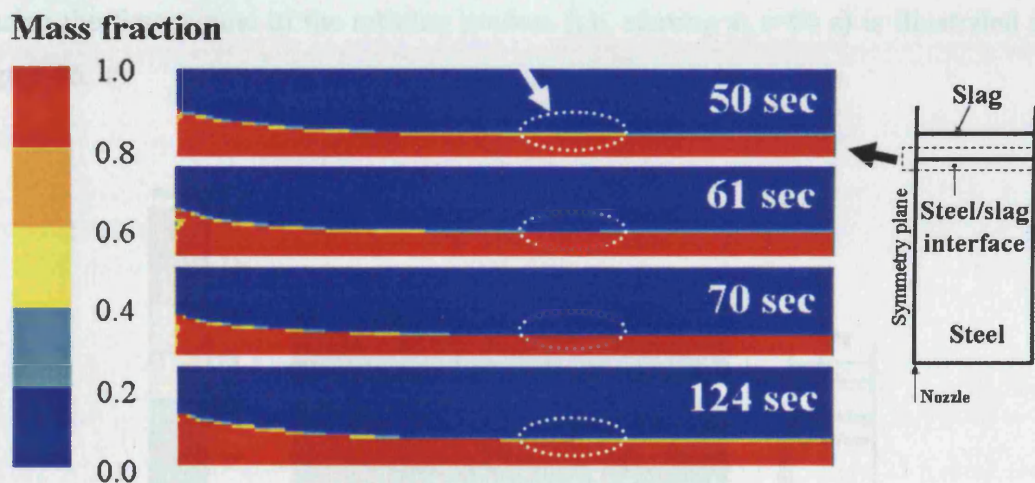


Figure-84. Mapping of the steel/slag mass fraction at the interface, the highlighted region illustrates the variation which is occurring during the gas stirring process.

As explained earlier in chapter 3, the mass fraction, temperature, and pressure for each single cell in the domain, and for each phase and species of concern is being saved in Fluent in a text file. This file then is read by MTDATA to run the thermodynamic analysis only at the cells containing a sufficient mass mixture which are located at the steel/slag interface. Then MTDATA saves the predicted exchange species mass of interest (Al, O, and S) for the cell where caused MTDATA has been executed and gives a zero value to the rest of the domain cells. This result from MTDATA is then used by Fluent to calculate the exchange mass transfer rate. Due to

the expected variation of the steel/slag mass fraction at the steel/slag interface, and also the variation in the species mass distribution in the molten steel, it is essential to update frequently the predicted mass exchange by MTDATA i.e. to have as high as interface rate as can be afforded given the analysis time.

The predicted species mass transfer rate at the steel/slag interface was monitored to examine the influence of the MTDATA interface rate on the predicted desulphurization rate. First the species mass transfer rate predicted by Fluent at the steel/slag interface was monitored during the first minute of the refining process using a single interface with MTDATA at the beginning of the refining process. Then the species mass transfer rate predicted by Fluent at the steel/slag interface was monitored using an updated by MTDATA every 20 sec. The initial prediction by MTDATA is shown in figure 85-a. The variation of the calculated mass transfer rate by Fluent during the first minute of the refining process (i.e. starting at $t=60$ s) is illustrated in figure 86.

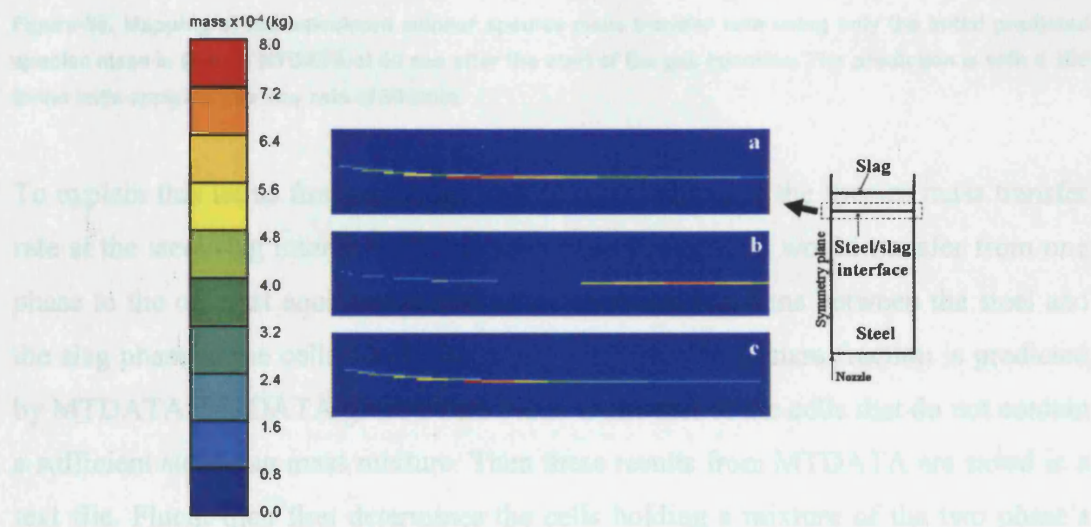


Figure-85. Mapping of the predicted removed sulphur mass in (kg) at the steel/slag interface. a) Initial prediction by MTDATA at 50 sec after the start of the gas injection, b) Second estimation at 70 sec after the start of the gas injection, c) Third estimation at 90 sec after the start of the gas injection. The prediction is with a 100 tonne ladle applying a gas flow rate of 80 l/min.

In figure 86 the number of cells loaded with a mass transfer rate at the steel/slag interface reduces during the process time. This can be understood due to, firstly, the variation in steel/slag mass fraction at the interface illustrated in figure 84, and

secondly, due to the changes of the species mass fraction distribution which will be clarified later

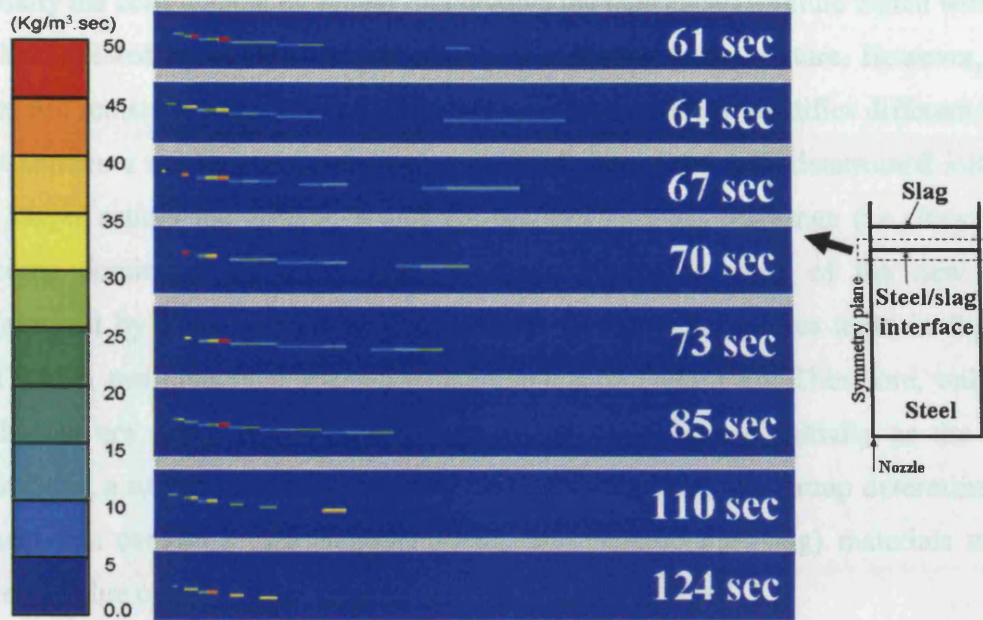
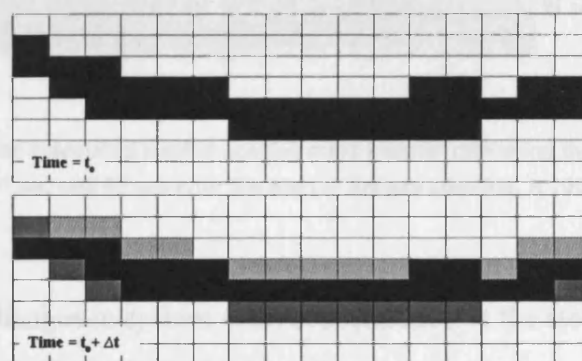


Figure-86. Mapping of the calculated sulphur species mass transfer rate using only the initial predicted species mass in (kg) by MTDATA at 50 sec after the start of the gas injection. The prediction is with a 100 tonne ladle applying gas flow rate of 80 l/min.

To explain this let us first understand how Fluent calculates the species mass transfer rate at the steel/slag interface. The species mass in (kg) that would transfer from one phase to the other at equilibrium due to the chemical reactions between the steel and the slag phase at the cells containing a sufficient steel/slag mass fraction is predicted by MTDATA. MTDATA gives a zero value to the rest of the cells that do not contain a sufficient steel/slag mass mixture. Then these results from MTDATA are saved in a text file. Fluent then first determines the cells holding a mixture of the two phase's material (steel/slag) together to activate the species mass exchange between the two present phases (steel/slag). It then reads the text file holding the predicted species mass in (kg) for each single cell in the domain. Finally Fluent uses the species mass in (kg) from the saved text file, the steel velocity at the cell of interest, and the cell volume to calculate the species mass transfer rate in ($\text{kg}/(\text{m}^3\text{s})$) for each single cell in the domain. However, only the cells at the steel/slag interface containing a sufficient

steel/slag mass mixture as per MTDATA would have a positive mass transfer rate, and the rest would get a zero value.

Initially the cells located by Fluent that involve the (steel/slag) mixture match with the cells suggested by MTDATA that contain a sufficient mass mixture. However, this does not remain the case. Due to the steel circulation, Fluent identifies different cells that contain a mixture of (steel/slag) material. Some of the cells determined initially no longer satisfy the criteria to activate the species mass exchange (i.e. they have become dominated by either steel or slag). Therefore some of the new cells determined by Fluent would be given a zero value of the species mass in (kg) by MTDATA resulting in a zero mass transfer rate in ($\text{kg}/(\text{m}^3\text{s})$). Therefore, only the cells that are common between the groups of cells defined initially as the cells containing a sufficient mass mixture by MTDATA and the new group determined by Fluent that contain a mass mixture of the two phases (steel/slag) materials would given a value of the species mass transfer as sketched in figure 87.



- Cells initially contain a sufficient steel/slag mass mixture determine by MTDATA and given a non zero value of the predicted species mass in (kg), but they have become dominated by either steel or slag, therefore, it was not detected by Fluent to activate the species mass transfer mechanism.
- Cells contain a steel/slag mass mixture determine by Fluent to activate the species mass transfer mechanism, but it was given a zero value of the predicted species mass in (kg) by MTDATA.
- Cells which are identified by both Fluent and MTDATA as subject of analysis.
- Cells which are dominated by a single phase and given by MTDATA a zero value of the predicted species mass in (kg).

Figure-87. A sketch to demonstrate the influence of the dissimilarity between the cells defined by MTDATA as cells with a sufficient steel/slag mass mixture and the cells defined by Fluent to activate the species mass transfer mechanism.

This would result in a vanishing of the calculated mass transfer rate as illustrated in figure 86. Therefore, a frequent update (i.e. high interface rate) is essential to make sure that there are enough 'common' cells during the process time.

Based on the above discuss frequent update rate as low as few seconds by MTDATA is essential. The influence of the frequent update every 20 seconds on the calculated species mass transfer rate is illustrated in figure 88. The updated predicted species mass in (kg) at the steel/slag interface is given in figure 85.

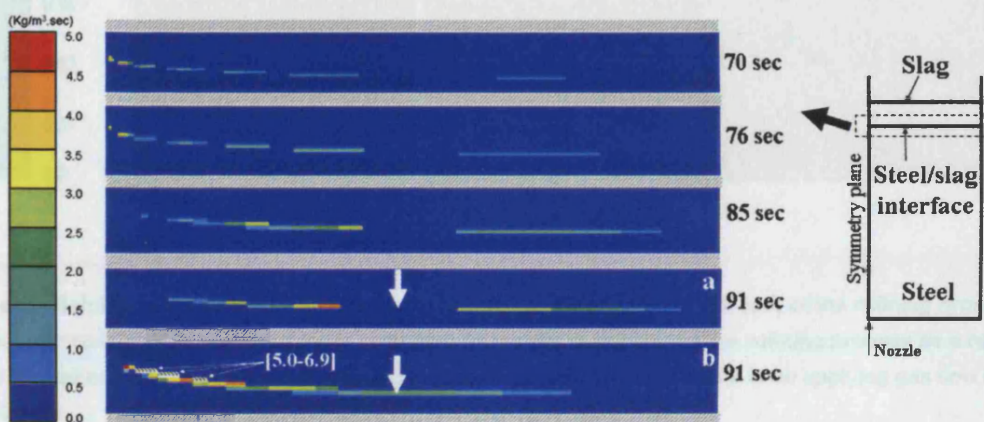


Figure-88. Mapping of the calculated sulphur species mass transfer rate using the predicted species mass in (kg) by MTDATA at 70 sec and 90 sec after the start of the gas injection. A 100 tonne ladle applying gas flow rate of 80 l/min.

Furthermore, the changes in species mass concentration at the steel/slag interface play a major role in the determination of the predicted species mass in (kg). During the gas stirring process the steel rises upward from the bottom side close to the axis line on through the plume zone to the steel/slag interface. Then it turns and moves towards the ladle side wall along the steel/slag interface before it turns back again to the bottom and so on. During this journey, the species mass fraction in the molten steel at the steel/slag interface changes due to the refining occurring at the interface and due to the mixing with the steel coming from the bottom. Figure 89 illustrates the variation in the sulphur concentration dissolved in steel due to the circulation occurring. From the figure can be seen the switch which is happening to the sulphur rich steel along the steel/slag interface that results in variation in the expected predicted species mass transfer rate along the steel/slag interface.

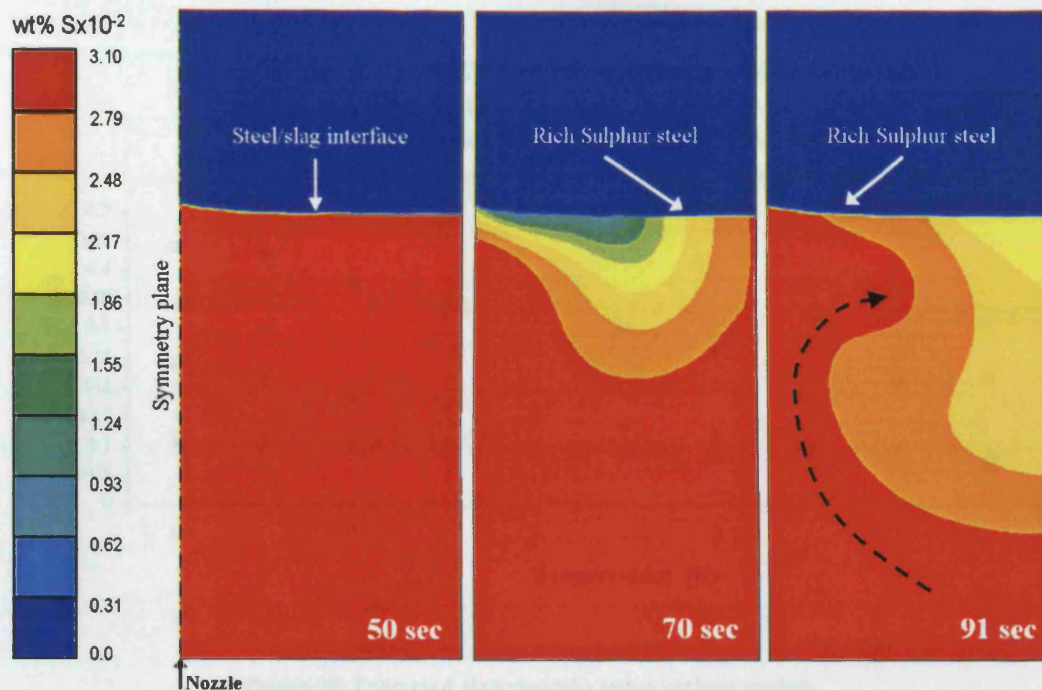


Figure-89. Sulphur mass concentration changes during the 40sec (50 sec -91 sec) of the refining process. The sulphur rich steel at the interface is switching from right to left during the refining process as a result of the over all circulation of the steel in the ladle vessel. (results for a 100 tonne ladle applying gas flow rate of 80 l/min).

5.2.2 The influence of the use of the NPL slag viscosity model

The NPL slag viscosity model was selected to replace the temperature dependence slag viscosity correlation given in table 9 as discussed in section 2.2.3 (iii). The comprehensive slag viscosity model proposed by KTH given in section 2.2.3 (ii) (a) was discarded due the copyright as discussed earlier. The KTH model although it is complex to employ would be the most suitable model from the list in section 2.2.3 (ii) for this present slag system. The evidence for this is as follows. Figure 90 shows the comparison between predictions using the KTH model [51] compared with the prediction from the NPL model here and the temperature dependence correlation given in table 9. The figure also shows experimental results [51].

The slag viscosity predicted using the NPL model agrees much more closely with the experimental measurement than the results predicted using the temperature dependence correlation given in table 9 (see figure 90).

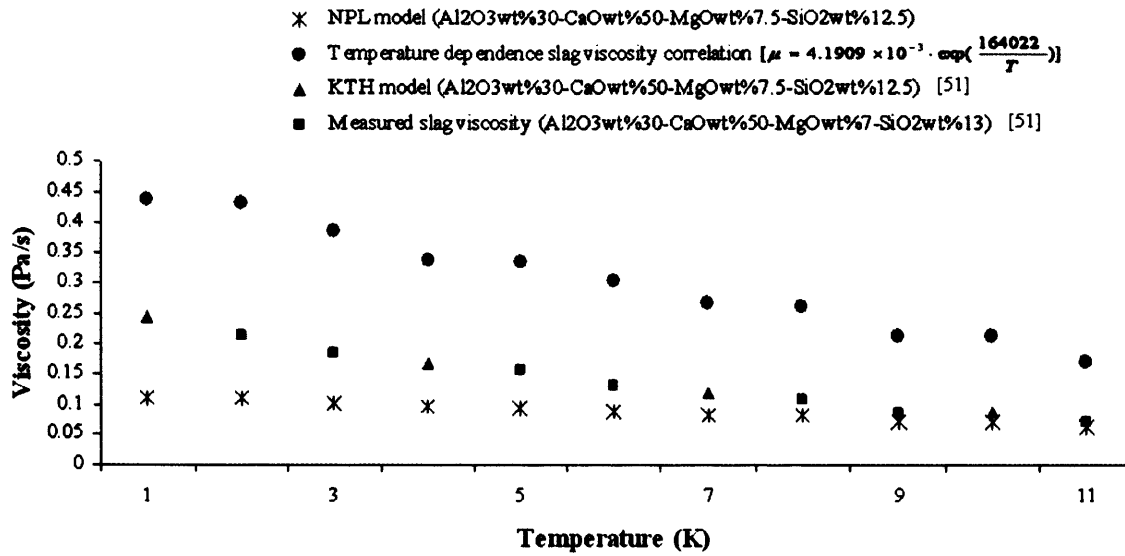


Figure 90. Estimated slag viscosity using various models.

The NPL and KTH models have additional parameters (in comparison with the temperature dependence correlation) that account for the influence of the slag structure changes and not only the temperature influence. The KTH model, in fact, shows extraordinarily good matching with the experimental measurement for this particular slag system (Al₂O₃ wt%30-CaO wt%50-MgO wt%7.5-SiO₂ wt%12.5) [51]. At high temperature both the NPL and the KTH model show a good agreement with the measurement. On the other hand, the NPL model is relatively insensitive to temperature.

Figure 74 illustrates the influence on the desulphurization over time of the predicted slag viscosity values due to the NPL model and also due to the temperature correlation in table (9). The influence of the ladle slag viscosity was examined by Jonsson [51] at 120l/min gas flow rate. The slag viscosity was found to be a significant influence on the secondary steelmaking refining process. An enlargement of the mixing zone at the steel/slag interface probably occurs due to the reduction of the slag viscosity. This would increase the overall desulphurization rate. Also, the influence of the applied gas flow rate was examined as shown in the figure.

5.2.3 The influence of allowing Ca^{++} mobility and CaS precipitation

Initially, the precipitated CaS is higher at the bubble slag zone (figure 91 (1min)) due to the high sulphur concentration as in agreement with experiment [112]. However, the concentrations in that region rapidly homogenize (figure 91 (5, 10 min)). This could be due to the fact that the precipitated CaS, in these calculations, has been defined as a species of the slag system, and therefore can move quite rapidly. It would be desirable to treat it as a fourth phase (after steel, slag, and gas) but when this approach was attempted the solution became unstable. This requires more attention.

Looking to the data in table 7 (page 42), the significant influence of the presence of the network forming SiO_2 on the restriction of the Ca^{++} mobility is noticeable. In this present work the influence of SiO_2 present in the slag was neglected due to the lack of information about the cation diffusivity in slag. Therefore, a high value of the Ca^{++} diffusivity rate ($19 \times 10^{-6} \text{ cm}^2/\text{s}$) was used in this present work.

Generally the sulphide precipitation is expected to affect the desulphurization rate. In contrast to expectation, comparing the two curves in figure 75 (page 94) shows a slight increase in the desulphurization rate during the precipitation of CaS. There are three possible reasons for this:

- The apparently high homogenization rate of the precipitated CaS and its movement from the steel/slag interface which would enhance the desulphurization process.
- The rapid homogenization of Ca^{++} over the slag domain results in almost a zero gradient of the CaO phase. This reduces the possibility of the local reduction of the CaO phase mass concentration at the steel/slag interface which would lead to a local reduction of the desulphurization rate.
- Finally, due to the formation of the precipitated CaS phase, the active dissolved sulphur in slag was reduced locally in comparison with the case where the CaS precipitation was not allowed over the same time during the

refining process, which increases the local sulphur capacity. This results in the slight increase of the desulphurization rate shown in figure 75.

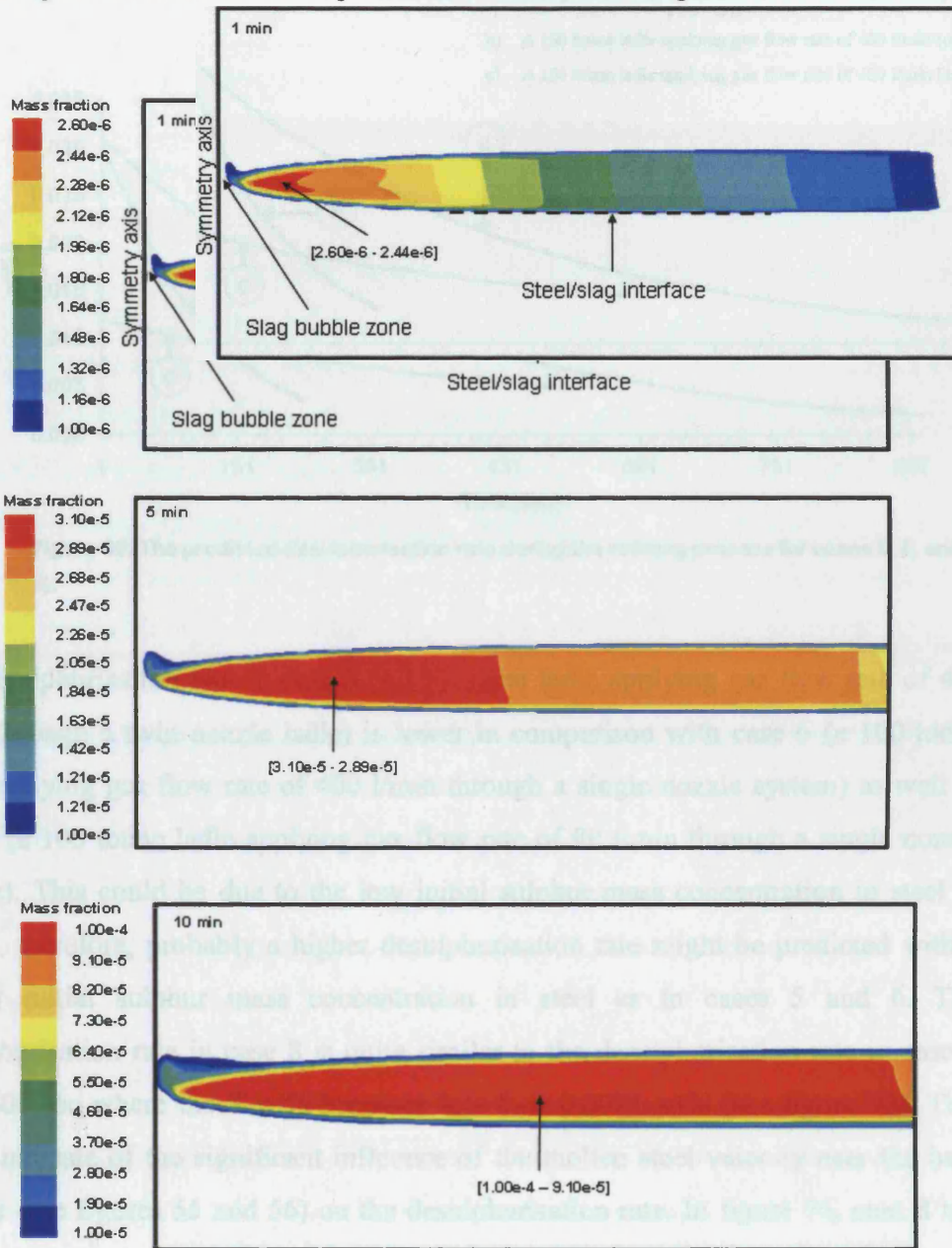


Figure-91. The precipitated CaS mass fraction in slag during the refining.

5.2.4 The influence of nozzle configuration on the desulphurisation rate

With respect to the gas flow rate, a rough comparison between the two cases 6 and 8 gives an indication of the influence of the nozzle configuration on the

desulphurisation rate. Figure 92 illustrates the predicted desulphurisation rate in cases 5, 6, and 8.

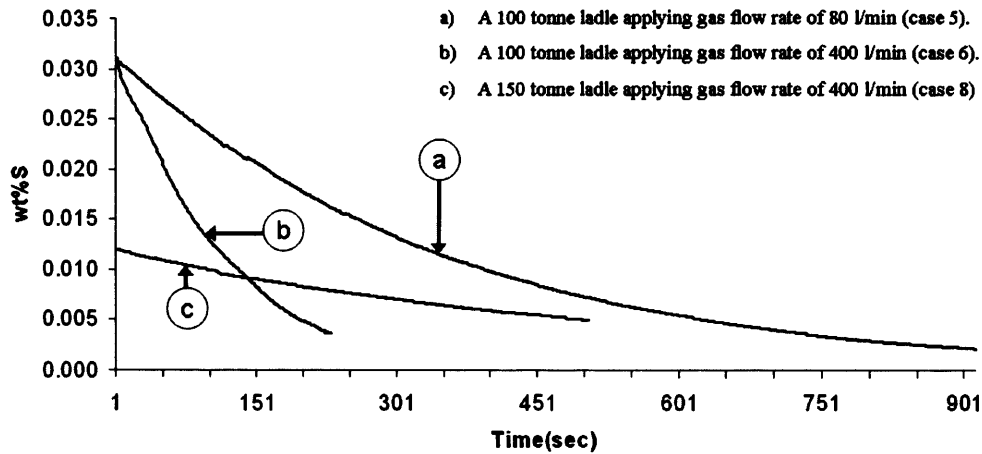


Figure-92. The predicted desulphurisation rate during the refining process for cases 5, 6, and 8).

The desulphurisation rate in case 8 (a 150 tonne ladle applying gas flow rate of 400 l/min through a twin nozzle ladle) is lower in comparison with case 6 (a 100 tonne ladle applying gas flow rate of 400 l/min through a single nozzle system) as well as case 5 (a 100 tonne ladle applying gas flow rate of 80 l/min through a single nozzle system). This could be due to the low initial sulphur mass concentration in steel in case 8, therefore, probably a higher desulphurisation rate might be predicted with a similar initial sulphur mass concentration in steel as in cases 5 and 6. The desulphurisation rate in case 8 is quite similar to the desulphurisation rate in case 5 after 600 sec where the S wt% becomes less than 0.0075 wt% (see figure 92). This might indicate of the significant influence of the molten steel velocity near the bath surface (see figures 55 and 56) on the desulphurisation rate. In figure 76, case 8 has simulated only about 500 sec of the total process time. The time in industry would be about 1800 sec. It is important that in industry this process time is being used to achieve a low level of hydrogen (less than 2 ppm) as well as sulphur.

6. Conclusions

In this present work a demonstration of the link between CFD and a thermodynamic model to simulate the refining of steel in a ladle, in particular desulphurisation, was described. The predicted desulphurisation rate is in good agreement with published literature results. A successful coupling between the CFD prediction and the thermodynamic analysis has been achieved. It will be possible to extend the present model to study other types of steelmaking processes involving slag-metal reactions.

The validity of the model has been tested by comparison with experimental results. The present model predicted steel near-surface horizontal velocities in good agreement with experimental measurement. In general the prediction of the near-surface velocities was improved using the top gas occupied zone approach in comparison with the classical top wall/symmetry surface linked with a gas escape mechanism.

In this present work the capability of the model to predict the desulphurisation rate under different operational conditions was demonstrated. A successful implementation of the NPL slag viscosity model was achieved. This relates the slag viscosity to temperature and composition, both of which change continuously during the process. Therefore, it is possible to study the influence of the slag system composition variation during the refining process.

In this present work, the influence on desulphurisation rate of allowing the precipitation of the CaS phase in the slag has been investigated. Successful implementation of the Nilsson slag capacity model was achieved.

One of the advantages of the MTDATA package is the ease of switching to analyse a different slag oxide system; therefore, it was possible to simulate a real plant case using a different slag system.

In this present work some features are:

- Addition of a vacuum zone on the top of the slag layer, to avoid restricted heat losses from the top surface, and provide more freedom for the slag phase motion.
- Advanced thermodynamic prediction with minimal assumptions using the MTDATA thermodynamic package from National Physical Laboratory (NPL), using three different databases.
- The model can be upgraded easily to study more phenomena in steelmaking processes involving slag-metal reactions e.g. decarburisation at the steel/slag interface, due to the use of a separate thermodynamic package.

7. Future works

- Further work on nitrogen removal during the ladle degassing process is required. Hydrogen removal can be implemented in this present simulation model using a simple mass transfer mechanism between the gas phase bubbles and the dissolved hydrogen species. The method used to predict the bubble size plays a major role in this refining process. The argon bubble surface area is the domain where the hydrogen gas formation occurs. Therefore, great care should be taken in the selection of the suitable bubble size prediction method.
- It is possible to upgrade the present model to model different slag system. Therefore, it is possible to study the influence of the slag system composition variation during the refining process.
- It is possible to investigate the influence of FeO, MnO and P₂O₅ oxides on the desulphurisation rate.
- Further investigation of allowing Ca⁺⁺ mobility and CaS precipitation in slag using a proper cation diffusivity rate. Also it would be desirable to treat CaS as a fourth phase (after steel, slag, and gas).
- It is possible to investigate and utilize the capability of the tank vacuum degassing to achieve decarburisation, a process that is usually achieved using the circulation degassing process (RH).

8. References

- [1] D. Mazumdar and R. I. L. Guthrie, "The physical and mathematical modeling of gas stirring ladle systems," *ISIJ International*, vol. 35, (1), 1995, pp. 1-20.
- [2] L. Jonsson, D. Sichen, and P. Jönsson, "A new approach to model sulphur refining in a gas-stirring ladle a coupled CFD and thermodynamic model," *ISIJ International*, vol. 38, (3), 1998, pp. 260-267.
- [3] O. J. Ilegbusi and J. Szekely, "The modeling of gas-bubble driven circulations systems," *ISIJ International*, vol. 30, (9), 1990, pp. 731-739.
- [4] H. Turkoglu and B. Farouk, "Numerical computations of fluid flow and heat transfer in gas injected iron baths," *ISIJ International*, vol. 30, (11), 1990, pp. 961-970.
- [5] S. V. Komarov and M. Sano, "Bubble behavior and heat transfer in preheated gas injection into liquid bath," *ISIJ International*, vol. 38, (10), 1998, pp. 1045-1052.
- [6] R. Clift, J. R. Grace, and M. E. Weber, "Formation and breakup of fluid particles: Breakup of drops and bubbles," *Bubbles, drops, and particles*. New York: Dover Publications, inc., 2005, pp. 321-351. (First published by Academic Press, Inc., New York, 1978).
- [7] A. Ghosh, "Flow fundamentals," *Secondary steelmaking, principles and applications*: CRS Press, 2001, pp. 47-78.
- [8] Y. Xie, S. Orsten, and F. Oeters, "Behaviour of bubbles at gas blowing into liquid wood's metal," *ISIJ International*, vol. 32, (1), 1992, pp. 66-75.

- [9] D. Mazumdar, H. Nakajima, and R. I. L. Guthrie, *Metallurgical & Materials Transactions (B)*, vol. 19B, 1988, pp. 507-511.
- [10] M. Iguchi, O. J. Ilegbusi, H. Ueda, T. Kuranaga, and Z. Morita, *Metallurgical & Materials Transactions (B)*, vol. 26B, 1996, pp. 37-41.
- [11] O. J. Ilegbusi, M. Iguchi, K. Nakajima, M. Sano, and M. Sakamoto, "Modeling mean flow and turbulence characteristics in gas-agitated bath with top layer," *Metallurgical & Materials Transactions (B)*, vol. 29B, 1998, pp. 211-222.
- [12] K. Mori, M. Sano, and Sato, "Size of bubbles formed at single nozzle immersed in molten iron," *T. ISIJ*, 1979, pp. 553-561.
- [13] L. Wang, H. Lee, and P. Hayes, "A new approach to molten steel refining using fine gas bubbles," *ISIJ International*, vol. 36, (1), 1996, pp. 17-24.
- [14] F. Oeters, *Metallurgy of steelmaking*. Woodhead Publishing, Cambridge, England, 1994.
- [15] E. Turkdogan, "Rate phenomena: estimation of bubble size for uniformly dispersed bubbles in the steel bath," *Fundamentals of steelmaking: The Institute of Materials*, 1996, pp. 74-81.
- [16] E. T. Turkdogan, "Steel refining in the ladle: mixing time," *Fundamentals of Steelmaking: The Institute of Materials*, 1996, pp. 251-252.
- [17] J. W. Han, S. H. Heo, D. H. Kam, B. D. You, J. J. Pak, and H. S. Song, "Transient fluid flow phenomena in a gas stirred liquid bath with top oil layer-approach by numerical simulation and water model experiments," *ISIJ International*, vol. 41, (10), 2001, pp. 1165-1173.
- [18] K. Krishnakumar, N. B. Ballal, P. K. Sinha, M. K. Sardar, and K. N. Jha, "Water model experiments on mixing phenomena in a VOD ladle," *ISIJ International*, vol. 39, (5), 1999, pp. 419-425.
- [19] W. E. Ranz and W. R. Marshall, *Chem. Eng. Prog.*, vol. 48, (3), 1951, pp. 141.

- [20] T. Imai, T. Murayama, and Y. Ono, "The estimation of convective heat transfer coefficients between a spherical particle and fluid at lower Reynolds number," *ISIJ International*, vol. 35, (12), 1995, pp. 1438-1443.
- [21] S. Taniguchi, M. Ohmi, and S. Ishiura, *Trans. Iron Steel Inst. Jpn.*, vol. 23, 1983, pp. 572.
- [22] S. Taniguchi, M. Ohmi, S. Ishiura, and S. Yamauchi, *Trans. Iron Steel Inst. Jpn.*, vol. 23, 1983, pp. 565.
- [23] S. Whitaker, "Forced convection heat transfer correlations for flow in pipes, past flat plates, single cylinders, single spheres, and for flow in packed bed and tube bundles," *AIChE Journal*, vol. 18, (2), 1972, pp. 361-371.
- [24] J. L. Xia and T. Ahokainen, "Transient flow and heat transfer in a steelmaking ladle during the holding period," *Metallurgical and Materials Transactions B*, vol. 32B, 2001, pp. 733-741.
- [25] P. R. Austin, J. M. Camplin, J. Herbertson, and L. J. Taggart, "Mathematical modelling of thermal stratification and drainage of steel ladles," *ISIJ International*, vol. 32, (2), 1992, pp. 196-202.
- [26] L. Jonsson and P. Jönsson, "Modeling of fluid flow conditions around the slag/metal interface in a gas-stirred ladle," *ISIJ International*, vol. 36, (9), 1996, pp. 1127-1134.
- [27] C. Cicutti, M. Valdez, J. Petroni, R. Ares, R. Donayo, and A. Gomez, "Slag optimization practices during the production of low carbon aluminum killed steels," presented at Sixth International Conference on Clean Steel, Balatonfüred, Hungary, 2002.
- [28] P. Herasymenko and G. E. Speight, "Ionic theory of slag-metal equilibria," *Journal of the Iron and Steel Institute*, (November), 1950, pp. 169-183.
- [29] N. Sano, W.-K. Lu, P. V. Riboud, and M. Maeda, "Thermodynamics of slags," *Advanced physical chemistry for process metallurgy*. San Diego, California, USA: Academic Press, 1997, pp. 45-86.

- [30] T. A. Engh, "Thermodynamics and transport properties," *Principles of metal refining*: Oxford University Press, 1992, pp. 39-125.
- [31] V. D. Eisenhuttenleute, "The structure of slags containing silica and/or other complex-forming constituents," *Slag Atlas*, K. C. Mills, Ed.: Verlag Stahleisen GmbH, 1995, pp. 5-6.
- [32] A. Ghosh, "Thermodynamics fundamentals," *Secondary steelmaking, principles and applications*: CRS Press, 2001, pp. 9 - 46.
- [33] E. Turkdogan, "Physicochemical properties of molten slags: slag basicity," *Fundamentals of steelmaking*: The Institute of Materials, 1996, pp. 138-179.
- [34] V. D. Eisenhuttenleute, "Basicity," *Slag atlas*, K. C. Mills, Ed.: Verlag Stahleisen GmbH, 1995, pp. 10.
- [35] E. T. Turkdogan, "Slags and fluxes for ferrous ladle metallurgy," *Ironmaking and Steelmaking*, vol. 12, (2), 1985, pp. 64-78.
- [36] "Synthetic slags for steelmaking," Shieldalloy Metallurgical Cooperation 1995.
- [37] K. P. Abraham and F. D. Richardson, "Sulphide capacities of silicate melts," *Journal of the Iron and Steel Institute*, vol. 196, (November), 1960, pp. 313-317.
- [38] F. D. Richardson and C. J. B. Fincham, "Sulphur in silicate and aluminate slags," *Journal of the Iron and Steel Institute*, vol. 178, (September), 1954, pp. 4-15.
- [39] F. D. Richardson, "Slags and mattes," *Physical chemistry of melts in metallurgy*, vol. 2: Academic Press London and New York, 1974, pp. 291-327.
- [40] E. T. Turkdogan, "Physicochemical properties of molten slags: gas solubilities in slags," *Fundamentals of steelmaking*: The Institute of Materials, 1996, pp. 138-179.

- [41] E. T. Turkdogan, "Steel refining in the ladle: desulphurisation," *Fundamentals of Steelmaking*: The Institute of Materials, 1996, pp. 269-276.
- [42] E. T. Turkdogan, "Equilibrium data on liquid steel-slag reactions: reduction of sulphur," *Fundamentals of Steelmaking*: The Institute of Materials, 1996, pp. 189-192.
- [43] M. Andersson, M. Hallberg, L. Jonsson, and P. Jonsson, "Slag-metal reactions during ladle treatment with focus on desulphurisation," *Ironmaking and Steelmaking*, vol. 29, (3), 2002, pp. 224-232.
- [44] R. A. Sharma and F. D. Richardson, "Activities in lime-alumina melts," *Journal of the Iron and Steel Institute*, vol. 198, (August), 1961, pp. 386-390.
- [45] E. T. Turkdogan, "Thermodynamic activity," *Fundamentals of steelmaking*: The Institute of Materials, 1996, pp. 13-19.
- [46] M. Nzotta, M. Andersson, P. Jönsson, and S. Seetharaman, "A study on the sulphide capacities of steelmaking slags," *Scandinavian Journal of Metallurgy*, vol. 29, 2000, pp. 177-184.
- [47] T. Sjoqvist, S. Jung, P. Jonsson, and M. Andreasson, "Influence of calcium carbide slag additions on inclusion characteristics in steel," *Ironmaking and Steelmaking*, vol. 27, (5), 2000, pp. 373-380.
- [48] M. Nzotta, D. Sichen, and S. Seetharaman, "Sulphide capacities in some multi component slag systems," *ISIJ International*, vol. 38, (11), 1998, pp. 1170-1179.
- [49] M. M. Nzotta, M. Andreasson, P. Jönsson, and S. Seetharaman, "A study on the sulphide capacities of steelmaking slags," *Scandinavian Journal of Metallurgy*, vol. 29, 2000, pp. 177-184.
- [50] R. Nilsson, D. Sichen, and S. Seetharaman, "Estimation of sulphide capacities of multi-component silicate melts," *Scandinavian Journal of Metallurgy*, vol. 25, (3), 1996, pp. 128-134.

- [51] P. G. Jönsson, L. Jonsson, and D. Sichen, "Viscosities of LF slags and their impact on ladle refining," *ISIJ International*, vol. 37, (5), 1997, pp. 484-491.
- [52] E. T. Turkdogan, "Physicochemical properties of molten slags: surface tension," *Fundamentals of steelmaking*: The Institute of Materials, 1996, pp. 138-179.
- [53] F. D. Richardson, "Interfacial phenomena," *Physical chemistry of melts in metallurgy*, vol. 2: Academic Press London and New York, 1974.
- [54] E. T. Turkdogan, "Thermodynamic properties," *Physicochemical properties of molten slags and glasses*: The Metals Society, London, 1983.
- [55] D. Sichen, J. Bygdén, and S. Seetharaman, "A model for estimation of viscosities of complex metallic and ionic melts," *Metallurgical & Materials Transactions B*, vol. 25B, 1994, pp. 519-525.
- [56] Y. A. Çengel and M. A. Boles, "Chemical and phase equilibrium: Phase equilibrium," *Thermodynamics: An engineering approach*: McGRAW-HILL, 1989, pp. 691-695.
- [57] M. M. Nzotta, D. Sichen, and S. Seetharaman, "A study of the sulfide capacities of iron-oxide containing slags," *Metallurgical and Materials Transactions B*, vol. 30, (5), 1999, pp. 909-920.
- [58] J. F. Elliott, M. Gleiser, and V. Ramakrishna, *Thermochemistry for steelmaking I, II*. Massachusetts: Addison-Wesley, 1963.
- [59] E. Turkdogan and P. M. Bills, "A critical review of viscosity of CaO-MgO-Al₂O₃-SiO₂ melts," *Am. Ceram. Soc. Bull.*, vol. 39, 1960, pp. 682.
- [60] P. Kozakevitch, *Physical chemistry of process metallurgy*. New York: Wiley Interscience, 1961.
- [61] T. Matsushita, M. Hayashi, and S. Seetharaman, "Thermochemical and thermophysical property measurements in slag systems," *Int. J. Materials and Product Technology*, vol. 22, (4), 2005, pp. 351-390.

- [62] K. C. Mills, L. Chapman, A. B. Fox, and S. Sridhar, "'Round robin' project on the estimation of slag viscosities," *Scandinavian Journal of Metallurgy*, vol. 30, 2001, pp. 396-403.
- [63] L. Zhang and S. Jahanshahi, "Review and modeling of viscosity of silicate melts: Part I. viscosity of binary and ternary silicate containing CaO, MgO, and MnO," *Metallurgical and Materials Transactions B*, vol. 29B, 1998, pp. 177-186.
- [64] S. Seetharaman, D. Sichen, and J. Zhang, *J Metals*, vol. 51, 1999, pp. 38-40.
- [65] K. C. Mills and S. Sridhar, "Viscosities of ironmaking and steelmaking slags," *Ironmaking and Steelmaking*, vol. 26, (4), 1999, pp. 262-268.
- [66] M. Temkin, "Mixtures of fused salts as ionic solutions," *Acta Phys. Chim. URSS*, vol. 20, 1945, pp. 411-420.
- [67] S. Seetharaman and D. Sichen, "Viscosities of high temperature systems - a modelling approach," *ISIJ International*, vol. 37, (2), 1997, pp. 109-118.
- [68] F. Ji, D. Sichen, and S. Seetharaman, "Viscosities of multicomponent silicate melts at high temperatures," *International Journal of Thermophysics*, vol. 20, (1), 1999, pp. 309-323.
- [69] K. C. Mills, "Influence of structure on the physico-chemical properties of slags," *ISIJ International*, vol. 33, (1), 1993, pp. 148-155.
- [70] L. Zhang and S. Jahanshahi, "Review and modeling of viscosity of silicate melts: Part II. viscosity of melts containing iron oxide in the CaO-MgO-MnO-FeO-Fe₂O₃-SiO₂ system," *Metallurgical and Materials Transactions B*, vol. 29B, 1998, pp. 187-195.
- [71] L. Zhang and S. Jahanshahi, "Modeling viscosity of alumina-containing silicate melts," *Scandinavian Journal of Metallurgy*, vol. 30, 2001, pp. 364-369.
- [72] J. Crank, "The diffusion equations," *The mathematics of diffusion*, second edition ed: Oxford Science Publications, 1975, pp. 1-10.

- [73] E. Turkdogan, "Rate phenomena: diffusion in ionic media (slags)," *Fundamentals of steelmaking*: The Institute of Materials, 1996, pp. 44.
- [74] M. D. Dolan and R. F. Johnston, "Multicomponent diffusion in molten slags," *Metallurgical & Materials Transactions (B)*, vol. 35B, 2004, pp. 675-684.
- [75] R. F. Johnston, R. A. Stark, and J. Taylor, "Diffusion in liquid slags," *Ironmaking and Steelmaking*, (4), 1974, pp. 220-227.
- [76] E. T. Turkdogan, "Rheological and transport properties: mass diffusivity and electrical conductivity," *Physicochemical properties of molten slags and glasses*: The Metals Society, London, 1983, pp. 28.
- [77] E. T. Turkdogan, "Reaction during steel solidification: subsurface blowhole formation," *Fundamentals of steelmaking*: The Institute of Materials, 1996, pp. 297-320.
- [78] E. T. Turkdogan, "Physicochemical properties of steel: solubility of hydrogen," *Fundamentals of steelmaking*: The Institute of Materials, 1996, pp. 96-97.
- [79] A. Ghosh, "Degassing and decarburization of liquid steel," *Secondary steelmaking, principles and applications*: CRS Press, 2001, pp. 147-186.
- [80] J. H. Walsh, J. Chipman, T. B. King, and N. J. Grant, "Hydrogen in steelmaking slags," *Journal of Metals, Transactions AIME*, (November), 1956, pp. 1568--76.
- [81] K. N. Jha, M. K. Sardar, N. N. Jha, and S. Chakraborty, "Hydrogen control during steel making for medium carbon wheels," *Scandinavian Journal of Metallurgy*, vol. 32, 2003, pp. 296-300.
- [82] L. Jonsson, "Mathematical modeling of selected ladle operations-Towards metallurgical process models based on fundamental equations," *PhD thesis, Department of Metallurgy*", Royal Institute of Technology, Stockholm, 1998, Sweden.

- [83] P. Jönsson and L. Jonsson, "The use of fundamental process models in studying ladle refining operations," *ISIJ International*, vol. 41, (11), 2001, pp. 1289-1302.
- [84] T. Kitamura, K. Miyamoto, R. Tsujino, S. Mizoguchi, and K. Kato, "Mathematical model for nitrogen desorption and decarburization reaction in vacuum degasser," *ISIJ International*, vol. 36, (4), 1996, pp. 395-401.
- [85] B. E. Launder and D. B. Spalding, "The numerical computation of turbulent flows," *Computer Methods in Applied Mechanics and Engineering*, vol. 3, 1974, pp. 269-289.
- [86] M.-Y. Zhu, T. Inomoto, I. Sawada, and T.-C. Hsiao, "Fluid flow and mixing phenomenon in the ladle stirred by argon through multi-tuyere," *ISIJ International*, vol. 35, (5), 1995, pp. 472-479.
- [87] H. Turkoglu and B. Farouk, "Mixing time and liquid circulation rate in steelmaking ladles with vertical gas injection," *ISIJ International*, vol. 31, (12), 1991, pp. 1371-1380.
- [88] M. Y. Zhu, I. Sawada, and M. Iguchi, "Physical characteristics of a horizontally injected gas jet and turbulent flow in metallurgical vessels," *ISIJ International*, vol. 38, (5), 1998, pp. 411-420.
- [89] L. Jonsson, C. E. Grip, A. Johansson, and P. Jönsson, "Three-phase (steel, slag, gas) modeling of the CAS-OB process," presented at Steelmaking conference, Chicago; IL, 1997.
- [90] M. A. T. Andersson, L. Jonsson, and P. Jönsson, "A Thermodynamic and kinetic model of reoxidation and desulphurisation in the ladle furnace," *ISIJ International*, vol. 40, (11), 2000, pp. 1080-1088.
- [91] M. A. T. Andersson, L. Jonsson, and P. Jönsson, "A model of reoxidation from the top of slag and the effect on sulphur refining during vacuum degassing," *Scandinavian Journal of Metallurgy*, vol. 32, 2003, pp. 123-136.
- [92] C. E. Grip and L. Jonsson, "Physical behaviour of slag in a 107-tonne ladle:

- production scale experiments and theoretical simulation," *Scandinavian Journal of Metallurgy*, vol. 32, 2003, pp. 113-122.
- [93] E. A. H. Castillejos, M. E. Salcudean, and J. K. Brimacombe, "Fluid flow and bath temperature destratification in gas-stirred ladles," *Metallurgical Transactions B (Process Metallurgy)*, vol. 20, (5), 1989, pp. 603-611.
- [94] J. L. Xia, T. Ahokainen, and L. Holappa, "Analysis of flow in a ladle with gas-stirred melt," *Scandinavian Journal of Metallurgy*, vol. 30, 2001, pp. 69-76.
- [95] W. M. Kays, M. E. Crawford, and B. Weigand, "Turbulent Prandtl number," *Convective heat and mass transfer*, Fourth edition ed: McGRAW-HILL, 2005, pp. 233-239.
- [96] W. M. Kays, "Turbulent Prandtl number-where are we?," *Transaction of the ASME*, vol. 116, 1994, pp. 284-295.
- [97] B. Weigand, J. R. Ferguson, and M. E. Crawford, "An extended Keys and Crawford turbulent Prandtl number model," *Int. J. Heat Mass Transfer*, vol. 40, (17), 1997, pp. 4191-4196.
- [98] J. T. Kuo and G. B. Wallis, "Flow of bubbles through nozzles," *Int. J. Multiphase Flow*, vol. 14, (5), 1988, pp. 547-564.
- [99] L. Schiller and Z. Naumann, "A drag coefficient correlation," *V. D. I. Zeitung*, vol. 77, 1935, pp. 318-320.
- [100] S. A. Morsi and A. J. Alexander, "An investigation of particle trajectories in two-phase flow systems," *J. Fluid Mech.*, vol. 55, (2), 1972, pp. 193-208.
- [101] R. Clift, J. R. Grace, and M. E. Weber, "Spheres at higher Reynolds number," *Bubbles, drops, and particles*. Mineola, New York: Dover publications, inc., 2005, pp. 97-137. (First published by Academic Press, Inc., New York, 1978).
- [102] Y. Kawai and Y. Shiraishi, "Handbook of physico-chemical properties at high temperatures," The Iron and Steel Institute of Japan, 1988, pp. 2.

- [103] E. T. Turkdogan, "Thermal conductivity," *Fundamentals of steelmaking*: The Institute of Materials, 1996, pp. 178.
- [104] D. Mazumdar, H. B. Kim, and R. I. L. Guthrie, "Modelling criteria for flow simulation in gas stirred ladles: experimental study," *Ironmaking and Steelmaking*, vol. 27, (4), 2000, pp. 302-309.
- [105] L. Wang, H.-G. Lee, and P. Hayes, "A new approach to molten steel refining using fine gas bubbles," *ISIJ International*, vol. 36, (1), 1996, pp. 17-24.
- [106] K. Ogawa and T. Onoue, "Mixing and mass transfer in ladle refining process," *ISIJ International*, vol. 29, (2), 1989, pp. 148-153.
- [107] N. El-Kaddah, D. G. C. Robertson, S. T. Johansen, and V. R. Voller, "Fluid flow phenomena in metals processing," The Minerals, Metals & Materials Society, 1999, pp. 279.
- [108] A. Jauhiainen, L. Jonsson, and D.-Y. Sheng, "Modeling of alloy mixing into steel," *Scandinavian Journal of Metallurgy*, vol. 30, 2001, pp. 242-253.
- [109] J. F. Domgin, P. Gardin, and M. Brunet, "Experimental and numerical investigation of gas stirred ladles," presented at Second International Conference on CFD in the Minerals and Process Industries, CSIRO, Melbourne, Australia, 1999.
- [110] W. E. Ranz and W. R. Marshall, *Chem. Eng. Prog.*, vol. 48, (3), 1952, pp. 141-146.
- [111] T. C. Hsiao, T. Lehner, and B. Kjellberg, "Fluid flow in ladles - Experimental results," *Scandinavian Journal of Metallurgy*, vol. 9, (3), 1980, pp. 105-110.
- [112] J. Szekely, G. Carlsson, and L. Helle, "Injection practice in the secondary metallurgy of steel," *Ladle metallurgy*. New York: Springer-Verlag, 1989, pp. 118.
- [113] K. Krishnapisharody and G. A. Irons, "Modeling of slag eye formation over a metal bath due to gas bubbling," *Metallurgical & Materials Transactions B*, vol. 37B, 2006, pp. 763-772.

-
- [114] R. I. L. Guthrie, "Physical and mathematical models for ladle metallurgy operations," presented at Mathematical modelling of materials processing operations, Palm Springs, California, USA, 1987.
- [115] W. M. Kays and M. E. Crawford, *Convective heat and mass transfer*, 3rd edition ed. New York: McGRAW-HILL, 1993.

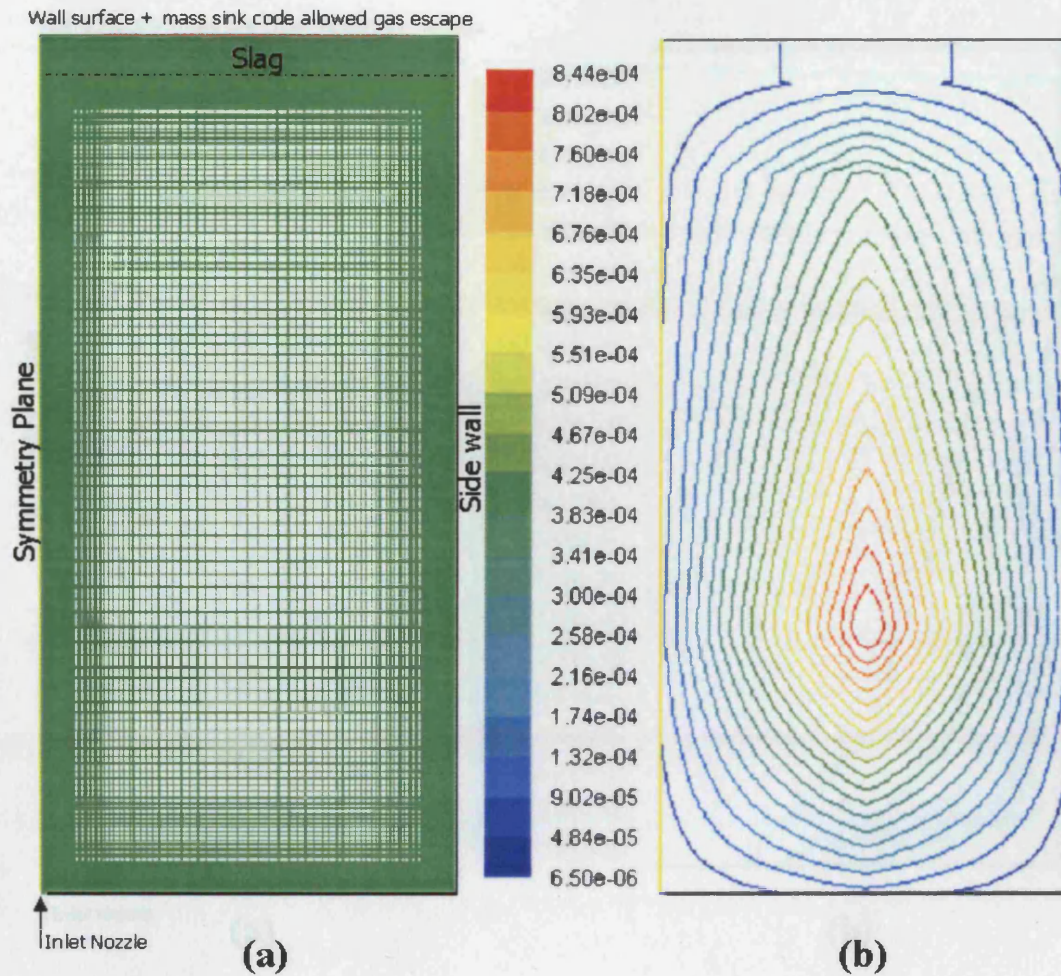


Figure-1. (a) Quadrilateral cell grid with 106600 cells, (b) cell volume contours (m^3). This grid was rejected due to the high number of cells causing high computational running time. Fine cells at the bottom and side wall can be avoided using the Enhanced Wall Treatment Fluent function. Also, the computational running time of the thermodynamics package would be very long due to the high number of cells at the steel/slag interface zone.

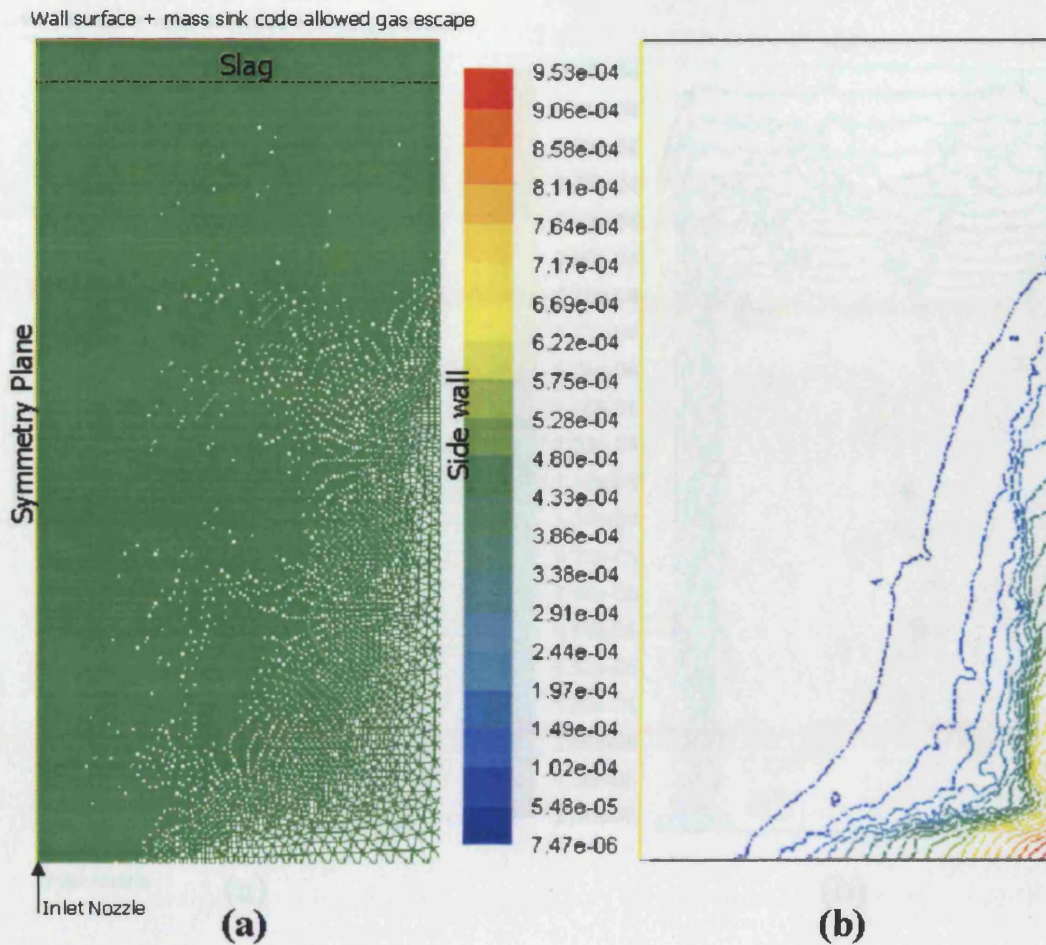


Figure-2 (a) Triangular cell grid with 95068 cells, (b) cell volume contours (m^3). With this type of grid cell, the solution of the multiphase system collapsed more rapidly than with the quadrilateral cell kind. This could not be clearly justified. Also, none of the models reported in the literature listed in this report used a triangular cell to build the grid. Additionally, for such a simple ladle system geometry, more cells were required to build the grid using a triangular cell than with a quadrilateral cell of a similar average size.

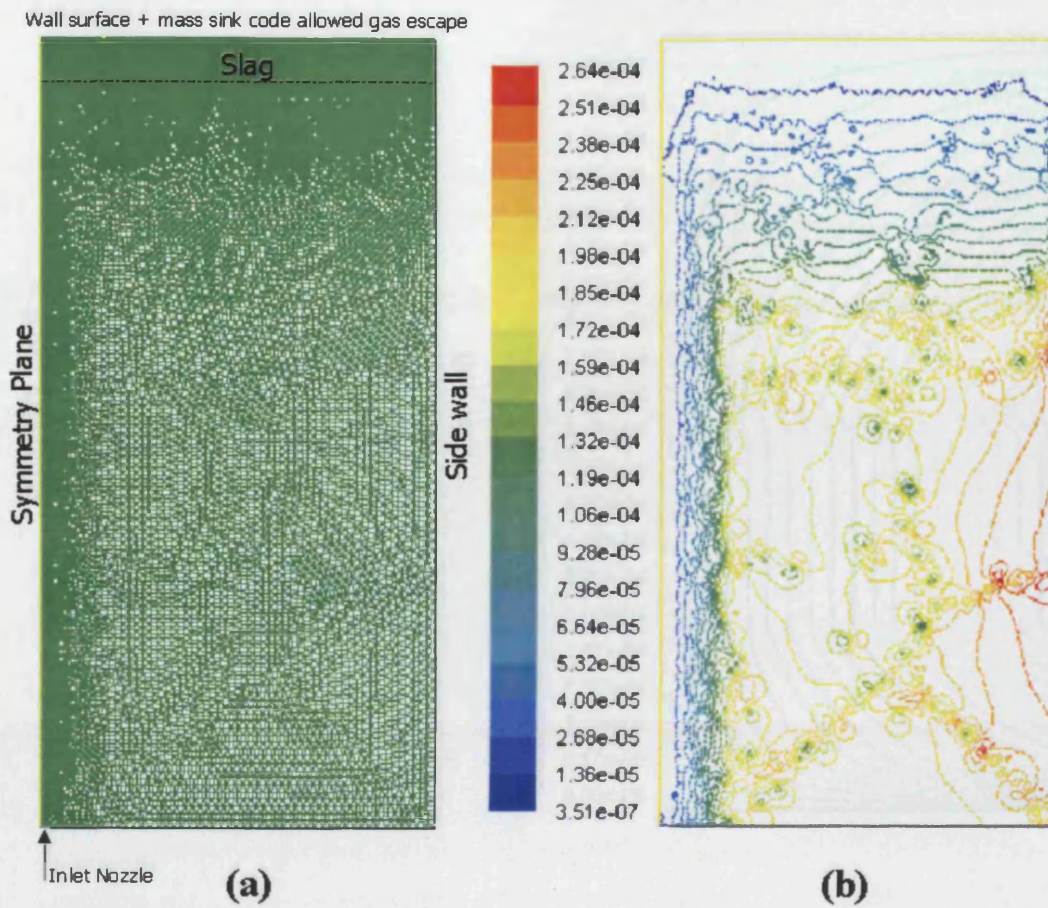


Figure-3. (a) Triangular cell grid with 38665 cells, fewer than in figure (2), (b) cell volume contours (m³). The solution for the multiphase system still collapsed more rapidly than for the quadrilateral cell kind.

and data was not
be needed using the standard VOF treatment. Also, the
computational running time of the thermodynamic package would be very
long due to the high number of cells at the deforming interface zone.

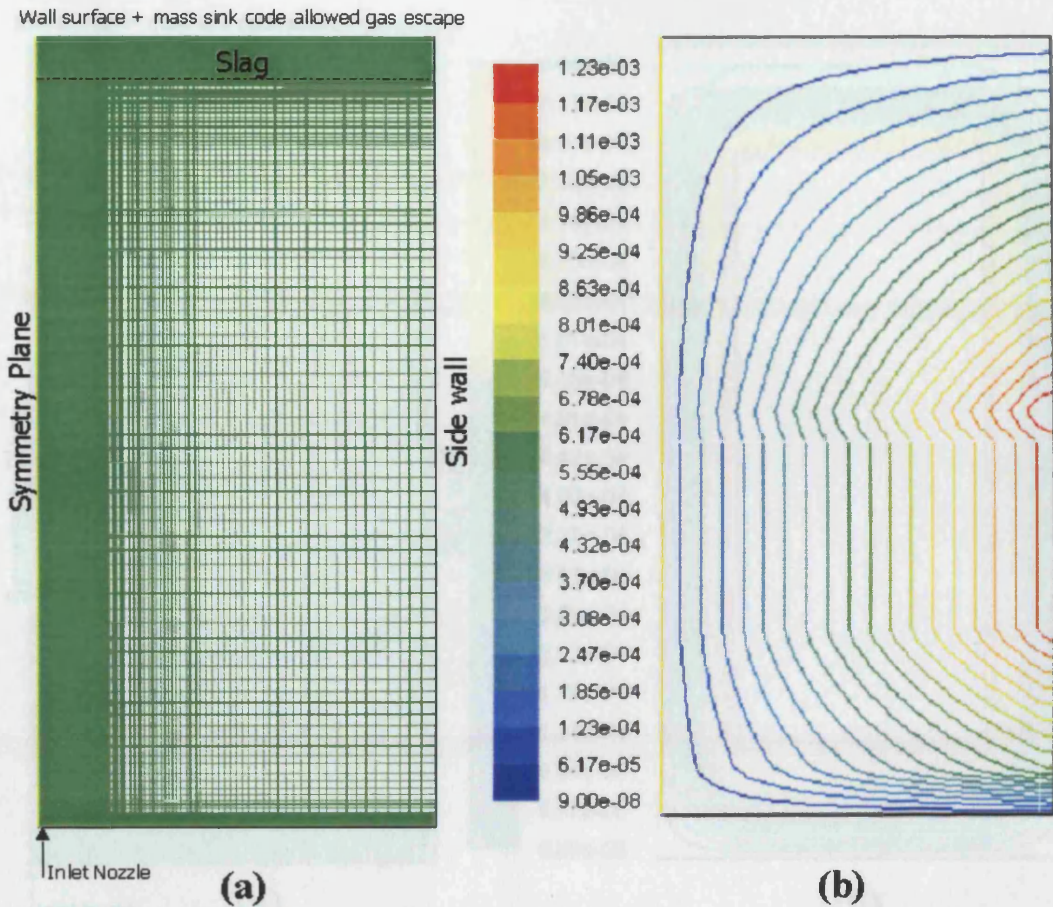


Figure-4. (a) Quadrilateral cell grid with 25500 cells, (b) cell volume contours (m^3). This grid was rejected due to the high number of cells causing high computational running time. Fine cells at the bottom and side wall can be avoided using the Enhanced Wall Treatment Fluent function. Also, the computational running time of the thermodynamics package would be very long due to the high number of cells at the steel/slag interface zone.

Wall surface + mass sink code allowed gas escape

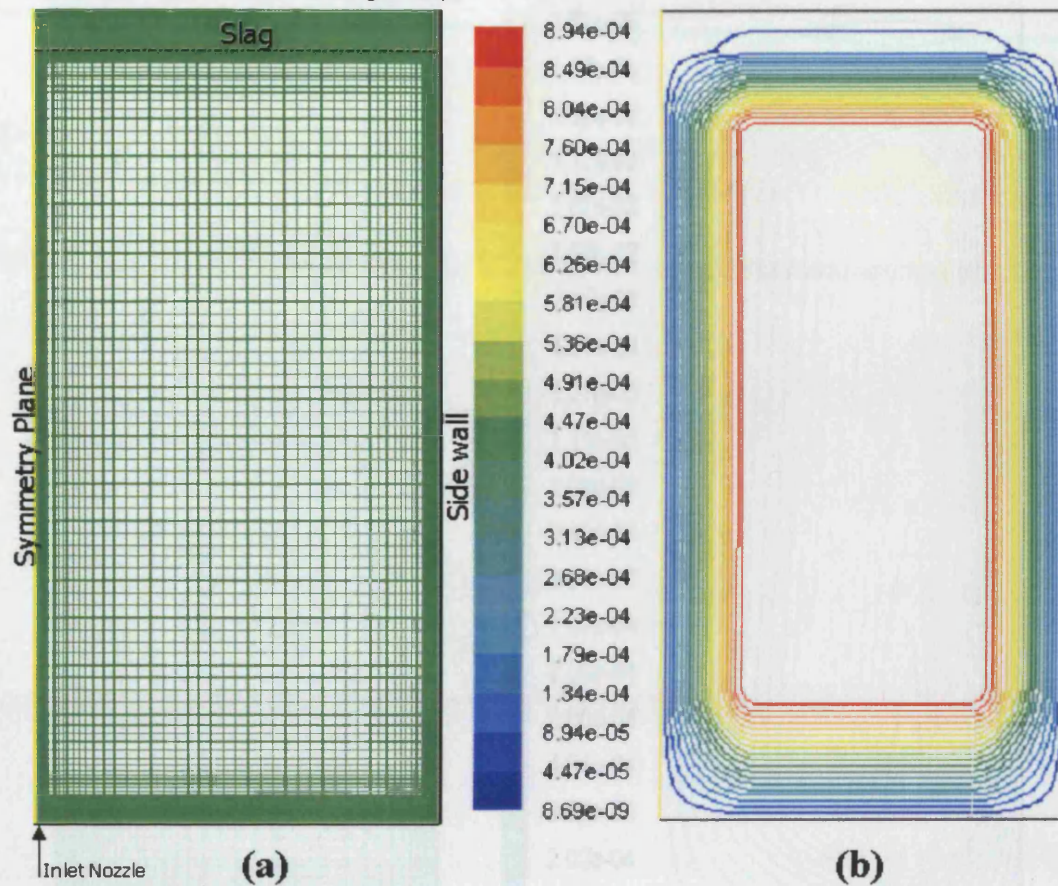


Figure-5. (a) Quadrilateral cell grid with 20400 cells, (b) cell volume contours (m³). This grid was rejected due to the high number of cells causing high computational running time. Fine cells at the bottom and side wall can be avoided using the Enhanced Wall Treatment Fluent function.

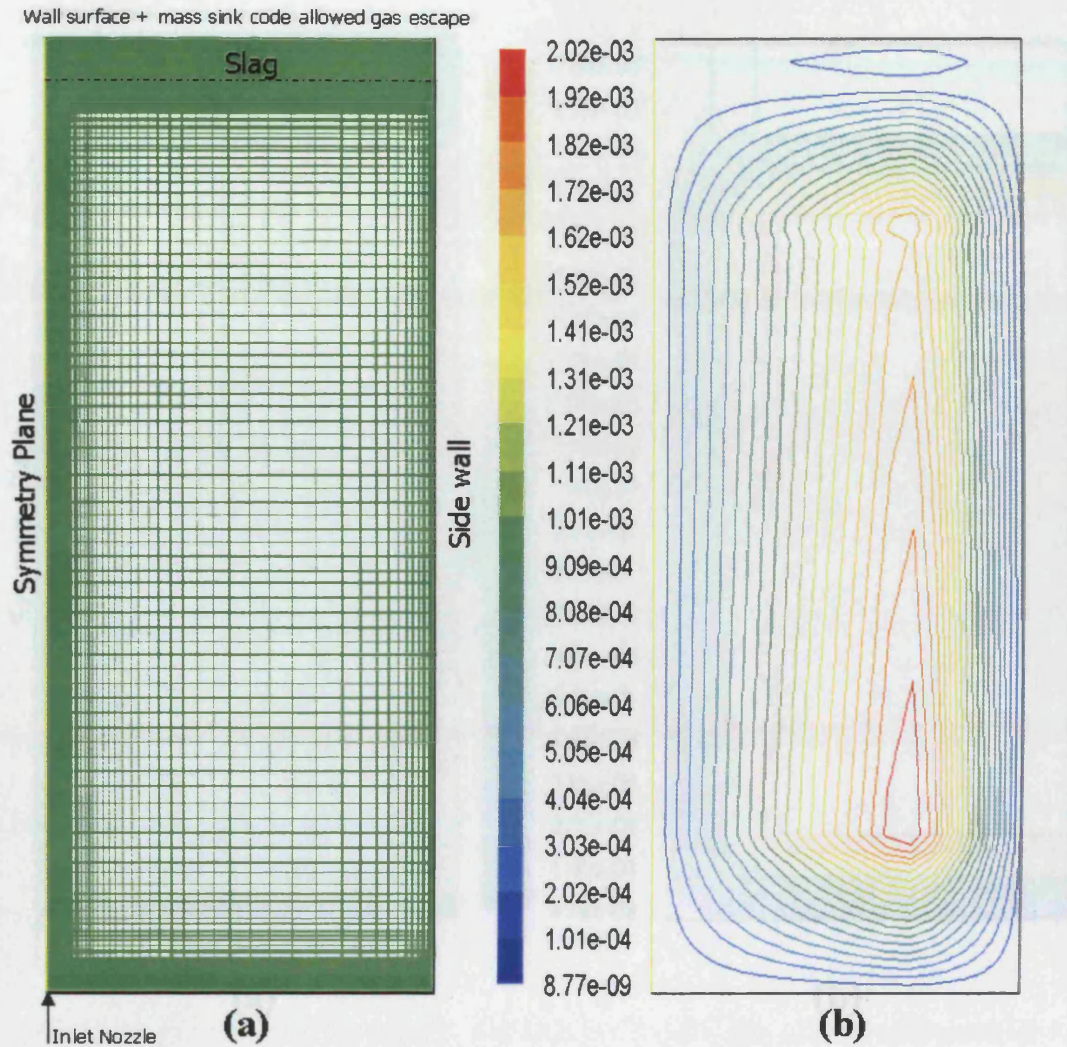


Figure-6. (a) Quadrilateral cell grid with 18955 cells, (b) cell volume contours (m^3). This grid was rejected due to the high number of cells causing high computational running time. Fine cells at the wall can be avoided using the Enhanced Wall Treatment Fluent function.

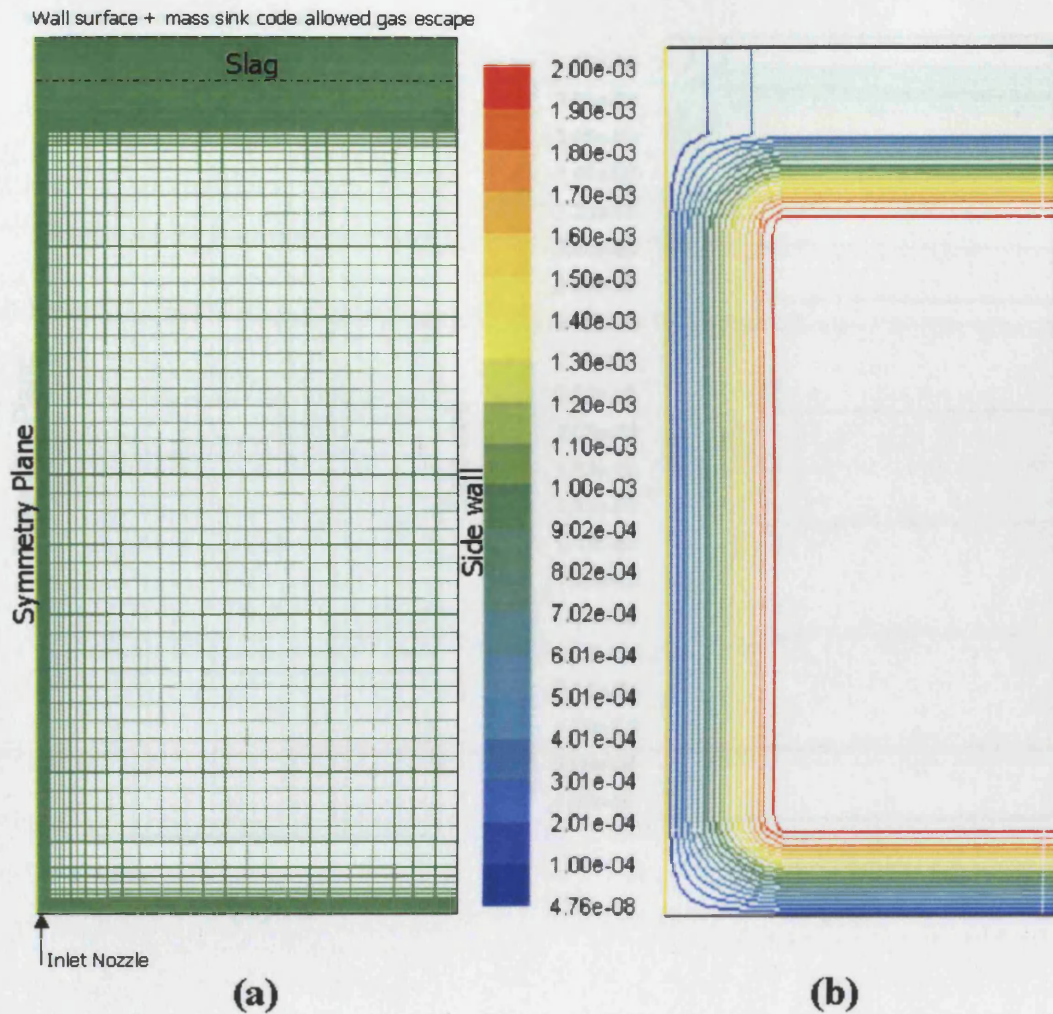


Figure-7. (a) Quadrilateral cell grid with 5341 cells, (b) cell volume contours (m^3). This grid caused a collapse of the solution due to the high growth rate of the cell size from the symmetrical axis on the left side toward the wall side. The growth rate was within the well known recommended range ($\pm 20\%$) in CFD.

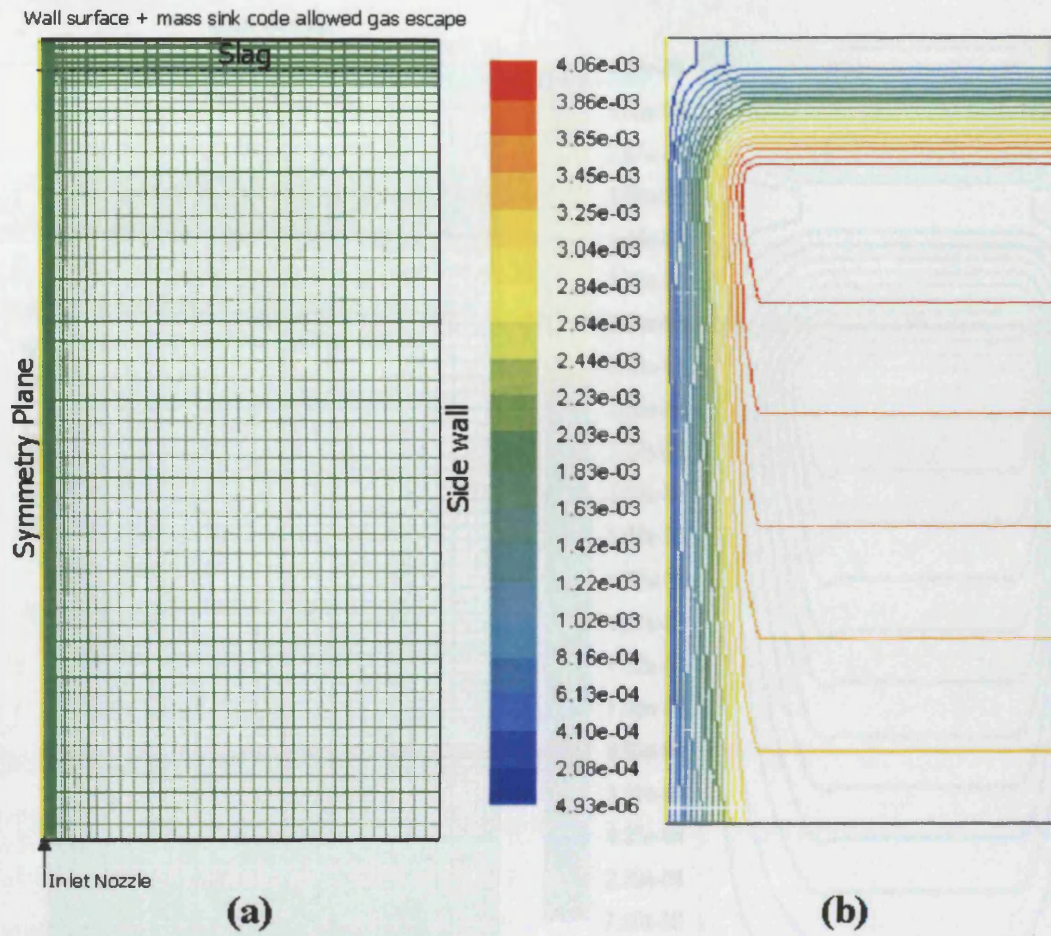


Figure-8. (a) Quadrilateral cell grid with 3016 cells, (b) cell volume contours (m^3). The solution collapsed due to the coarse grid used at the steel/slag interface zone.

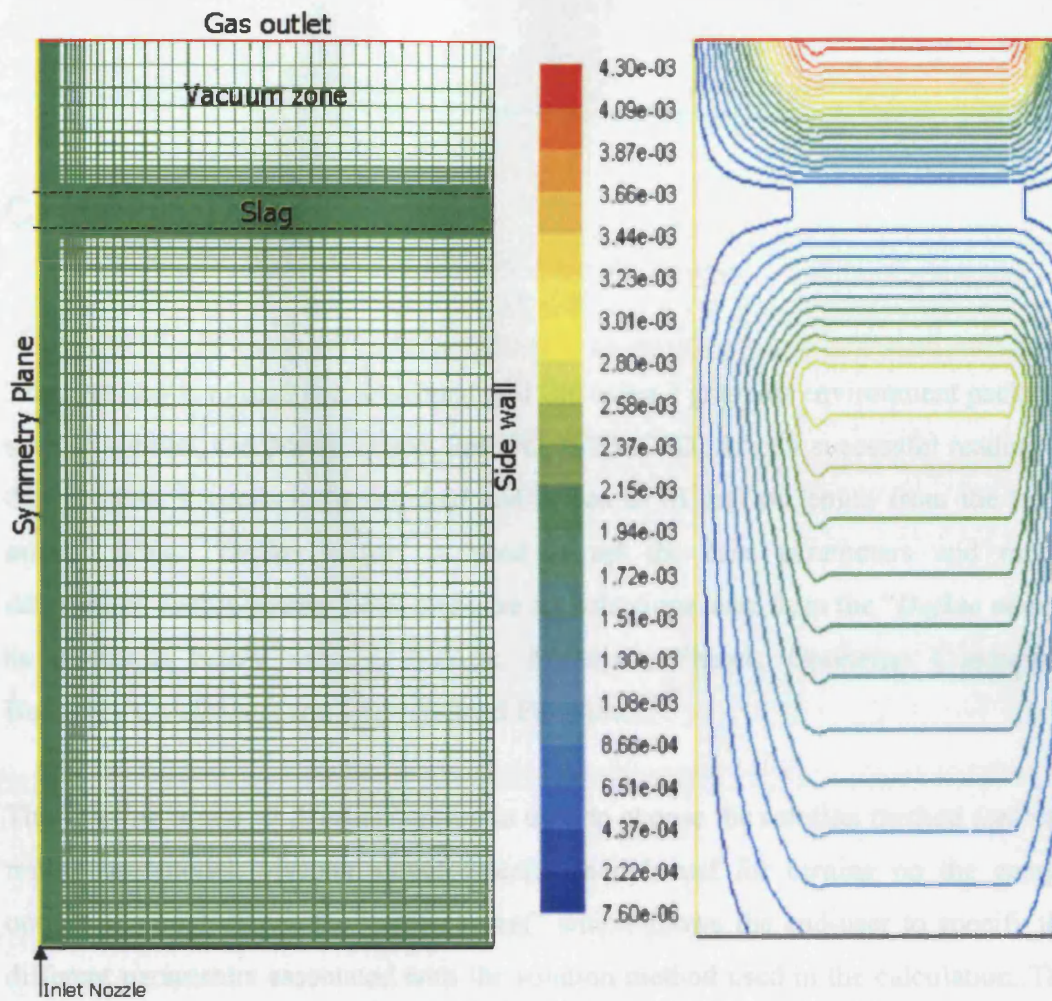


Figure-9. A new vacuum zone was added on the top of the slag layer occupied by gas. (a) Quadrilateral cell grid with 7600 cells, (b) cell volume contours (m³).

CFD model creation steps

The first step is to read the developed grid file using a graphics environment package, such as Gambit, GeoMesh, TGrid, PreBFC, ICEMCFD. After a successful reading of the grid file, it needs to be checked and scaled to SI unit of length from the “*grid menu*”. Then “*Define menu*” is used to set the case parameters and model description. In this present work there are six selections used from the “*Define menu*” as discussed below namely; Models; Materials; Phases; Operation Conditions; Boundary Conditions; and User-Defined Function.

The “*Define menu* → *Models*” option is used to choose the solution method (solver); multiphase model; viscous model; species model; and for turning on the energy option. Figure 1 shows the “*solver panel*” which allows the end-user to specify the different parameters associated with the solution method used in the calculation. The segregated solution algorithm method and implicit formulation approach were selected for this present work, which allowed the use of the Eulerian multiphase model as discussed below. More details about these solver options and other options can be found in the Fluent support manuals.

The “*multiphase model panel*” is shown in figure 2. Fluent provides three different models namely; “volume of fluid”, “mixture”, and “Eulerian”. The Eulerian model was used in this analysis due to its ability to solve separately the conservation equations for each single phase in the system with exchange mechanisms of the momentum, heat and mass exchange between the phases. In other words, it was selected because it is the only multiphase model that allows the mass transfer of the species of interest between phases.

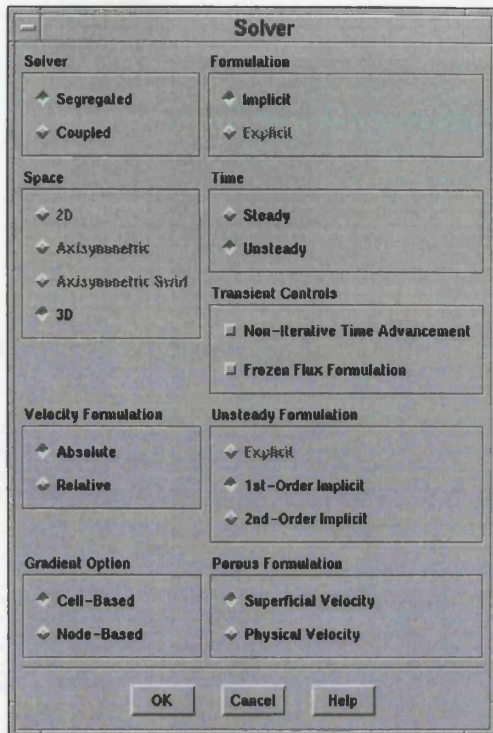


Figure-1 Solver panel.

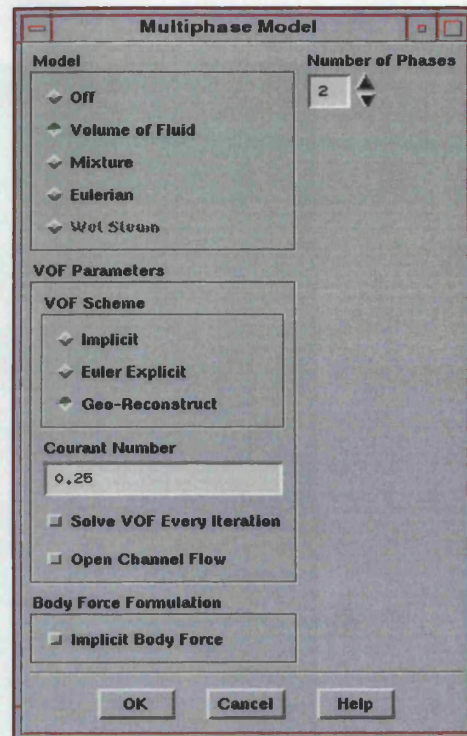


Figure-2 Multiphase model panel.

The “*viscous model panel*” is shown in figure 3. Fluent provides several models as presented in the figure. Also, the end-user is allowed to customize the viscous model as required. The $k-\epsilon$ turbulence model was selected in this present work (see section 3.1). Furthermore, the “*Enhanced wall treatment*” option can be used to enhance the solution near the wall with a lower number of cells. This is turned on in this present work.

The “*Define menu → Materials*” option is used to define the materials properties for the different phases. The “*Materials panel*” is shown in figure 4. Fluent provides a huge material library. However, a new material can be added and/or the material properties can be modified. Using this panel, the slag material was defined. Also, User Defined Function (UDF) files were loaded to define some of the variable properties as a function of temperature. Furthermore, this material panel is used to define the species mixture properties. In this model a species mixture named steel-mixture was created, that is made of the steel phase as a carrier with mass fractions of some dissolved elements such as aluminum and sulphur. Also, a slag mixture was created. “*Species panel*” is shown in figure 5.

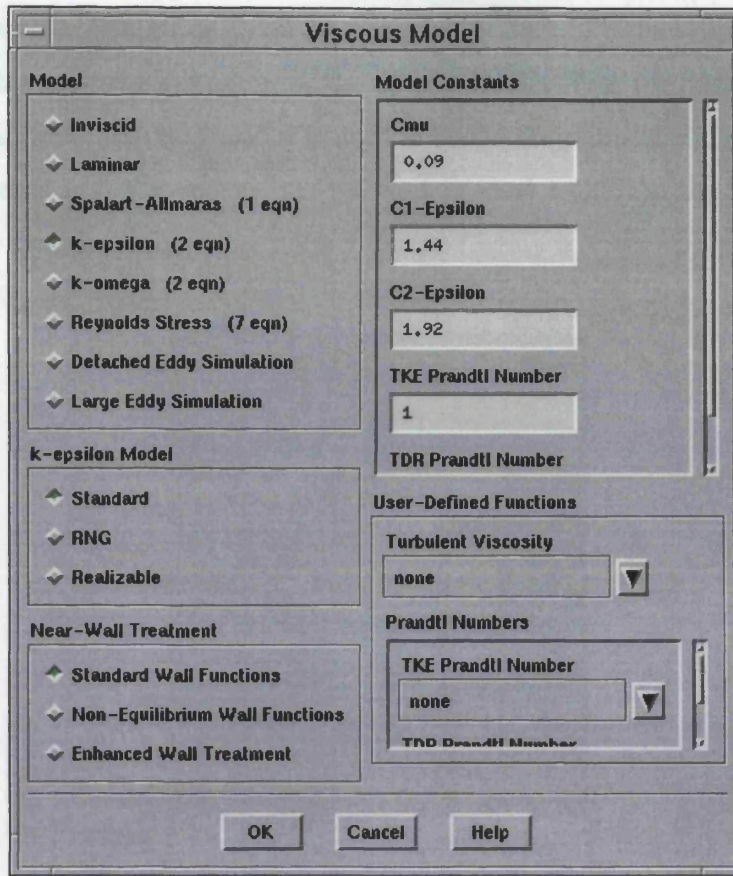


Figure-3 Viscous model panel.

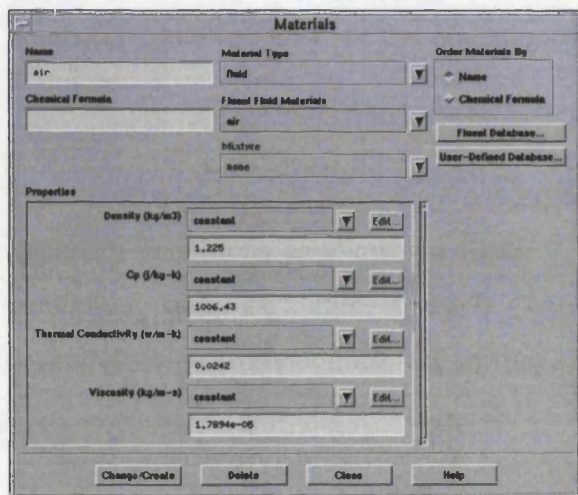


Figure-4 Materials panel.

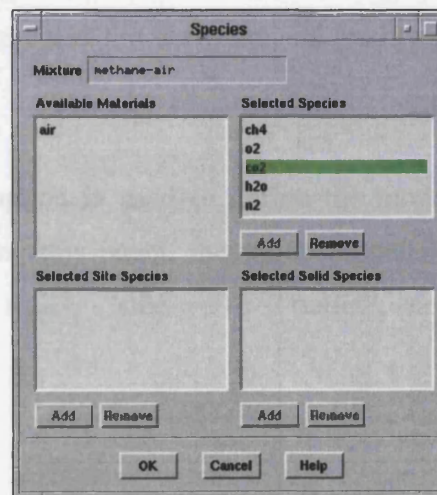


Figure-5 Species panel.

The “*Define menu → Phases*” option shown in figure 6 is used to set the primary and the second(s) phase(s) parameters such as the phase material defined earlier in the materials panel. Also, the interactions between phases such as the drag coefficient,

heat transfer, and mass transfer are set by using this panel. The phase can be defined as a single material like air or it can be a species mixture like steel-mixture discussed earlier, but this requires activation of the species model from the “*Model panel*”. In this work, the steel-mixture material is used to define the primary phase, and the slag-mixture material and the Argon gas material is used to define the two secondary phases of the system.

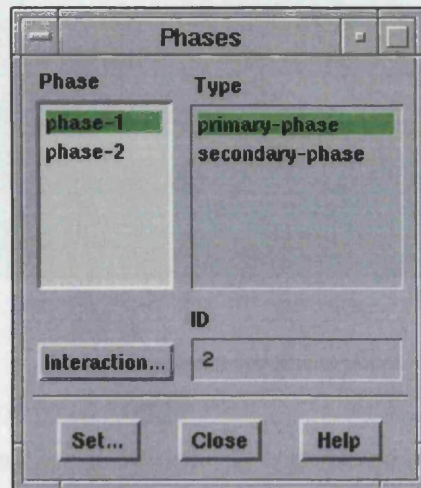


Figure-6 Phases panel.

The “*Define menu* → *Operating conditions*” option is used to define the system operation condition such as the operation pressure and the activation of gravity if required.

The “*Define menu* → *Boundary conditions*” option is used to define the model boundary conditions as shown in figure 7. Using this panel, the model boundary conditions such as “inlet nozzle”, “bottom wall”, “side-wall”, “outlet”, and “symmetry side” were defined (see section 3.2).

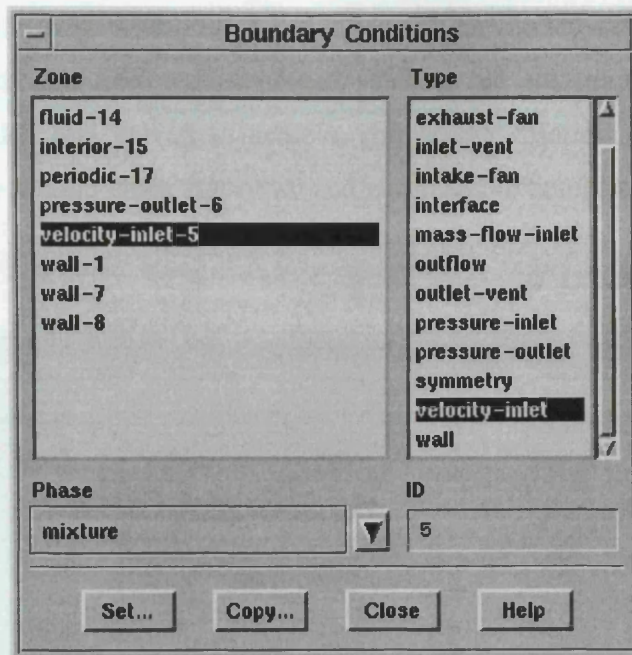


Figure-7 Boundary conditions panel.

At this step, the model setting is completed and the next step is to set the solution procedure. “*Solve menu* → *Initialize* → *Patch*” option is used to define the three phases (steel/slag/gas) initial volume fraction; initial species mass fraction; and the initial temperature at each one of the different defined regions. The control volume was divided into three regions (see section 3.1) using the “*Adapt Iso-Value*” as shown in figure 8. For this present multiphase case the default initialization panel was not sufficient to initialize the case. Therefore, the “*Adapt Iso-Value*” panel was used instead of initializing the case.

At this point, the case should be ready to run. However, due to complicated situation here where three unlike phases are on top of each other, a proper solution initiation should be achieved. As per the Fluent manual, an initial solution using the Mixture multiphase model can be used as an initial solution for the more advanced Eulerian multiphase model. However, in this present work, this strategy did not work. Figure 9 shows the “*Solve* → *Controls* → *Solution*” panel to control the solution algorithm. The solution started using the first order equation algorithm with the activation of only two equations (flow and volume fraction). These equations were solved using a very small time step (0.00001sec) until a converged solution was achieved. Then, the

Turbulence equation was added into the solution and the model was run for some time until a converged solution was achieved; and so on i.e. more equations were successively loaded and solved to achieve converging solution. Then the solution upgraded into the second order algorithm and was ready to complete the mathematical journey.

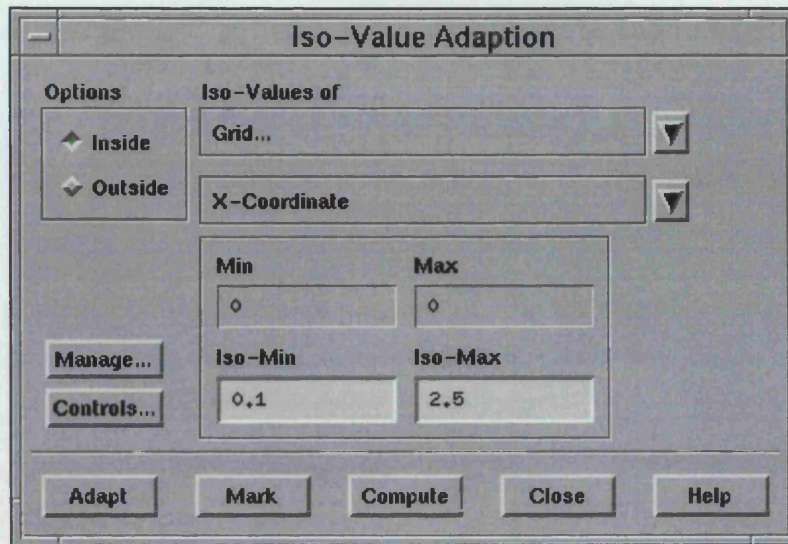


Figure-8. Iso-value adaption panel.

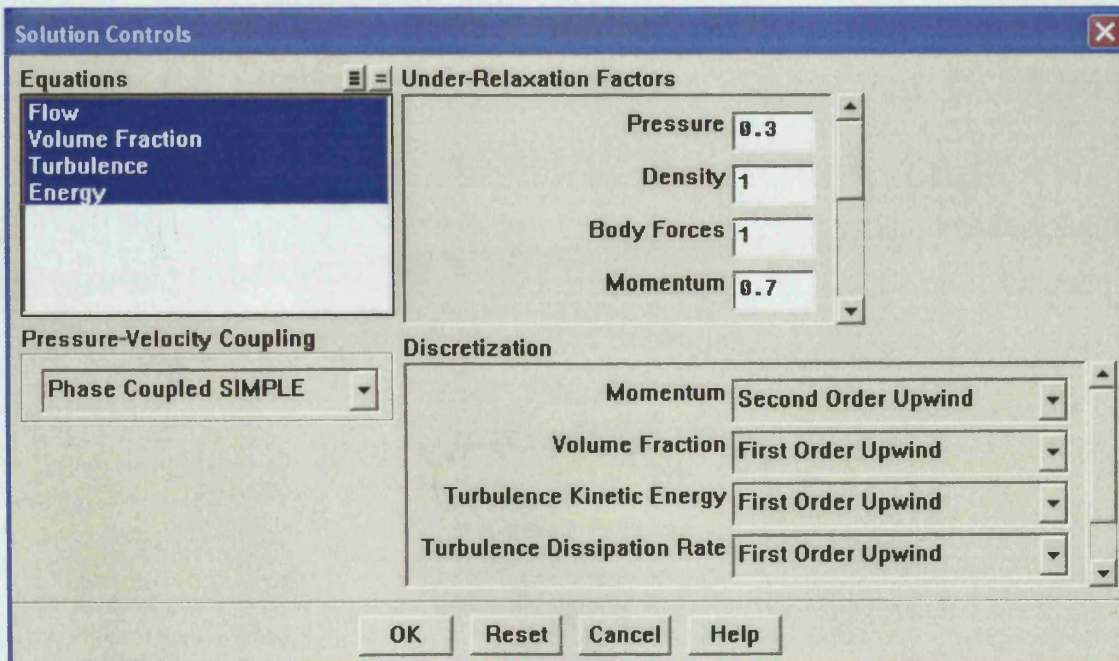


Figure-9 Solution control panel.